UNIVERSITÀ
DEGLI STUDI
DI PADOVA

Host Istitution: Università degli Studi di Padova

Dipartimento di Geoscienze

DOCTORAL COURSE IN EARTH SCIENCES
SERIES XXIX

MORPHOMETRIC ANALYSIS OF DIFFERENTLY DEGRADED SIMPLE CRATERS ON THE MOON

This PhD Thesis has been founded by INAF-OAPD

Coordinator: Prof. Fabrizio Nestola
Supervisors: Prof. Matteo Massironi and Dott. Gabriele Cremonese
Co-Supervisor: Dott. Andrea Ninfo

PhD candidate : Valerio Vivaldi

The Moon has held our imaginations for millennia, yet it is only in modern times that we have visited this body, first with robotic machines and then with astronauts. Exploration of the moon has taught us much about the evolution of the solar system and ourselves. We've known for centuries about the effects on tides and biological cycles from a waxing and waning moon. But it took space-age exploration to show us how the moon is connected to human existence on a very fundamental level.

By Paul D. Spudis
(Lunar and Planetary Institute)

INDEX

ABSTRACT

The main focus of this PhD research is the morphologic characterization of simple impact craters on lunar maria in order to find out a correlation between craters morphological degradation and absolute model ages of the surfaces where they were emplaced. Crater degradation can be indeed used to constrain the chronological evolution of planetary surfaces.

The crater degradation is usually retrieved through visual inspection by subdividing craters into 4 classes: C1 represents the freshest ones, C2 are the ones with the first evidence of degradation (smoothed rim), C3 and C4 are related to morphologies ranging from heavily eroded to totally flattened respectively [Arthur, 1963].

We firstly conducted a morphometric analysis of craters representative of the four classes starting from the freshest one represented by the Linné crater. Craters were chosen on a homogeneous geological unit, the S28 unit in mare Serenitatis, with an absolute model age of 2.84 Gy [Hiesinger et al., 2011]. This analysis allowed us to establish the thresholds of mean *slope* from craters inner wall, in order to constrain the morphometric characterization of the four degradation classes.

Successively we have extracted all impact craters (383) from a unique geological unit and we have defined the morphologic relationships among the degradation classes in function of the craters diameters.

Finally, we expanded our analysis to six lunar *maria*, considering six lunar maria with different average absolute model ages, in order to perform this analysis with the wider range of ages. For each mare we considered a unique surface (dataset) derived from the merging of geological units with similar absolute model ages within the basin, in order to guarantee the most homogeneous possible surfaces, both in terms of impact rheology and absolute age. From the six surfaces we have extracted inner wall mean *slopes* from over 1000 impact craters. The mean *slope* values of the inner walls have shown a relation between crater morphology and the absolute model ages of the geological units where they are located. Older basins are characterized by craters with lower mean slope values, suggesting a dominance of older craters in their population, whereas the younger units have shown higher mean slope values of their simple craters, suggesting a population dominated by recent impacts. This tendency is the expression of the morphological alteration strictly connected to the lunar maria age. Since the geomorphometry of impact craters is influenced by the absolute age of the target area, we have constrained potential isochrones by fixing absolute age thresholds based on the morphological variations of impact craters.

RIASSUNTO

Il principale obiettivo di questa tesi di dottorato è stato la caratterizzazione morfologica dei crateri di impatto semplici all'interno dei maria lunari, al fine di trovare una correlazione tra la degradazione dei crateri e l'età assoluta stimata delle superfici ad essi correlate. La degradazione dei crateri può essere infatti utilizzata per comprendere meglio l'evoluzione cronologica delle superfici planetarie.

In questa ricerca abbiamo considerato le quattro classi di degradazione generalmente impiegate nella classificazione visuale dello stato di degradazione dei crateri. Sulla Luna la classe C1 rappresenta crateri freschi, la C2 crateri al primo stadio di degradazione (rim smussato) e le ultime due classi sono riferite ai crateri con morfologie profondamente modificate dall'erosione (C3) e totalmente erosi (C4) [Arthur, 1963].

In primo luogo abbiamo condotto una analisi morfometrica su crateri rappresentativi delle 4 classi a partire da Linné che viene considerato il riferimento dei crateri semplici di tipo C1 sulla luna. Quest'analisi è stata fondamentale per stabilire le soglie di inclinazione media relativa alla scarpata interna di crateri rappresentanti le quattro classi. Attraverso queste soglie è stato possibile caratterizzare morfometricamente le quattro classi di degradazione. Successivamente abbiamo estratto 383 crateri da una singola unità geologica per confrontare le relazioni morfologiche tra le classi di degradazione in funzione del diametro dei crateri. Infine l'analisi morfometrica è stata estesa a diversi *maria* lunari, mediante l'estrazione di migliaia di crateri di impatto semplici provenienti da superfici con diversa età. Successivamente sono stati considerati sei bacini lunari con età medie molto differenti, per sviluppare l'analisi su un range di età il più grande possibile. Per ogni bacino è stata creata una superficie (dataset), derivata dal raggruppamento di unità geologiche coeve del bacino stesso, così da estrarre crateri posti su una superficie il più omogenea possibile sia in termini di reologia di impatto che di età assoluta.

I valori di pendenza media delle scarpate interne dei crateri estratti hanno dimostrato una relazione con l'età assoluta stimata delle unità geologiche in cui si trovano. I bacini più vecchi, infatti, sono caratterizzati da crateri con valori inferiori di pendenza media, il che suggerisce una predominanza di crateri antichi ed erosi. Le unità più giovani, invece, hanno mostrato crateri con alti valori di pendenza media, suggerendo una popolazione dominata da impatti più recenti. Questa tendenza è espressione della degradazione morfologica, strettamente legata all'età assolute dei *maria* lunari.

Poiché la Geomorfometria dei crateri da impatto è risultata essere influenzata dall'età assoluta delle stesse superfici di impatto, abbiamo potuto creare delle potenziali isocrone fissando soglie di età assoluta basate sulle variazioni morfologiche dei crateri da impatto.

INTRODUCTION

1- Exploration of the Moon

The Moon is our closest planetary body and its surface was observed since the development of optical telescopes. The first pioneering exploration of the Moon was in 1959 when *Luna 1*, a small Soviet sphere probe, flew over our natural satellite at a distance of 5995 km, revealing the absence of lunar magnetic field and the evidence of the solar wind. Since *Luna 1* reached the Moon shifted from a unattainable silver sphere visible in our sky to a real place, a potential destination for probes and human missions. *Luna 2* in 1959 landed on the Moon surface near Aristides, Archimedes, and Autolycus craters. However only with the *Luna 3* probe humanity observed for the first time the far side of the Moon, never visible from the Earth.

The first USA landing on lunar surface was in 1962, when NASA lunched *Ranger 4*, a kamikaze missions set up to crash on the surface and capturing as many images as possible before the contact with the surface. After several failures *Ranger 7* succeeded in taking pictures of *Mare Nubium* in 1964 and it was followed by *Ranger 8* and *Ranger 9.* Thanks to these missions we discovered very small impact craters. Those craters were formed by the micrometeorite bombardment, one of the reasons for the formation of the lunar fine powder, called regolith. The first orbit around the Moon was performed by Soviet probe *Luna 10*, in 1966. Again U.S.S.R were the pioneers of the soft-landing, with the automatic robot *Luna 9,* successful landed on *Oceanus Procellarum*, where it founds a powdered surface with few rocks and a strength sufficient to support the weight of a lander [ROSCOSMOS].

NASA followed with the landing of the robotic spacecraft *Surveyor 1* in 1966. Over the years robotic missions, such as the five NASA *Lunar Orbiters*, have mapped the entire Moon surface from orbit retrieving extremely high resolution images of potential landing sites for the forthcoming Moon landings of *Apollo* missions. At the same time aerospace technology was developing very quickly until Neil Armstrong made the first steps on the Moon surface in the 1969, with the *Apollo 11* mission. Later missions saw astronauts spend as long as three days on the Moon driving a lunar rover that across the satellite's surface. Before the end of *Apollo* project in 1972, five other missions and a dozen men had explored the Moon, included the geologist-astronaut Jack Schmitt onboard the *Apollo 17*.

Apollo missions provided also several lunar samples from different regions of the Moon, allowing scientists to perform radiometric absolute age estimations for the first time in other planetary surfaces.

In 1994 the *U.S. Naval Research Laboratory* (*Ballistic Missile Defense Organization*) launched *Clementine* mission, initially pointed to test military technologies and successively focused to perform the first global mapping of the Moon surface. The observations included imaging at various wavelengths including ultraviolet and infrared, laser ranging altimetry, and charged particle measurements, with the purposes of assessing the surface mineralogy of the Moon and obtaining a lunar altimetry map from 60N to 60S latitude. In 1999 was the turn of *Lunar Prospector*, aimed to find out possible evidence of ice at the lunar poles, to complement the previously *Clementine*'s Moon composition mapping and to explore the Moon's gravitational field. One of the main scientific goals of *Lunar Prospector* was the support to the Moon formation hypothesis, confirming the later formation of the Moon with respect to the Earth. At the end of the mission the spacecraft was intentionally crashed into the Moon in the hopes of raising a plume that could yield evidence of water ice, but none was observed from earth based telescopes [NASA]. In the last years several missions of different countries interested the Moon.

In 2007 *Japan Aerospace Exploration Agency* [JAXA] lunched the *Kaguya-Selene* mission in order to obtain scientific data of the lunar origin and evolution and develop the technology for future lunar explorations. Some of the main results of this mission are the improvement of lunar global topography, with global high resolution images and *Digital Terrain Models* and a detailed gravity map of the far side of the Moon.

In 2009 NASA lunched the *Lunar Reconnaissance Orbiter* spacecraft with the purpose of investigating the lunar surface through a global 3D high resolution topography, improving maps of mineralogical components of the lunar crust and finding potential landing sites for future human missions.

In the last years China and India developed the technology to reach the Moon with several missions. China lunched the *Chang'e 1* orbiter in 2004, followed by the orbiter spacecraft *Chang'e 2* (2010) and the lander probe *Chang-e 3* (2013) that was a small rover landed on the lunar surface. The scientific objectives of *Chang'e* missions include lunar surface topography and geology survey, lunar surface material composition and resource survey, Sun-Earth-Moon space environment detection [CNSA]. On the Indian side in 2008 was lunched *Chandrayaan-1* mission with the objectives to perform of a three-dimensional high resolution atlas of both the near and far sides of the Moon and a high spatial resolution chemical and mineralogical mapping of the entire lunar surface.

2- Physical and Geological properties of the Moon

The Moon has a diameter of 3476 km, with a density of $3.34 g/cm^3$ and the average distance from the Earth is 385000 km. The internal structure of our satellite is differentiated: crust, mantle, and core. The crust has a thickness of about 50-60 km and the

lithosphere-asthenosphere transition is approximatively 1100 km deep. The mantle presents a thickness of about 650 km and is subdivided in upper and lower mantle. Recent 3D thermal evolution models of the Moon have confirmed the possibility for the presence of a solid inner iron-rich core with a radius of about 240 km and a fluid outer core primarily made of liquid iron with a radius of about 330-350 km, surrounded by a partially molten boundary layer [Weber et al., 2012; Zhang et al., 2013].
The basaltic lunar rock samples erupted onto the surface from mantle partial melting confirm the mafic mantle composition. The crust thickness is on average about 50 km [Wieczorek et al., 2006].
The main volcanic formations on the Moon are the lunar *maria*, generated by ancient large impacts successively pooled by basaltic lavas. They appear as dark and relatively featureless smoothed plains, not saturated by cratering.
On the nearside of the Moon *maria* basins cover about 31% of the surface, whereas on the far side the *maria* coverage is only 2% [Wilhelms, 1987].
The analyses conducted using laser altimeters and stereo images allowed to perform a detailed topographic map of the Moon, revealing elevation difference between far side and near side, of 1.9 km on average.
The Moon surface is densely cratered (more of 300000 impact craters with diameter > 1 km in the near side), being impact cratering the major geologic process that has affected its surface [Melosh, 1989]. For this reason impact craters are the main geomorphological markers on which is based the lunar geological timescale. They are generally well-preserved because of the lack of an atmosphere and an idrosphere, being the space weathering a very slow erosional process.
The selenological timescale divides the history of the Moon into five periods: Copernican (0 to 1 Ga), Eratosthenian (1.0 to 3.2 Ga), Imbrian (3.20 to 3.85 Ga), Nectarian (3.85 to 3.92 Ga), and Pre-Nectarian (3.92 to 4.6 Ga). [Wilhelms, 1987]. The radiometric ages of impact-melted rocks collected during the Apollo missions, clustered between 3.8 and 4.1 Ga, has been used to constrain the absolute ages of lunar geological periods.

3- Formation and morphology of simple impact craters

The final morphology of impact craters derives from the post impact modifications, mainly due to gravitative collapses of the steepest parts of the rim within the transient crater. The transient crater has a circular bowl-shaped cavity, with a depth-diameter of about 1:4. The shape of a transient crater is not influenced by the impact velocity, diameter or impact angle, but it undergoes to morphological modifications due to gravitational phenomena. The final impact crater morphology is hence strictly related to gravity, rock density and strength and geological setting of the target surface.

The gravitational instability on small simple impact craters involve the rim, composed and surrounded by fractured, heated and shocked rocks, that collapse within the crater producing landslides, dry flows and lens of broken rocks accumulation on the floor. Differently, large craters are subjected to dramatic collapses, that give rise to the formation of wall terraces , central peaks and internal rings (complex craters). The very large craters also form several rings (multi-ring craters).
On the Moon the transition between simple and complex craters is estimated close to 15 km of rim diameter. The morphology of complex craters is more complicated and the erosion of so large craters is too slow, being the degradation effect less clear [Fassett, 2014]. On the other hand simple impact craters have a morphology easier to characterize and their erosive evolution is more evident. Moreover simple craters are widely distributed than complex craters within lunar *maria*. For these reasons we have chosen simple impact craters to perform our analyses [Melosh, 1989, 1999, 2011].

4- Current dating method and the contribute of this research

Nowadays the age estimates of geological units on planetary surfaces are mainly performed with *crater counting*. This method is based on the concept for which impact craters accumulate at a nearly constant rate on a fresh surface with no impact craters. Indeed the age of a geological unit and the crater production rate determine the number of impact craters superposed on that geological units [Öpik, 1960; Shoemaker et al., 1962; Baldwin, 1985].
This method has been successively calibrated using the radiometric absolute ages of samples returned back from the Moon by *Apollo* missions, allowing the averaged cratering rate to be estimated much more accurately. Lunar *maria* have preserved the cratering record over their 3.2–3.5 Ga history. The calibrated surfaces allowed to employ with greater confidence *crater counting* as a chronometric tool, in order to date the rest of the unsampled lunar surface. On the basis of the concept for which the crater number is inversely proportional to the square of crater diameter ($N=kD^{-2}$) is possible to retrieve relative ages of not saturated units, by calculating the size–frequency distribution (SFD) of craters and correlate it to a 11°polynomial function, the *Neukum Production Function* (NPF) [Neukum, 1983]. This chronology model is calibrated on the crater size–frequency distribution measurements performed on lunar units on which it is possible a correlation with radiometric ages, retrieved from sample return missions of lunar rocks. Afterwards the NPF was applied on other planetary bodies (e.g. Mercury, Mars and minor rocky bodies) by understanding and modeling the fluxes of impactors. According to Neukum & Ivanov [1994] the overall shape of the crater size–frequency distribution has not changed over the past 4 Ga, suggesting a stable impactor population over the past 4 Ga.

This methodology is wildly employed to date the unsampled planetary surfaces, however at present there are no methods to retrieve the absolute age from the crater degradation.
Crater degradation morphology is an important point of view for the relative age determination among different geological units. This process induces morphologic modification and its obviously related to the geological time, because of the erosion depending, which is due to space weathering as well as gravitational phenomena.
For these reasons crater degradation can be employed to constrain the chronological evolution of a planetary surfaces, on the basis of the concept for which older terrains should have craters in a more advanced state of degradation than younger ones, exposed for a shorter period to erosional processes [Fassett, 2014].
This research is therefore focused on characterizing the degradation of simple impact craters on different lunar maria through a numerical approach based on topographic data.
In order to understand how degradation processes are impressed in the geomorphological evolution of impact craters, was firstly necessary to conceptualize and characterize the morphology of a pristine simple impact crater (Cap.1). In this regard *Linné* is considered in literature as the best preserved impact crater on the Moon, displaying a pristine morphology appearing as an inverted truncated cone [Garvin et al., 2011].
In 1963 Arthur proposed four crater classes of degradation for the Moon: C1 represents fresh craters, C2 are the ones with the first evidence of degradation (smoothed rim) and C3-C4 are related to impact craters with morphologies ranging from heavily eroded to totally flattened ones. However the four degradation classes are discriminated through a visual interpretation, which is affected by subjectivity. To propose an objective procedure of classification we used the high resolution morphometric signature of *Linné* crater as morphological reference for the C1 class. Than we have conducted a high resolution morphometric analysis on other craters representative of C2, C3 and C4, fundamental to establish morphometric thresholds to numerically characterize the four degradation classes. Successively we extracted 252 craters in order to compare the morphologic relationships among the degradation classes pertaining to a unique geological unit (Cap.2).
The morphometric characterization of the degradation classes was a milestone in the understanding of a possible correlation between morphological evolution of impact craters and the age of the surface where they are superposed (Cap.3).
Then, in the light of the above, we expanded our analysis to several lunar maria, extracting thousands of simple impact craters from differently aged surfaces. We have chosen several geological units from six lunar basaltic basins characterized by different absolute ages, as shown in TAB.1.
In particular we gathered geological units with similar absolute model age from basaltic basins, in order to compare crater morphology distribution from the most homogeneous possible surfaces, both in terms of impact rheology and absolute age.

The mean *slope* values of the inner walls have shown a relation between crater morphology and the absolute model ages of the geological units where they are located. Older basins indeed are characterized by lower mean slope values, suggesting a dominance of older craters in their population, whereas the younger units have shown higher mean slope values, suggesting a crater population dominated by recent impacts. This tendency is the expression of the morphological alteration due to degradation processes, strictly connected to the lunar maria age. Since the geomorphometry of impact craters is influenced by absolute age of the target area we may fix absolute age thresholds based on the morphological variations of impact craters to constrain potential isochrones.
This research may potentially offer new possibilities to the estimation of the absolute model ages on planetary terrains, being a parallel support to crater counting.

CHRONOLOGICAL SUBSET	**GEOLOGICAL UNITS** (Hiesinger et al., 2011)	**MEAN AGE**	**SURFACE AREA**	**N° CRATERS**
Procellarum	P60 (1.20Ga); P58 (1.33Ga); P55 (1.67Ga); P56 (1.49Ga); P53(1.68Ga)	1.47 Gy	200,000 km^2	164
Serenitatis	S26 (2.94 Ga); S27 (2.90 Ga); S28 (2.84 Ga)	2.89 Gy	100,000 km^2	181
Imbrium	I19 (3.10 Gy); I20 – I21 (3.01 Gy); I22 (2.96 Ga).	3.02Gy	400,000 km^2	178
Crisium	U1 (3.65±0.05 Ga); U2 (3.50±0.10 Ga)	3.57 Gy	100,000 km^2	159
Endymion	(3.63–3.70 Ga)	3.66 Gy	25,000 km^2	174
Australe	A2 (3.80 Ga); A22 (3.57Ga)	3.68 Gy	25,000 km^2	158

TAB.1- *Lunar basins with the geological units used to perform the statistical analysis. There are the absolute model ages [Hiesinger et Al., 2011], the mean ages of the considered surfaces, the surface area and the n° of extracted craters.*

REFERENCES

Arthur, D.W.G., Agnieray, A.P., Horvath, R.A., Wood, C.A. , Chapman, C.R., 1963. The system of lunar craters. Quadrant I. Comm. Lunar Planet. Lab. 2, #30.

Baldwin R.B., 1985. Relative and absolute ages of individual craters and the rate of infalls on the Moon in the post-Imbrium period. Icarus 61, 63–91.

CNSA (China National Space Administration- http://www.cnsa.gov.cn/)

Fassett C.I. and Thomson B.J. 2014. Crater degradation on the lunar maria: Topographic diffusion and the rate of erosion on the moon. Journal of Geophysical Research: Planets 119, 2255-2271.

Garvin J.B., Robinson M.S., Frawley J., Tran T., Mazarico E., and Neumann G. 2011. Linné: simple lunar mare crater geometry from LRO observations. 42nd Lunar and Planetary Science Conference (2011), #2063.

Hiesinger H., J.W.Head, U. Wolf, R. Jaumann and G. Neukum, 2011. Ages and stratigraphy of lunar mare basalts: A synthesis. Geological Society of America Special Papers 2011;477;1-51 doi: 10.1130/2011.2477.

ISRO (Indian Space Research Organization- http://www.isro.gov.in/)

JAXA (Japan Aerospace Exploration Agency-http://global.jaxa.jp/).

Melosh H.J. 2011. Planetary surface processes. Cambridge University Press, 500 p. NASA.

Melosh H.J. and Ivanov B.A. 1999. Impact crater collapse. Annual Review of Earth and Planetary Sciences 27, 385-415.

Melosh H.J. 1989. Impact cratering: A geologic process. New York: Oxford University Press. 245 p.

Melosh, H.J. and Gaffney, E.S. 1983. Acoustic fluidization and the scale dependence of impact crater morphology. J. Geophys. Res. 88, Suppl., A830-A834.

NASA (NASA National Aeronautics and Space Administration –www.nasa.gov).

Neukum G., 1983. Meteoritenbombardement and datierung planetarer oberfluchen. Habilitation Dissertation for Faculty Membership, University of Munich. 186 pp.

Neukum G. and Ivanov B. A., 1994. Crater size distribution and impact probabilities on Earth from lunar, terrestrial-planet, and asteroid cratering data. In Hazards Due to Comets and Asteroids (T. Gehrels, ed.), pp. 359–416. Univ. of Arizona, Tucson.

Öpik E., 1960. The lunar surface as an impact counter. Month. Not. Roy. Astron. Soc., 120,404 doi: 10.1093/mnras/120.5.404.

ROSCOSMOS (Roscosmos State Corporation for Space Activities-http://en.roscosmos.ru/).

Shoemaker E.M. and Hackman R.J., 1962. Stratigraphic basis for a lunar time scale, in Kopal, Z., and Miklhalov, S.K., eds., The Moon: London, Academic Press, p. 289–300.

Weber R., Lin P.Y., Garnero J.E., Williams Q., Lognonné P., 2011. Seismic Detection of the Lunar Core. Science 331, 309-DOI:10.1126/science.1199375.

Wieczorek M.A., Jolliff B.L., Khan A., Pritchard M.E., Weiss B.P., Williams J.G., Hood L.L., Righter K., Neal C.R., Shearer C.K., McCallum I.S., Tompkins S., Hawke B.R., Peterson C., Gillis J.J., Bussey B., 2006.The Constitution and Structure of the Lunar Interior. DOI:10.2138/rmg.2006.60.3.

Wilhelms D.E., McCauley J.F., and Trask N.J. 1987. The geologic history of the Moon. USGS Report 1348, 302 p.

Zhang, N., E. M. Parmentier, and Y. Liang (2013), A 3-D numerical study of the thermal evolution of the Moon after cumulate mantle overturn: The importance of rheology and core solidification, J. Geophys. Res. Planets, 118, 1789–1804, doi:10.1002/jgre.20121.

CHAPTER 1

MORPHOMETRIC ANALYSIS OF A FRESH SIMPLE IMPACT CRATER ON THE MOON: LINNÉ CRATER

Vivaldi V.[1,2], Massironi M.[2,1], Ninfo A.[3], Cremonese G.[1]

(1) INAF-Astronomical Observatory of Padua, Italy, (2) Dept. of Geosciences, University of Padua, Italy. (3) Dipartimento di Fisica e Scienze della Terra, University of Ferrara, Italy

ABSTRACT

This research introduces a quantitative method to characterize the morphology of a fresh simple impact crater on the Moon. At this purpose a morphometric analysis was conducted on high resolution Digital Terrain Models (DTMs) produced by Lunar Reconnaissance Orbiter (LRO) (NASA). Linné is a well-preserved impact crater of 2.2 km in diameter, located at 27.7°N 11.8°E, near the western edge of mare Serenitatis on the nearside of the Moon. The crater was photographed by many space missions orbiting the Moon and its particularly pristine morphology may place Linné as one of the most striking example of a fresh simple crater. In particular, we have performed the morphometric signature of the four main morphological sectors of the crater (rim, floor, inner and outer wall) using the "NAC DTM LINNECRATER E280N0120" DTM (2m/px). The morphometric signature of Linné crater enlighten its pristine morphology, confirming that the crater was not eroded by degradation processes. For these morphometric characteristics Linné can be considered as a base reference for the morphologic analysis of crater degradation. In addition, from a detailed analysis of the Linné inner scarp we have found the presence of clear-cut boundaries within the inner scarp, highlighting the morphologic setting of possible lava emplacement events sequences.

INTRODUCTION

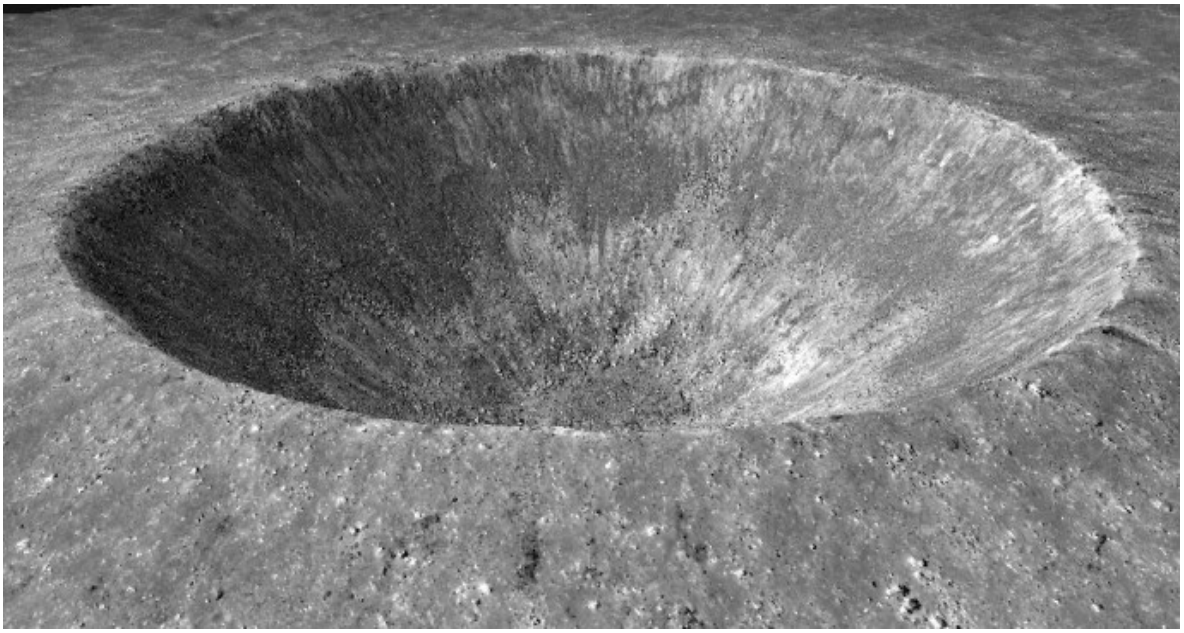

Fig.1- 3D visualization of Linné crater from high resolution DTM (LROC).

Impact craters are the most widespread landform on the rocky bodies surfaces of the Solar System [Melosh, 1989]. They have been collected on planetary and small bodies, and therefore they kept the record of the cumulative effects of subsequent impacts, volcanic emplacements, tectonics, landslides, aeolian activity, and space weathering [Neukum et al., 1975]. The morphology of simple impact craters depends on the interaction between gravity and target strength under dynamical loading [Melosh, 1989, 1999, 2011]. In addition, post-impact modification processes as for instance crater degradation, might deeply affect the morphology of observed structures.

On the Moon crater degradation is due to gravitational processes (landslides, dry flows) and space weathering, and it can be related to the chronological evolution of planetary surfaces, known as planetary resurfacing. The space weathering is a process of erosion and mineral alteration caused by cosmic, solar rays and micrometeorite bombardment: this process is particularly influenced by micrometeoroids flux [Cremonese et al., 2013; Pieters et al., 2012; Hapke, 2001; Vernazza et al., 2009].

This research introduces an innovative method to determine and quantify the post-impact morphology of a lunar simple impact crater.

Morphometric analysis has twofold benefits as the topographic based survey and the quantitative approach, providing for an objective analysis. Geomorphometry on planetary surfaces is indeed usually conducted through the measurements of 2D topographic profiles

[e.g., Aasim and Bahuguna, 2014; Basilevsky et al., 2014; Fassett and Thomson, 2014; Pike, 1995; Salamumićcar et al., 2012; Watters et al., 2015], but areal 3D surveys on high resolution DTMs are normally favored by Earth geomorphologists since in this way a much robust statistic is guaranteed. Moreover, this distributed analysis allows a better understanding of the real landforms characteristics (i.e. areal extension, continuity, precise boundary definition, etc.). Hence, in this analysis we have applied a 3D areal approach in order to retrieve an accurate surface statistic from the extraction of the morphometric variables.

Post-impact simple crater morphology can be better studied from the analysis of fresh pristine impact structures. In this regard Linné (*Fig.1*) is one of the best preserved simple impact crater on the Moon, showing a particularly pristine morphology and appearing as an inverted truncated cone [Garvin et al., 2011]. Linné is located near the western edge of *mare Serenitatis*, a basalt smooth basin located on the nearside of the Moon, on S14 spectral unit. S14 has an absolute model age of 3.49 GY [Hiesinger, 2011] and it's superposed on LPM-1 unit, that is characterized by a smooth morphology with an albedo ranging from 0.064 to 0.066 [Carr, 1966].

DATA AND METHODS

Remote sensing data from the recent space missions provided a huge amount of high resolution *Digital Terrain Models* (*DTMs*). This detailed topographic survey enables a surface analysis with a high level of accuracy. High resolution topography was fundamental for the characterization and the quantification of the geomorphometry on the four different morphological homogeneous domains of a simple impact crater.

The geomorphometric analysis of Linné crater was carried out on *Lunar Reconnaissance Orbiter* (LRO) data, and more in details on the orthorectified images with cell size of 0.5 m and the Digital Terrain Model (DTM) with cell size of 2 m. The DTM was generated from the LRO Camera – *Narrow Angle Camera* (LROC NAC) stereo pairs, calibrated on the *Lunar Orbiter Laser Altimeter* (LOLA) transects [Robinson et al., 2010].

LROC images were acquired at different solar illumination conditions between March and October 2010. The camera was not designed as a stereo system, but can obtain stereo pairs through images acquired from two different orbits (with at least one off-nadir slew) [Beyer et al. 2009]. The DTM was produced processing the stereo pair with USGS Integrated Software for Imagers and Spectrometers (ISIS) for the radiometric correction, and SOCET SET® from BAE Systems for the ingestion of spacecraft coordinates, altitude, Euler angles, and ephemeris positions [Tran et al., 2010]. The LOLA near center-line topographic transect of the crater were acquired between June and September 2010.

In particular, we used the "NAC DTM LINNECRATER E280N0120" *Digital Terrain Model* with a cell size of 2m and the derived product "NAC DTM LINNECRATER M139829261 50CM".

METHODS

With the purpose of a morphological quantification of a lunar fresh simple crater the main four morphological domains of the crater (rim, floor, inner and outer wall) were studied. This analysis has been conducted by processing a high resolution DTM in order to retrieve different derivatives such as *slope*, *curvatures* and topographic *openness*. *Curvatures* have been calculated along different planes: the *profile curvature* has been calculated along the maximum slope plane and the *plan curvature* along the horizontal plane. The topographic *openness* is an angular measure applied on an irregular surface in order to quantify the dominance or the enclosure degree of the surface [Yokoyama et Al., 2002]. In this study the positive *openness* has been adopted to emphasized convex morphologies, as for instance the rim crest, using a radial distance of 1000 m.

All those morphometric variables have been employed as a topographic and numerical tool for the automatic detection of the four domains. In particular *slope* was applied to detect the inner and the outer scarp whereas *curvatures* automatically detected the rim and the floor boundaries. Moreover, with the *topographic openness* we were able to better highlight the edge between the rim and the inner scarp, showing the pristine crest as well as morphological irregularities within the inner scarp. However, the calculation of *curvatures* is particularly affected by DTM noises and errors. For this reason, we applied a multi-scalar approach in order to reduce DTM noises and errors, evaluating also the scale sensitivity of the analyzed surfaces. At this purpose, a kernel analysis has been employed to calculate *curvatures*. *Land Serf* software has been applied to statistically assess the maximum expression of the *profile curvature* at different kernel sizes [Wood, 2009]. In particular, every kernel size from 3x3 to 99x99 has been tested, corresponding on the Linnè DTM to a window area ranging from 6m^2 to 198m^2. The maximum expression of the profile curvature for this DTM resulted to be the 66m^2 one as shown in *Fig.2*.

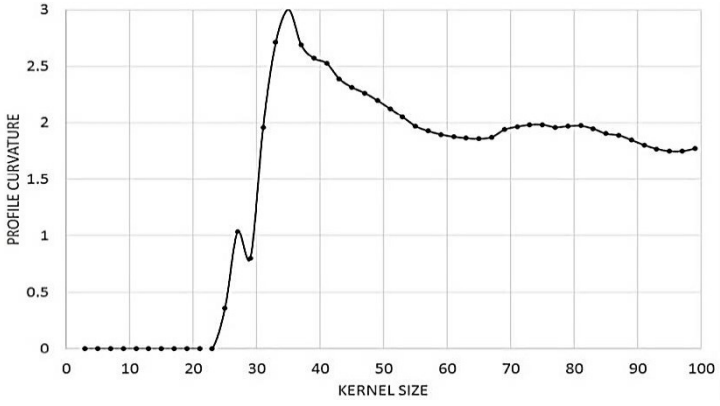

Fig.2- Plots of the maximum expression of the profile curvature at different evaluation kernel sizes for the LRO DTM, testing every kernel sizes from 3×3 to 99×99. For the LRO DTMs were estimated the peak at kernel 33.

The automatic detection was carried out by performing an unsupervised classification (*k-mean*) on *slope* and *curvatures* variables. From this objective classification were defined the boundaries among floor, inner wall, rim and the outer wall of the crater. Afterward a multi band raster mask has been created by reclassifying the *k-mean* raster of *slope* and the *curvatures*. From this raster was possible to create a vectorial layer in *ESRI Arc Map*, necessary for the extraction of all pixel values from each morphological domain.
In this analysis the values of *slope*, *curvatures* and *topographic openness* have been extracted to perform the statistical surface analysis.
When calculating topographic variables from a Digital Terrain Model (DTM), the choice of scale is constrained by the DTM resolution, as well as by the elevation errors present in any DTM. At coordinates x~0, y~0, the *slope* G, *profile curvature kr* and *plan curvature kl* can all be calculated from the parameters of the conic equation [Wood, 1996] as follow:

$$G = \arctan(\sqrt{d^2 + e^2}) \;\; ; \; (rad)$$

$$k_r = \frac{-200(ad^2+be^2+cde)}{(e^2+d^2)(1+d^2+e^2)^{3/2}} \;\; ; \; (l^{-1})$$

$$k_l = \frac{-200(ae^2 + bd^2 - cde)}{(e^2 + d^2)} \;\; ; (l^{-1})$$

RESULTS

Morphometric analysis of Linné crater

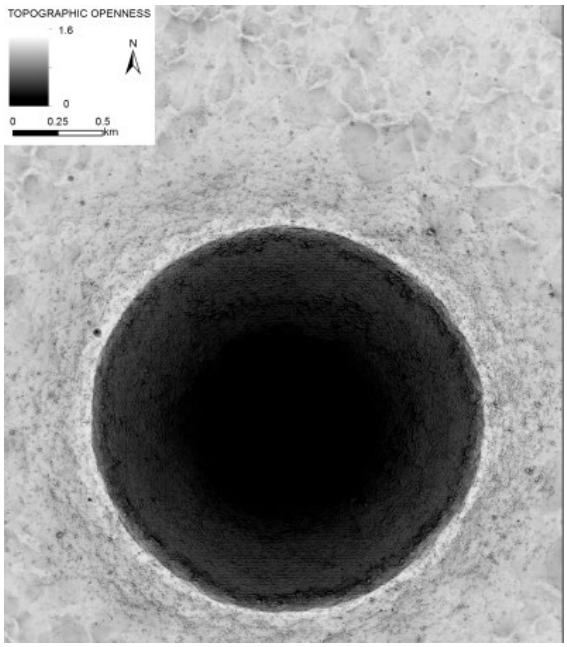

Fig.3 – Topographic openness enlighten the pristine morphology of Linné crater.

The observations performed on the high resolution orthorectified images (0.5m/px) of the crater enlighten its circular and sharp rim crest, which suggests that degradation processes have not yet significantly modified the crater. The wall is clearly interested by a change in albedo located at about 300 m below the rim, involving some sectors of the floor. Deposits on the crater floor are interpreted as a lens of breccia and melts by analogy with terrestrial cases. Such breccia lens is made up by allochthonous material of low level shock, but containing highly shocked melt clasts slumped down from the rim and crater walls [Sharpton, 2014]. The

change in albedo might therefore point to a different material composition.
By measurements on the Linné DTM, we found that the crater is 2.224 km in diameter and 0.52 km in depth, with d/D of 0.23. Linné crater covers an area of about 10 km^2 considering the outer scarp/ejecta border. The four morphological domains cover different areas of the crater, summarized as follow: outer scarp 5.5km^2 (55%), rim crest 0.3 km^2 (3%), inner scarp 4 km^2 (40%) and floor 0.2 (2%).
The outer scarp presents a mean *slope* gradient of about 10°. *Profile curvature* was calculated along the maximum declivity plane and shows a negative value (-0.05) revealing a slightly concave morphology radially from the center of the crater.
The rim sector is characterized by an average *profile curvature* of 0.5, suggesting a convex morphology. Null values of *profile curvature* and *slope* reveal a thin top edge on the rim identifiable as the Linné pristine rim crest. Moreover, the *topographic openness* confirmed this particularly pristine rim crest, enhancing a clear boundary between rim and inner scarp. This characteristic is also distinguishable in the first 50 m of depth of the inner scarp, below the rim edge *Fig.3*. In this section indeed the average *slope* gradient is about 45°-50°, exceeding the global inner scarp mean *slope* of 31.2° and suggesting the presence of an outcrop wall under the rim.
The mean *slope* gradient of inner wall of 31.2° resulted close with the lunar regolith angle of repose (about 31°) [Nickerson et al., 2011] and with the theoretical post-impact morphology of a simple impact crater [Melosh, 1999], confirming the youngness of this morphological structure. At the same time the mean *profile curvature* value is negative, approximately -0.1, suggesting a slightly concave morphology. Moreover, the floor presents a mean slope gradient of 0°- 3°, with a *profile curvature* of 0.05, enlighten a flat floor crater. The floor is interested by some morphological irregularities due to landslides from the bottom of the rim to the floor.
For these particular morphometric characteristics Linné can be classify as a very fresh crater, not eroded by degradation processes.

Detailed analysis of Linné inner scarp

The inner scarp of Linné crater was further investigated in order to understand the pre-impact target surface properties and to confirm a possible evidence of stratigraphic layering.
We processed through a density slice raster the *profile curvature* to enhance the map contrast and isolate any morphological changes on the scarp. This procedure enlightened the presence of three clear changes of curvature within the crater wall. The changing of curvature shown in *fig.4* by black boundaries is the expression of the *slope* gradient variation along the maximum slope direction. If setting the mean elevation of Linné surrounding area (-2620 m) as zero, those boundaries occur as continuous rings at +50, -

100 and -200 m along the inner crater scarp. Convex morphologies on simple crater walls may indeed have different origin, including gravitational landslides or non-homogeneities on the crust stratigraphy. These variations may also be interpreted as the expression of differently layered lava sequences, alternated by strata characterized by different strength. This last hypothesis
is more realistic in the case of Linné crater because the three steps run continuously along the wall, whereas post-impact collapses usually occur as local anomalies. Hence, the three boundaries are characterized by a positive value of the *profile curvature* that may arise from differential erosion on layers with different rheological properties. This difference of strength may affect the erosional processes, producing stepped landforms and suggesting a transition between overlapping geological units (likely lava flows interleaved by regolith or volcanic ashes) in *mare Serenitatis*.

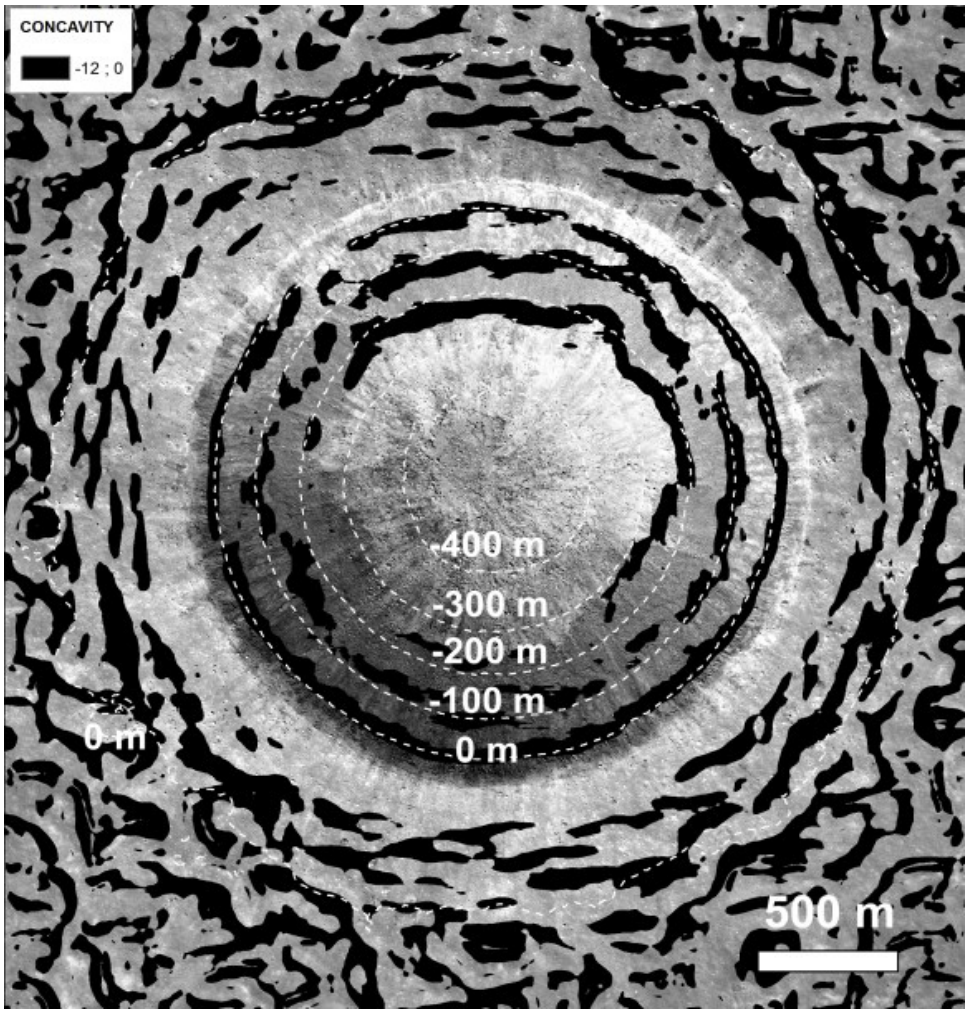

Fig.4- Classification of profile curvature to enhance the morphological steps in the inner scarp, as shown by the three black boundaries.

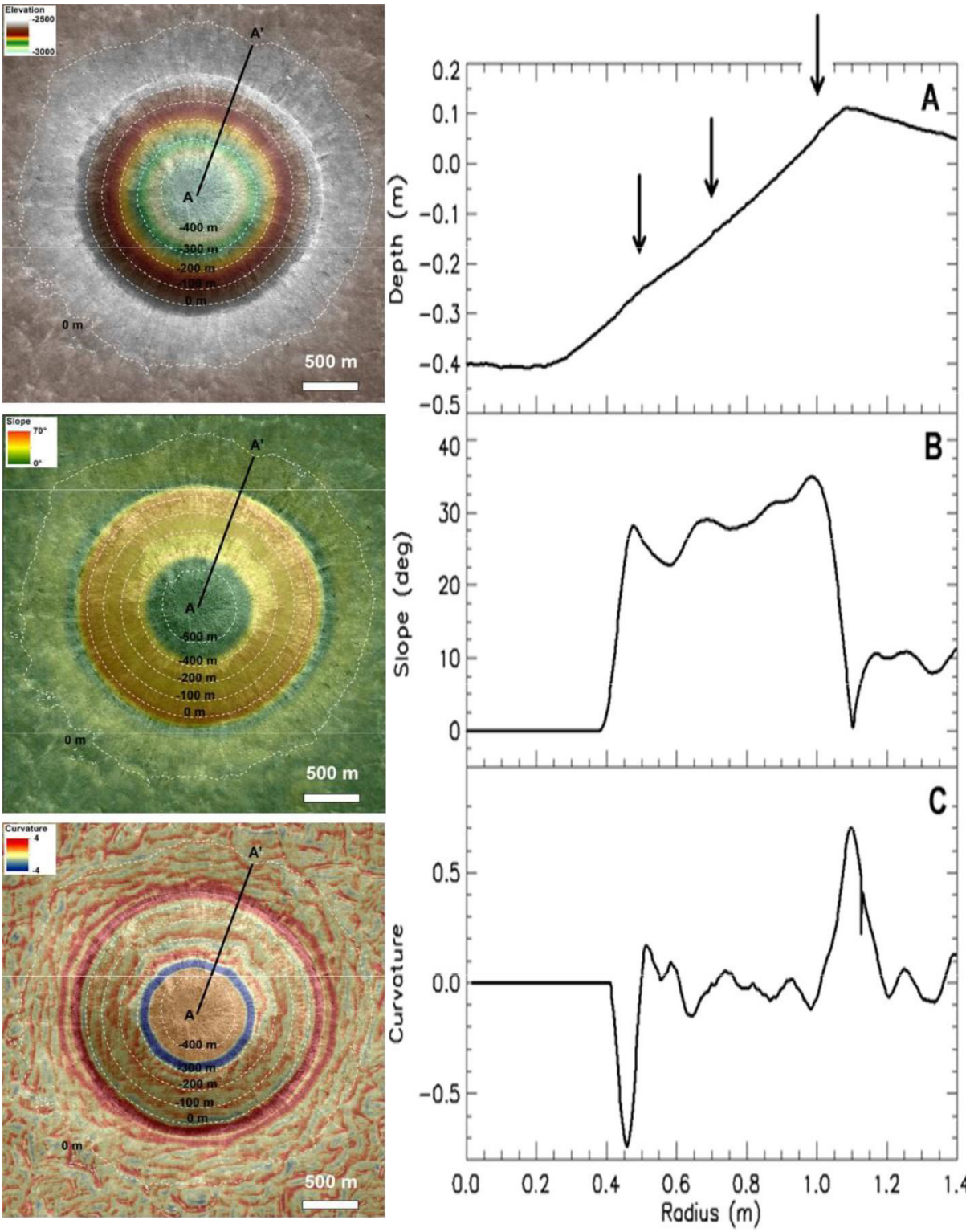

Fig.5-. Profiles of (A) topographic elevation, (B) slope, and (C) profile curvature. Profiles are taken along the line AA'. The arrows indicate the corresponding position along the topographic profile where changes in both slope and profile curvature occur.

CONCLUSIONS

This research shows how morphometric analysis can be useful to detect and quantify the morphology of impact craters. The extraction of pixel values, from different morphometric variables, enable us to calculate surface statistics, in order to quantify different sectors of an impact crater.

In this work we performed a morphometric analysis on the LROC DTM of Linné crater in order to constrain the morphometric signature of a very fresh impact crater. The morphometric signature of Linné crater confirmed its pristine morphology, enlighten that the crater was not strongly modify by degradation processes. For these morphometric characteristics Linné can be considered as a base reference for the morphological analysis of crater degradation classes, as concerning the fresh simple impact craters class C1 [Arthur, 1963].

In addition, we have found the presence of three uphill scarps running along the crater wall. Those features may be the morphological expression of subsequent emplacements of thin lava flows within *mare Serenitatis*, potentially useful to infer the stratigraphy at the impact site, *mare Serenitatis*.

The quantification and classification of morphometric variables described in this research, may be useful also for semi-automatic detection and characterization of the degradation classes of simple craters. This approach could be potentially a helpful tool for the geological mapping of planetary surfaces.

ACKNOWLEDGMENTS

This research was supported by the Italian Space Agency (ASI) within the SIMBIOSYS Project (ASI-INAF agreement no. I/022/10/0)

REFERENCES

Arthur, D.W.G., Agnieray, A.P., Horvath, R.A., Wood, C.A. , Chapman, C.R., 1963. The system of lunar craters. Quadrant I. Comm. Lunar Planet. Lab. 2, #30.

Aasim M. and I.M. Bahuguna, 2014. Depth-diameter ratios of lunar craters from chandrayaan-1 TMC images and DEM and its significance. International Journal Of Geomatics And Geosciences Volume 4, No4; ISSN 0976 – 4380.

Basilevsky A.T., Kreslavsky M.A., Karachevtseva I.P, and Gusakova E.N. 2014. Morphometry of small impact craters in the Lunokhod-1 and Lunokhod-2 study areas. Planetary and Space Science 92, 77-87.

Beyer R.A., 2015. An introduction to the data and tools of planetary geomorphology. Geomorphology 240, 137-145.

Carr M.H., 1966. Geologic map of the mare Serenitatis region of the Moon. Geologic Atlas of the Moon. Department of Interior. US Geological Survey.

Cremonese G., Borin P., Lucchetti A., Marzari F., And Bruno M., 2013. Micrometeoroids flux on the Moon. Astronomy & Astrophysics - 551, A27.

Garvin J.B., Robinson M.S., Frawley J., Tran T., Mazarico E., and Neumann G. 2011. Linné: simple lunar mare crater geometry from LRO observations. 42nd Lunar and Planetary Science Conference (2011), #2063.

Fassett C.I. and Thomson B.J. 2014. Crater degradation on the lunar maria: Topographic diffusion and the rate of erosion on the moon. Journal of Geophysical Research: Planets 119, 2255-2271.

Hapke B. 2001. Space weathering from Mercury to the asteroids belt. J.Geophys.Res., 106, I0039-I0074.

Hiesinger H., J.W. Head, U. Wolf, R. Jaumann and G. Neukum, 2011. Ages and stratigraphy of lunar mare basalts: A synthesis. Geological Society of America Special Papers 2011;477;1-51 doi: 10.1130/2011.2477.

Hiesinger H. and Head J.W. 2006. New views of Lunar geoscience: an introduction and overview. In: Reviews in Mineralogy & Geochemistry 60, 1.81.

Hiesinger H., Head J.W., and Wolf U. 2001. Lunar mare basalts: Mineralogical variations with time. 32nd Lunar and Planetary Science Conference (2001), #1826.

Hiesinger H., Jaumann R., Neukum G., and Head J.W. 2000. Ages of mare basalts on the lunar nearside. Journal of Geophysical Research 105, 29,239-29,275.

Melosh H.J. 2011. Planetary surface processes. Cambridge University Press, 500 p. NASA.

Melosh H.J. and Ivanov B.A. 1999. Impact crater collapse. Annual Review of Earth and Planetary Sciences 27, 385-415.

Melosh H.J. 1989. Impact cratering: A geologic process. New York: Oxford University Press. 245 p.

Melosh, H.J. and Gaffney, E.S. 1983. Acoustic fluidization and the scale dependence of impact crater morphology. J. Geophys. Res. 88, Suppl., A830-A834.

Neukum G. and Horn P. 1976. Effects of lava flows on lunar crater populations. The Moon 15, 205-222.

Neukum G., König B., and Arkani–Hamed J. 1975. A study of lunar impact crater size–distributions. The Moon 12, 201-229.

Pike R.J., 1995. Geomorphometry – progress, practice and pros-pect. Zeitschrift für Geomorphologie, N.F., SupplementBand 101 221–38

Nickerson, R.D.,G.D. Bart,M.T. Lawder,H.J. Melosh, 2011. Global lunar regolith depths revealed. 42nd Lunar and Planetary Science Conference, #2607.

Robinson M.S., Brylow S.M., Tschimmel M., Humm D., Lawrence S.J., Thomas P.C., Denevi B.W., Bowman-Cisneros E., Zerr J., Ravine M.A., Caplinger M.A., Ghaemi F.T., Schaffner J.A., Malin M.C., Mahanti P., Bartels A., Anderson J., Tran T.N., Eliason E.M., McEwen A.S., Turtle E., Jolliff B.L., and Hiesinger H. 2010. Lunar Reconnaissance Orbiter Camera (LROC) Instrument Overview. Space Science Reviews 150, 81-124.

Sharpton V.L 2014. Outcrops on lunar crater rims: Implications for rim construction mechanisms, ejecta volumes and excavation depths. Journal of Geophysical Research 119, 154-168.

Sharpton V.L., Krochuk R.V., and Herrick R.R. 2013. Characterization and morphological reconstruction of the Terny impact structure, central Ukraine. Meteoritics & Planetary Science 48, 806-818.

Tran T., Rosiek M.R., Beyer R.A., Mattson S., Howington-Kraus E., Robinson M.S., Archinal B.A., Edmundson K., Harbour D., Anderson E., and the LROC Science Team 2010. Generating digital terrain models using LROC NAC images. ASPRS/CaGIS.

Vernazza P., Binzel R.P., Rossi A., Fulchignoni M., and Birlan M., 2009. Solar wind as the origin of rapid reddening of asterioid surfaces. Nature, 458, 993-995.

Watters W.A., Geiger L.M., Fendrock M., and Gibson R. 2015. Morphometry of small recent impact craters on Mars: Size and terrain dependence, short-term modification. Journal of Geophysical Research Planets 120, 226-254.

Wilhelms D.E., McCauley J.F., and Trask N.J. 1987. The geologic history of the Moon. USGS Report 1348, 302 p.

Wood, J., 1996. The geomorphological characterization of digital elevation models. PhD Thesis, University of Leicester, UK.

Wood J., 2009. Chapter 14 Geomorphometry in LandSerf. In: Hengl T and Reuter HI (eds), Geomorphometry-Concepts, Software, Applications. Developments in Soil Science, vol. 33, Elsevier, Amsterdam, 333-349.

Yokoyama R, Shirasawa M, Pike R. 2002. Visualizing topography by openness: a new application of image processing to digital elevation models. Photogrammetric Engineering and Remote Sensing 68: 257–266.

CHAPTER 2

GEOMORPHOMETRY OF SIMPLE CRATER DEGRADATION CLASSES ON MARE SERENITATIS

Vivaldi V.[1,2], Ninfo A.[3], Massironi M.[2,1], Cremonese G.[1]

(1) INAF-Astronomical Observatory of Padua, Italy, (2) Dept. of Geosciences, University of Padua, Italy, (3) Dipartimento di Fisica e Scienze della Terra, University of Ferrara, Italy.

ABSTRACT

The classification of impact crater degradation is classically performed through a subjective visual interpretation of lunar surface images. The freshest craters are defined C1 and the more degraded ones are defined as C4 [Arthur et al., 1963]. Here we propose an alternative quantitative methodology based on a morphometric analysis of simple craters carried out on high resolution digital terrain models (DTM) from Lunar Recognisance Orbiter (NASA) and Kaguya-Selene (JAXA) missions.

The morphometric variables such as slopes and curvatures were calculated on a representative fresh (C1) simple crater (Linné), in order to retrieve the morphometric signature of the four main sectors: floor, inner scarp, rim and outer scarp. After we applied the morphometric analysis on other simple impact craters, representative of the last three degradation classes (C2, C3, C4), aiming to constrain the morphometric thresholds pertaining to the four classes of degradation.

After the characterization of the morphometric variables thresholds for the four classes we have conducted the morphometric analysis on 383 impact craters from a unique geological unit on mare Serenitatis (S28-2.84 Gy) [Hiesinger et al., 2011]. The extracted morphometric values allowed a statistical analyses of simple impact craters degradation as function of both the diameter and degradation class. The erosion of lunar impact craters is driven by gravitative processes as well as space weathering, that induce a smoothing effect especially on the rim and on the inner wall of craters. However the inner wall shows the more evident morphologic variations, being the wider sector of a simple crater as well as more susceptible to infilling and flattening processes. A power law trend in mean slope and mean profile curvature changing within the inner wall was discovered in function of diameter within each class. Those power law trends of degradation with decreasing crater size are comparable among the classes and enlighten an upper diameter cut-off for C4 and C3.

INTRODUCTION

Impact craters are the most widespread landforms on rocky bodies surfaces of the Solar System (Melosh, 1989). They are one of the most important geological features that characterize and modify the local and the global morphology of a planetary surface, being an essential element for understanding the formation and the evolution of the Solar System. Indeed the morphologic evolution of a planetary surface results from cumulative effects of subsequent impacts, volcanic emplacements, tectonics, landslides, aeolian activity (in presence of an atmosphere), and space weathering [Neukum et al., 1975].

Impact craters morphology results from the interaction between gravity and target strength under dynamical load [Melosh, 1989, 1999, 2011]. Progressively post-impact modification processes, as for instance crater degradation, might deeply affect the observed morphologies and structures.

To simplify the morphological quantification of crater degradation we have chosen the Moon, avoiding planetary bodies with an atmosphere, where impact craters structures are continuously modified by active effects of erosion, transport and deposition (e.g. Mars). The principal active processes of degradation on the Moon are gravitative processes, dominated by post impact landslides, and space weathering, due to micrometeorites bombardment and cosmic rays alteration [Neukum 1976]. The space weathering is a process of erosion and mineral alteration caused by cosmic, solar rays and micrometeorite bombardment: this process is particularly influenced by micrometeoroids flux [Cremonese et al., 2013; Pieters et al., 2012; Hapke, 2001; Vernazza et al., 2009]. Crater degradation can be used to constrain the chronological evolution of planetary surfaces. On the Moon post-Copernican craters (ages < 1.1 Ga) can be modified only by later impacts which caused rim crest smoothing or collapse, and debris infilling [Garvin et al., 1998], whereas pre Copernican craters were subjected to volcanism infilling and smoothing effects due to erosional processes (e.g. space weathering, gravitational processes).

Lunar impact craters with different degrees of preservation are classified into four classes of degradation, being the C1 referred to fresh craters with well sharp rims and bright ejecta, the C2 to craters with more smoothed rims and a well preserved inner cavity, the C3 to craters with no evidence of rims but with the presence of a cavity, and the C4 to heavily eroded craters with a bland topographic outline of their ancient cavity [Arthur, 1963]. However this classification is based on visual interpretation that is obviously affected by a certain degree of subjectivity.

Indeed the qualitative description of landforms (e.g. hilly, steep, and rough) in Earth geomorphology are subjective and often insufficient for comparative studies [Pike, 1995]. A more robust quantitative approach to empirically describe the shapes of the Earth's surface can facilitate the detailed interpretation of individual landform units and across various landform types. The mathematical description of planetary surfaces and the

extraction of surface-landform parameters are known as Geomorphometry [Pike et Al., 1995, 2002; 2008].
Nowadays morphometric analysis on planetary surfaces is mainly conducted through topographic profiles [e.g., Aasim and Bahuguna 2014, Basilevsky et al. 2014, Fassett and Thomson 2014, Pike 1977, Salamumićcar et al. 2012, Watters et al. 2015] which might not be exhaustive to represent the real 3D surface complexity. This can be instead retrieved by a statistical analysis of morphometric variables, derived from high resolution 3D topography (DTMs).
In this research we considered only simple, circular and symmetric impact craters, to avoid elliptical shapes and irregular morphologies of analysed craters. On the Moon indeed simple impact craters (D<15 km) involved minor modifications of the transient cavity in their formation being represented mainly by flows of breccia and melt along the crater wall to the floor [Melosh, 1999].
Here we propose a morphometric method to objectively determine and quantify the degradation of simple impact craters. In particular we applied a surface analysis based on the geomorphometry to the inner wall sector of each impact crater, with diameter ranging from 0.1 to 12 km, on target area in *mare Serenitatis* (Fig.1). The inner wall is the wider sector of a simple impact crater and its degradation interests a broad area of the crater itself: for this reason the morphologic variations due to degradation processes on the inner wall is more easily quantifiable.

GEOLOGICAL SETTING OF TARGET AREA

For this analysis we have chosen basaltic smooth plain target which can be considered homogeneous from topographic and mechanic point of view, being affected only by the rheological variability between the regolite and the underlying substratum. In particular we have chosen a geological unit in *mare Serenitatis* which is a large multiring basin, located on the nearside of the Moon with a diameter of 920 km [Head, 1979]. Recent works based on crater counting placed *Serenitatis* basin in the *Nectarian* period (3.87 Gy), at the same time of the Late Heavy Bombardment (LHB), when the Moon was exposed to hundred-kilometer size asteroids impacts [Hiesinger 2003, Stöffler et al., 2006]. Mare *Serenitatis* was subdivided into 29 geological units differing in albedo, thickness and spectral properties and belonging to successive lava flows emplaced between 3.81 and 2.44 Ga [Hiesinger et al., 2011].
The stratigraphic sequence characterized by solidified lava flows could reach few kilometers of depth from the *maria* surface, and each geological unit is thick several hundred meters [Pommerol et al., 2010; Weider et al., 2010]. Within mare *Serenitatis* we have chosen unit S28 dated to 2.84 Ga [Hiesinger et al., 2011].

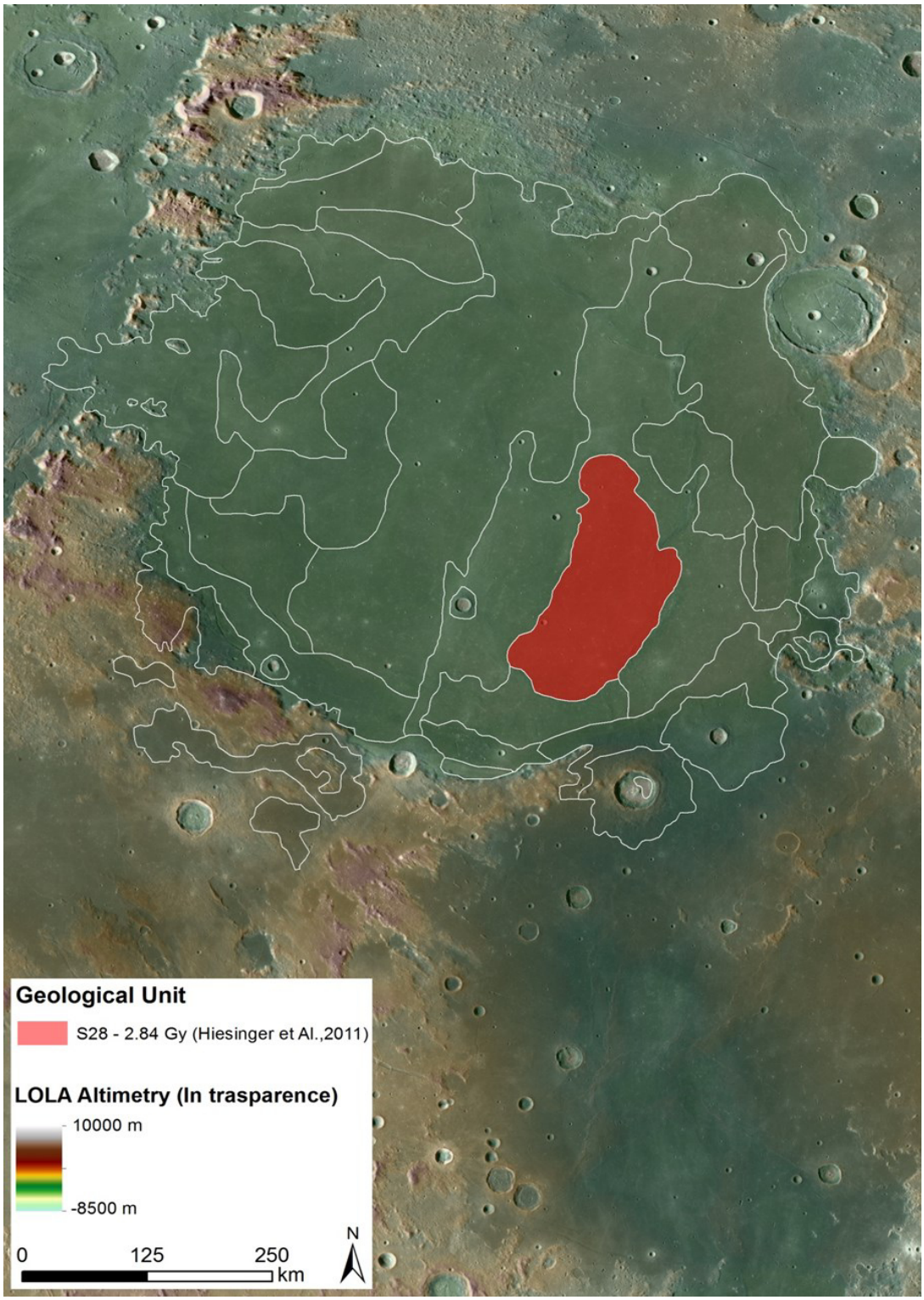

FIG. 1 *– Mare Serenitatis with the geo-chronological units proposed by Hiesinger (2011). The red area indicate the S28 Unit, used as target surface to compare the four degradation classes.*

DATA

We used high resolution DTMs and orthographic products from *Kaguya-Selene* [JAXA] and *Lunar Reconnaissance Orbiter* (LRO) [NASA] missions.
The Japan Aerospace Exploration Agency [JAXA] launched to the Moon the *Kaguya-Selene* spacecraft in September 2007, providing a great amount of data from 2007 to 2009, when the mission ended [Haruyama, J - 2008]. The high-performance optical Terrain Camera (TC), integrated in the Lunar Imager/Spectrometer (LISM) instrument suite, produced a global DTM with 7.4 to 10 meter of spatial resolution [Kato, M., 2007], in addition to the global survey of the Multi-Band Imager (MI, 20 m/pixel) [Isbell et al., 2014]. One of the objectives of TC camera was the production of a high resolution global mosaic, by releasing two morning and two evening near-global tile sets. The morning tile sets covered about 88% of the lunar surface and the evening sets provided about 89% of the spatial coverage. In addition a global orthographic product was produced with gap-filled by the Multi-Band Imager data in order to achieve about 95% of global coverage. We have built a global DTM mosaic of *Serenitatis*, by merging 40 DTMs and orthorectified tiles from TC, with a resolution of 7.4m.
The *Global Lunar* DTM "GLD 100", with a resolution of 100 meters per pixel, was instead produced by LRO and derived from the merging of *Lunar Orbiter Laser Altimeter* (LOLA) and *Wide Angle Camera* (WAC) observations. The "GLD 100" was used as base map to reference the Kaguya-Selene DTM mosaic and to perform a cross-check of the altimetric values.
The *Near Angle Camera* (NAC) onboard LRO produced very high resolution spotted images (0.5 m/pixel) and DTMs (2m/px). This camera was not designed as a stereo system, but stereo pairs can be obtained from acquisitions along two different orbits with at least one off-nadir slew [Beyer et al. 2015]. We employed the high resolution DTMs, acquired by the NAC at different solar illumination conditions between March and October 2010, in order to retrieve the morphometric signature of impact craters representative of the four degradation classes.

METHODS

Morphometric analysis was focused on the calculation and statistical analysis of the first two elevation derivatives, *slope* and *curvatures*. *Curvatures* were calculated along different planes: the *profile curvature* along the maximum slope plane and the *plan curvature* along the horizontal plane.
The *slope* shows wide areas with homogeneous values, such as the inner and the outer wall. The *profile curvature* is instead sensitive to morphologic variations along the maximum plane of declivity, enlightening for example the rim, the floor and the boundary between

inner wall and floor. On the contrary the *plan curvature* is sensitive to morphologic variations orthogonal to the maximum plane of declivity, detecting for example the rim crest (in fresh craters) or dry flows within the inner wall as well as rim interruptions by gravitational collapses.

However the relation among morphometric variables and real landforms strictly depends on the scale and the object ontology, such as the dimension in relation to the surrounding area. Indeed morphometric parameters change continuously over the real landform and they essentially measure an average value related to a certain areal size taken into consideration. The accuracy of morphometric parameters defines the scale of the analysis and depends on the DTM cell size [Albani, 2004]. In fact, in geomorphometry, scale is considered as a function of the resolution of *Digital Elevation Models* (DEMs) [Evans, 2009; MacMillan, 2009].

Another point to consider is the DTM noise, that affect mainly *curvatures* respect to *slope*. In this work we have thus applied a multiscalar approach in order to retrieve *curvatures* reducing DTM errors and noises and maximizing the scale of analysis [Wood, 2009]. One of the main advantages of this approach is the possibility to test and compare a range of different kernel sizes. Kernel has indeed twofold effects: one is the maximization of *curvature* for the specific scale of analysis and the other is the smooth or loss of minor "features", often expression of minor landforms or DTM noise. In other words the larger is the kernel size, the stronger is the smoothing applied to the DTM. The smoothing effect can be useful for the reduction of DTM high frequency noises, derived from random errors [Albani, 2004]. A "*LandSerf*" script was employed to statistically assess the maximum expression of the *profile curvature* for each kernel size, by using the Evans' biquadratic polynomial function to compute the *profile curvature* [Wood, 2009]. Definitely this approach was necessary to evaluate the best kernel size for *curvatures* calculation, balancing the reduction of the propagation of errors in elevation and the expression of the relevant forms.

Multiscalar approach was applied both to *Kaguya* TC DTMs and LROC-NAC DTMs. For the LROC NAC DTMs every kernel sizes from 3x3 to 99x99 were calculated. On LROC DTMs those kernel sizes correspond to windows sizes ranging from $6m^2$ to $198m^2$. The more favorable kernel resulted the 33x33 one, which coincides to a windows area of $66m^2$, as shown in Fig.2. For the *Kaguya* TC DTMs every kernel sizes from 3x3 to 33x33 were tested and the best size calculated was the 15x15 one, which corresponds to a $150m^2$ window area (Fig.2).

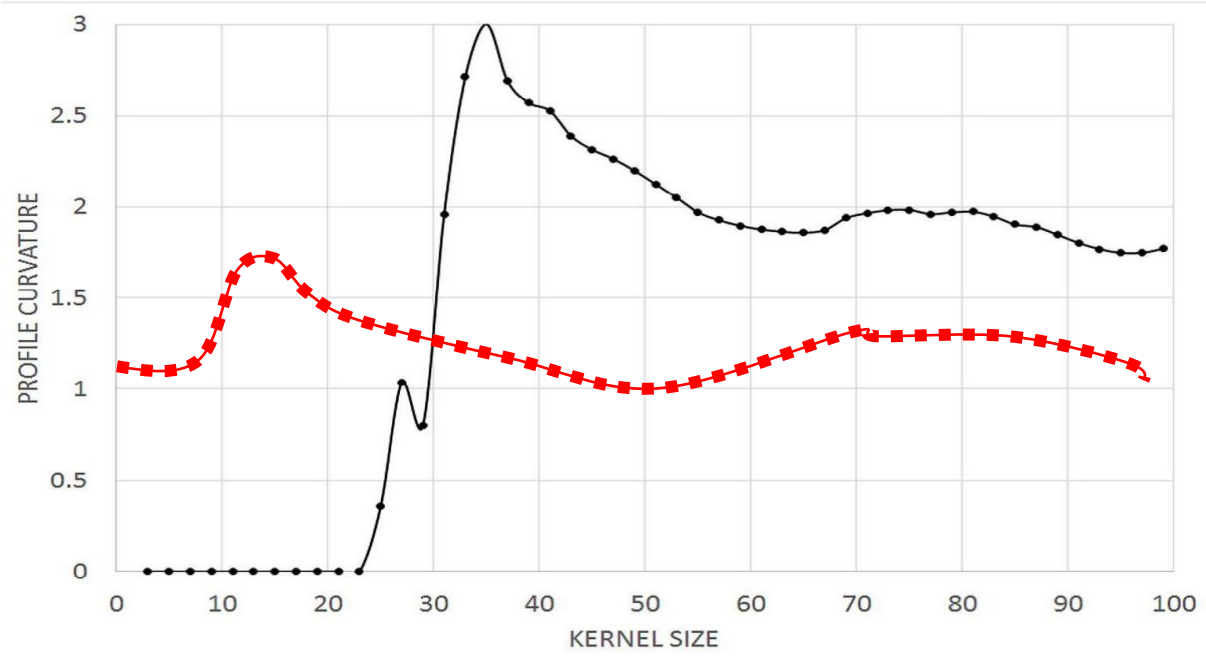

FIG. 2 *– Plots of the maximum expression of the profile curvature at different evaluation kernel sizes for the LRO DTM (black line) and for the Kaguya DTM (red line), testing every kernel sizes from 3×3 to 99×99. For the LRO DTMs were estimated the peak of profile curvature expression on kernel 33, whereas for the Kaguya DTM on kernel 15.*

RESULTS

Morphological characterization of a fresh simple impact crater: Linné crater

Morphometric analyses were firstly conducted on high resolution DTMs from LRO-NAC (2 m/px) in order to quantify the typical crater morphology pertaining to each degradation class (from C1 to C4). The C1class refers to freshest craters, that are very poorly represented in the analysed areas if we consider diameter ranging from 0.8 to 10 km and exclude secondary impact craters.

A fresh crater can be distinguished from its sharp edge and high reflectance ejecta and can be considered as the best natural model for the pristine post-impact morphology of an impact craters [Craddock and Howard, 2000; Head, 1979].

Linné crater is considered in several publications as a paradigm for the fresh simple craters class [e.g., Melosh, 2011; Chappelow, 2013, Martellato et Al., 2017]. The crater is located

at 27.7°N 11.8°E, near the western edge of *Mare Serenitatis*, presenting a diameter of 2.220 km, a depth 0.520 km and a d/D ratio of 0.23.

In this work we automatically subdivided the fresh crater into its four homogeneous morphologic domains (outer and inner wall, rim and floor) through an unsupervised classification, using the three morphometric variables exposed above (*slope*, *profile curvature* and *plan curvature*) (Fig.3). The product of this classification was a raster mask, capable to detect and extract values from the four morphologic domains of the crater.

Using the obtained mask to extract values we found that the crater covers an area of about 10 km^2 considering the outer scarp border. The crater area is subdivided into four sub-areas, pertaining to the outer scarp which covers 4.6 km^2 (46% of the total area), the rim which covers 0.7 km^2 (7% of the total area), the inner scarp covering 3.5 km^2 (35% of the total area) and the floor which is of 0.2 km^2 (2% of the total area) [Vivaldi et al., 2016]. Afterward, in order to establish the specific geomorphometric aspects of the four sectors of a fresh impact crater, we extracted morphometric values. We calculated the mean *slope* and *curvature* values, which were representative for each sector (rim crest, inner and outer wall, floor), effectively quantifying the morphology of each domain of Linné crater as follows.

The outer scarp presents a mean slope of ~10°. The profile curvature calculated along the maximum inclination plane is negative (-0.05), revealing a slightly concave morphology. The rim has a mean slope of about 45-50°, that is typical of a not eroded outcrop, and presents an average value of profile curvature of 0.5 (convex morphology). A subsection area of the rim, which denotes the top of such sector, has a mean slope approximating 0°, identifying the rim crest. The inner scarp has a mean *slope* gradient of the of 31.2° and resulted coherent with the lunar regolith angle of repose (about 31° [Nickerson et al., 2011]), whereas the mean *profile curvature* value of -0.1 suggests a slightly concave morphology. These morphologic characteristics highlight the very pristine nature of Linné crater, and therefore they can be representative of highly fresh craters which have not undergone any kind of heavy degradation process [Vivaldi et al., 2016].

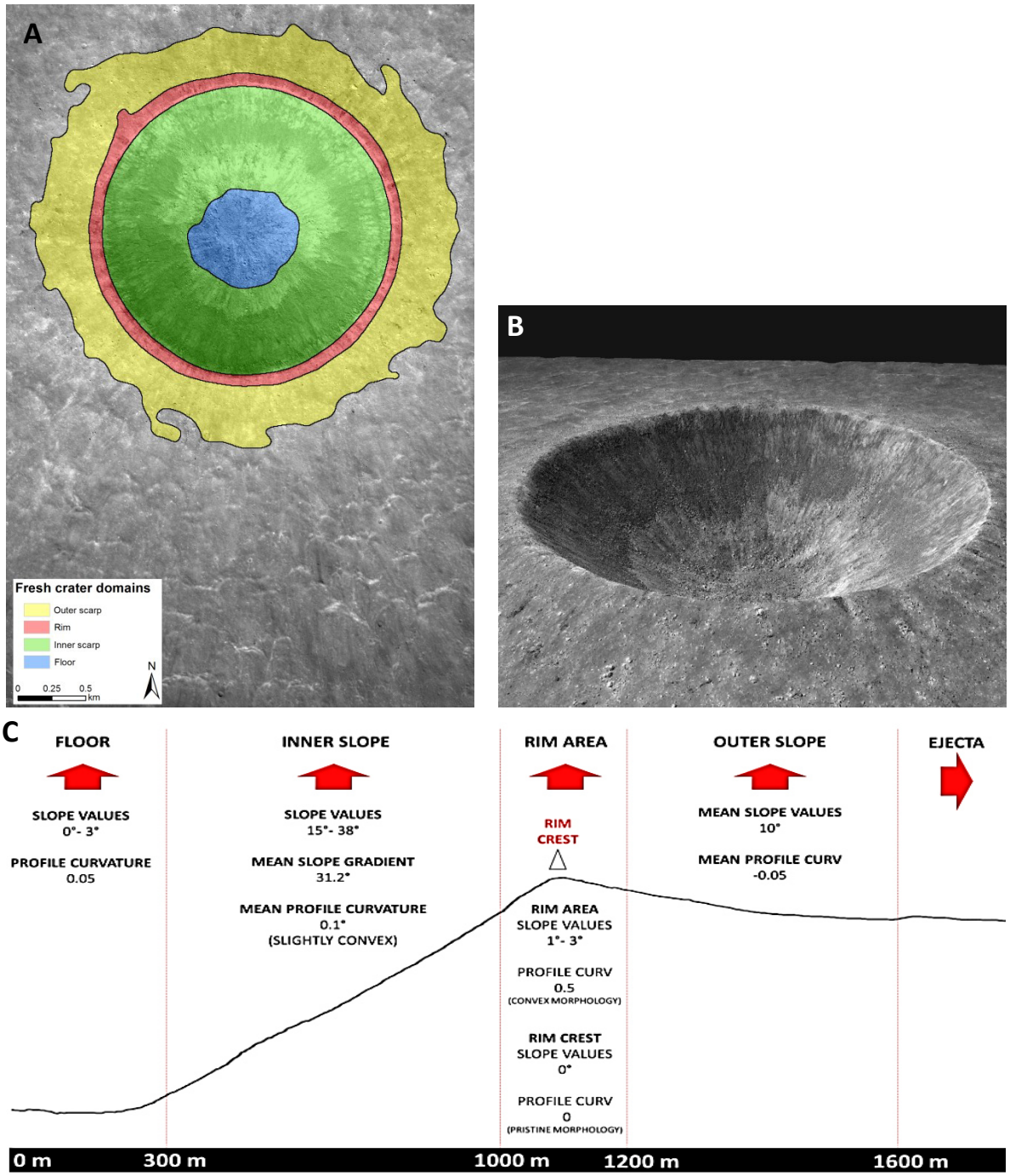

FIG. 3 *– A) K-mean classification derived by merging slope, profile curvature and planar curvature from Linnè crater DTM. This classification allows the numerical subdivision of a simple impact crater into the four sectors (outer scarp, rim, inner scarp and floor). B) 3D visualization of Linné crater from LRO-NAC observations. C) Topographic profile of Linnè crater with the principal morphometric variables thresholds.*

Automatic detection of the four morphological domains of simple impact craters

Using Linné crater as a morphometric reference for the simple impact crater morphology we have conducted a morphometric analysis on the other three degradation classes (C2, C3, C4).

At this purpose we chose three impact craters with diameters similar to Linné crater and representative of C2 (*NAC DTM IMBRIUM E287N3336*), C3 (*NAC DTM HARDINGH E400N2962*) and C4 (*NAC DTM RUMKERDOME2 E400N3010*).

Density slices of *slope* gradients applied on the four resulting *slope* maps revealed, as expected, how the rim crest tends to enlarge and smooth and the inner wall to lose *slope* gradient, with the increase of the degradation (Fig.4). Even though each morphologic domain of a simple impact crater is influenced by degradation, the inner wall showed the more significant morphologic modifications. Erosional processes indeed tend to flatten the inner wall, concurrently with the rim crest erosion and floor infilling. The main result is a progressive global smoothing effect of the crater morphology, as shown in Fig.4. Thus we have quantified the relation between diameter and the inner wall mean *slope* gradient, as a function of crater degradation.

The extraction of the morphometric variables from each pixel of the more degraded craters confirmed this degradation trend (Tab.1). Indeed C2 crater analyses presented an inner wall mean *slope* gradient reduction up to ~24°, whereas C3, which refers to more degraded craters without a defined rim, present an inner wall filled by deposits and a substantial loss of *slope* gradient (around 16°). The C4 class represents craters totally eroded, without a rim, but identifiable only through a little topographic depression. In this case a mean *slope* value of inner wall is around 7°. We have identified the C4 crater ancient rim area, which no longer displays a rim crest, but is rather a slightly degrading slope of 1.4° on average. Moreover a bland topographic feature around the residual inner scarp with a mean *slope* lower than 2°, identifies the presence of the ancient rim by now totally eroded.

Tab.1 summarizes all the mean *slope* values for each degradation class, as well as the min-max values and their range. The decrease of the mean *slope* values from C1 to C4 shows how the inner slope loses its declivity, with the increase of degradation. A maximum *slope* value around 70° on C1 may prove the presence of pristine outcrops in the inner wall, that are smoothed in C2, being the maximum *slope* value around 60°, and disappear in the other classes. Tab.1 allowed us to establish mean *slope* gradient thresholds of inner wall, in order to build different extraction masks for the automatic detection and morphometric characterization of the degradation classes.

CLASS	DTM	COORDINATES (DMS)	INNER WALL MEAN SLOPE
C1	NAC DTM LINNECRATER E280N0120 (*Linné*)	11°47'42.55"E 27°44'57.726"N	31.20°
C2	NAC_DTM_IMBRIUM_E287N3336.IMG	26°5'46.563"W 29°20'5.745"N	24.26°
C3	NAC_DTM_HARDINGH_E400N2962.IMG	63°48'23.627"W 39°37'5.466"N	16.46°
C4	NAC_DTM_RUMKERDOME2_E400N3010.IMG	59°8'8.24"W 40°41'34.294"N	7.58°

TAB.1*: mean slope values calculated from the four DTMs pertaining to four simple impact craters, representative of the C1 to C4 classes. The table fields are related to the degradation classes, the name of the DTM raster (PDS), the slope mean value.*

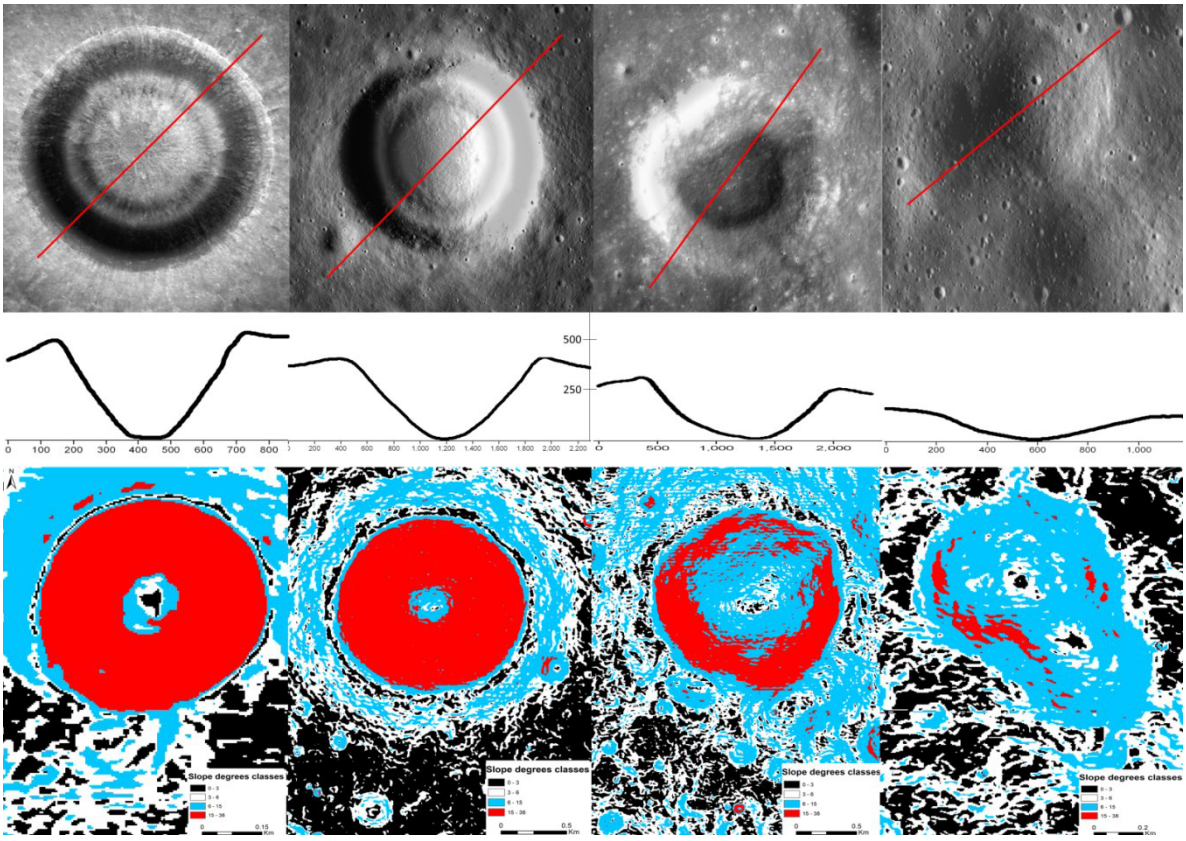

FIG. 4 *– Orthoimages (top) of the four simple impact craters representative of the four degradation classes. Topographic profiles (center) , calculated on DTMs show the flattening effect due by degradation. The slope density slice (bottom) shows the evolution of degradation from C1 to C4 class (from left to right). The rim crest tends to smooth and enlarge its morphology, whereas the inner wall tends to strongly reduce its declivity increasing the crater infilling.*

Degradation classes morphometry comparison

After having characterized the typical mean *slope* values for each degradation class we extended the morphometric analysis to a unique geological unit on Serenitatis basin.
We have chosen a restricted area of about 23000 km^2 on the S28 unit, that is located in the central part of mare *Serenitatis*. The composition of S28 is basaltic and has an absolute model age of 2.84 Ga [Hiesinger et al., 2011]. From this area we have mapped 383 simple impact craters, with diameters ranging from 0.1km up to 12 km (Fig.5). Impact craters with a diameter lower than 0.1 km have not enough pixels on the *Kaguya TC* DTM mosaic to assure significant morphometric statistic. On the other side diameters of 12 km define the transition from simple to complex craters.
Afterward we subdivided the craters into the four degradation classes (Tab.2) by applying the characteristic inner wall mean *slope* calculated in the previous high resolution topographic analysis. For each class was considered a buffer of ±5° centered on the mean *slope* values of the class: C1=31°, C2=24°, C3=20°, C4=15°.
To be sure of this objective classification we verified the results through the visual interpretation of orthoimages (cell size 0.5m/px).

CLASS	**NUMBER**
C1	106
C2	79
C3	157
C4	41
TOTAL	383

TAB.2: *extracted craters.*

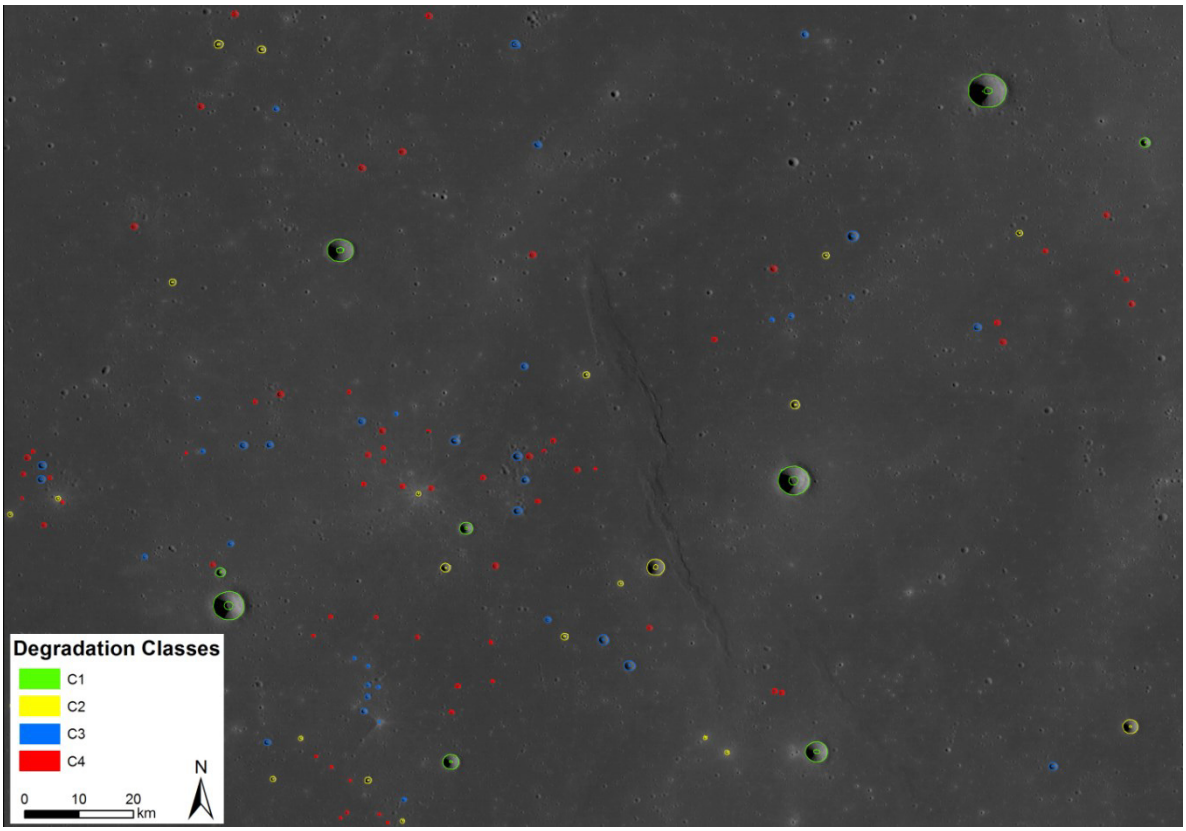

FIG. 5 *– Detail of S28 Unit with the vectorial extraction masks subdivided for the four degradation classes.*

Slope analysis

C1 larger craters have *mean* slope values approximating the regolite angle of repose, between 31° and 32°, whereas craters with diameter <100m of the same class show a mean slope ranging from 18° and 20°.

The resulting distribution of inner walls *slope* values shows a degradation trend within the first three. The first three degradation classes indeed follow a comparable power law trend: the mean *slope* increases from small to large diameters, as shown in the inner wall mean *slope/diameter* ratio diagram (Fig.6). C4 class is instead characterized by a wide dispersion of the data. This is due to the bland topographic expression and the mainly irregular morphology of the most degraded craters.

The *slope/diameter* diagram shows also a diameter upper cut-off at about 1 km size, for the most degraded crater class (C4). This is most probably due to the relative young age of the unit considered in *mare Serenitatis* [Hiesinger et Al., 2011], that does not allow larger craters to be degraded up to C4 class. In fact the diameter upper cut-off is present to all the degradation classes, shifting to larger craters from C4 to C1.

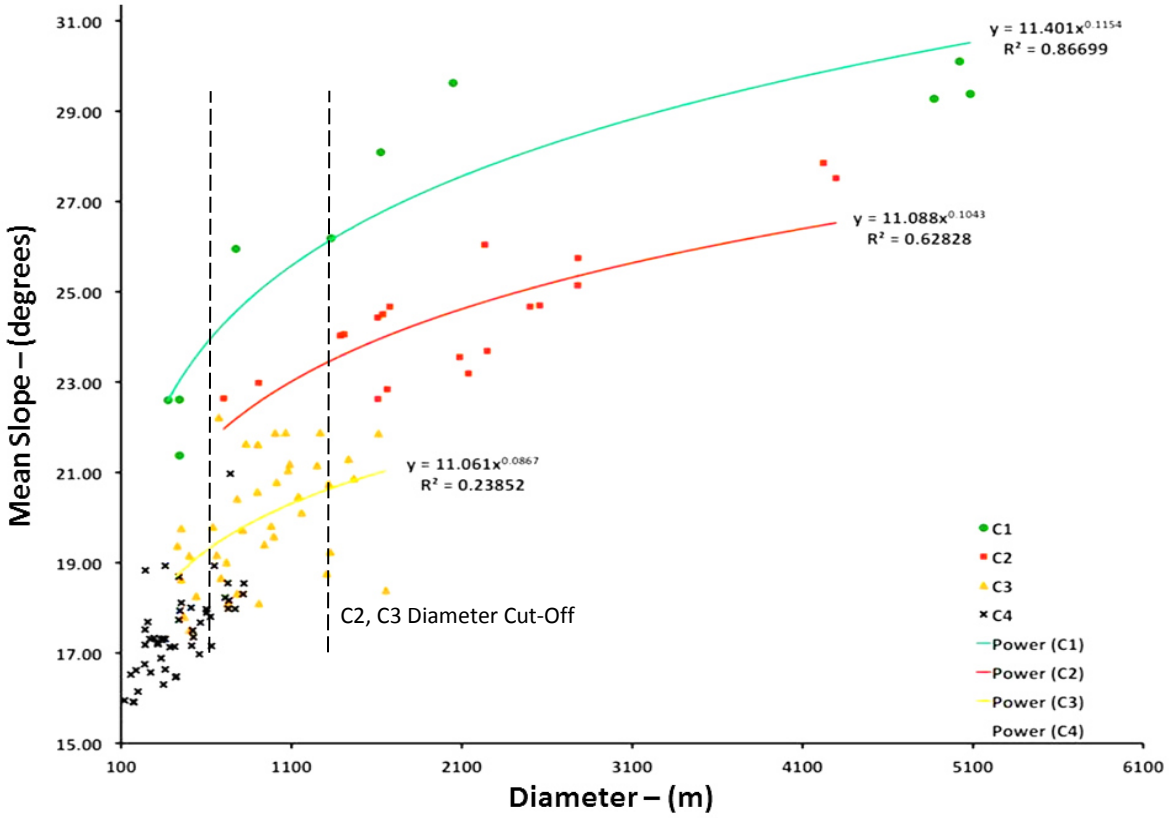

FIG. 6 *– Inner scarp mean slope values plotted in relation to crater diameter derived from the extraction of craters. The plot shows a power law trend enlightening how the inner wall of the small diameter craters presents low values of mean slope. This trend can be explained with a stronger erosion rate on small diameter craters that are subjected to a more quick degradation. The plot shows also a diameter upper cut-off at about 1 km size, related to the most degraded crater class (C4).*

Concavity analysis

The analysis of *curvatures* was conducted isolating the negative values of *profile curvature* (*concavity*) from the positive ones (*convexity*). This was obtained by applying a masking binary raster containing only negative values, in order to analyze only the *concavity* trends within the inner wall of the impact craters.

After the extraction we plotted the mean *concavity* values of each crater, in function of its diameter and the diagram was subdivided into the four degradation classes, alike the *slope/diameter* diagram (Fig.7).

The distribution of the negative *profile curvature* values follows a similar power law trend for C1 and C2, which becomes less defined for C3 and disappear in C4. This enlightens

how the *concavity* along the inner wall tends to decrease in function of degradation class from C1 to C4, according with a flattening morphological evolution from less degraded to more degraded craters.

Considering the relation between the mean *concavity* and the diameter is clear how the *concavity* is inversely proportional to the increase of the diameter size. In other words larger and more degraded craters tend to a flatten morphology (profile curvature approximate to 0) and might eventually reach a positive *profile curvature* expression (*convexity*).

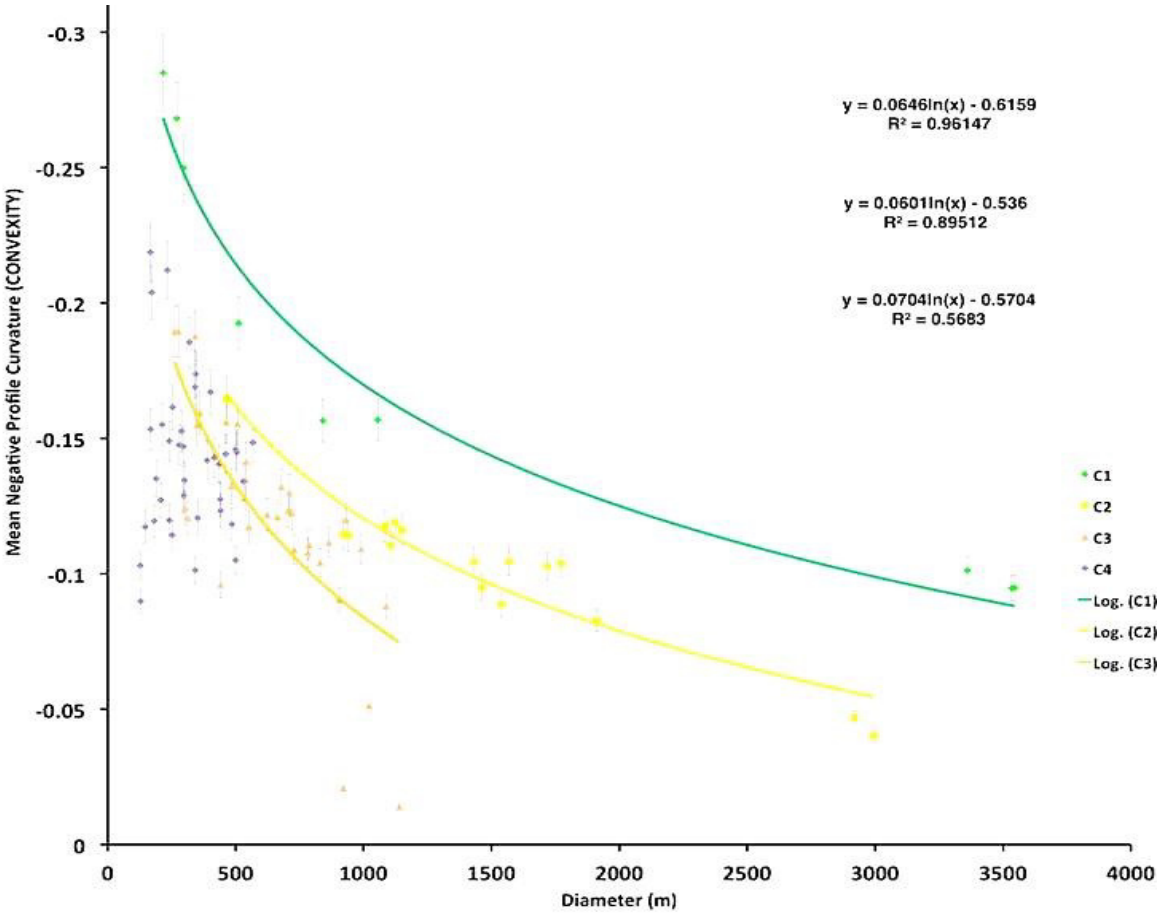

FIG. 7 - Distribution of negative profile curvature values (concavity). The plot shows a power law trend for C1 and C2, that become less clear on C3 and disappear on C4. This enlightens how the convexity along the inner wall tends to decrease in function of degradation class from C1 to C4, according with a flattening morphological evolution from less degraded to more degraded craters. In addition larger craters show a flatten morphology along the inner wall (profile curvature approximate to 0) and might eventually reach a positive profile curvature expression (convexity) (see more details within the text).

DISCUSSIONS

The statistical distribution of the inner wall mean *slope* highlighted a plausible power law trend in function of the diameter, at least for C1, C2 and C3 classes, whereas C4 class is affected by the maximum degree of degradation exhibiting a low topographic relevance. Craters with larger diameter (>4 km) in C1 and C2 show clear differences in terms of ejecta albedo and rim sharpness on the visual interpretation in the orthoimages, although the topographic analyses measure bland morphologic variations of the inner wall as enlighten in the plot of Fig.6. Hence in the first step of crater degradation the rim crest erosion probably prevails, whereas in the following steps the continuous infilling of the inner wall becomes topographically more important. However the gap among C1 and C2 improve when the crater diameter decrease under 3km, making topographic variations more evident. This trend may be related to the velocity of erosional processes on lunar impact craters, becoming quicker from large craters to small ones. Small impacts involve mainly the regolite and the fractured uppermost layers of lunar crust generating impact craters with blender morphologies. Hence the inner scarp of small impact craters interests materials with a lower strength than the basalts, being more affected to gravitative phenomena and erosional processes.

The inner wall mean *slope* of C1larger craters approximates the regolith angle of repose, about 31° [Nickerson et Al., 2011]. This is coherent with the relatively freshness crater morphology, shaped only by early post impact modifications. However <200m sized craters of C1, show very bright ejecta and radial rays typical of fresh craters, present a mean *slope* value within the inner wall ranging from 18° to 20°, more typical of C3 mean values (14°-18°) than C1 (28°-32°). This is probably related to the mechanics of small impacts that involve exclusively regolith layers, which have a lower strength if compared to basaltic layers and the resulting impact morphology is blander. Moreover in the post impact phase the regolith is probably much more prone to landslides and collapses of the inner scarp, as well as more susceptible to weathering processes. The distribution of impact craters revealed a diameter upper cut-off out 1 km for the most degraded crater class (C4). This cut-off can be explained probably with the relative young age of the considered units in mare Serenitatis [Hiesinger et al., 2011], that does not allow larger craters to be degraded up to C4 class. Indeed the diameter upper cut-off is present to all the degradation classes and increase to larger craters from C4 to C1. This cut-off will potentially allow a refinement of relative age discrimination among different geological units, with similar absolute model ages.

The mean *concavity* diagram (Fig.7) shows how the *concavity* decreases with growing diameter and increasing degradation status of impact craters. In general degradation processes reduce inner wall *concavity*, decreasing the *slope* gradient with the simultaneous crater infilling. Sediments from dry-flows, landslides and potential material ejected from

surrounding impact events, tend to fill up the crater, supporting the increase and finally the prevalence of positive *profile curvature* values for the more degraded craters (C4). Craters also exhibit decreasing *concavity* with increasing diameters. These results can be explained under the light of the mechanic of impact that lead to more concave morphologies for small craters (bowl shaped floors and concave inner walls), to steep and sharp inner walls and flattened floors for larger craters, in particular at diameter closest to the transition with complex craters [Wilhelms, 1987; Melosh, 1989]. In addition larger craters are also interested by major and deeper gravitational events which might deform the carter floor at their foot leading to more irregular morphologies.

CONCLUSIONS

In this research we have applied morphometric analysis on high resolution topographic data in order to quantify the degradation of simple impact craters. We firstly derived and measured the morphological expression of the four different crater domains: the outer and inner wall, the rim and the floor. For this purpose we have chosen a particular fresh impact crater (Linné) as a reference for the quantification of the four homogeneous morphological domains. We applied the same analysis to other three simple impact craters, representative respectively of C2, C3 and C4 classes, in order to set up the characteristic thresholds of the four degradation classes. Afterwards we applied morphometric analysis on several simple craters on mare *Serenitatis*. Our results have provided a quantitative distinction among different crater classes and have shown common trends of degradation, going from larger to smaller craters within each class.

The statistical distribution of the inner wall mean *slopes* highlights a similar power law trend of the first three degradation classes, which seems independent from the degradation class.

We have also found a diameter upper cut-off at about 1 km of the most degraded crater class (C4), which can be explained with the relative young age of the considered unit in mare *Serenitatis* [Hiesinger et al., 2011], for which there were not enough time useful to degrade large craters up to C4 class. Indeed the diameter upper cut-off is present on all the degradation classes and increases from C4 to C1. This cut-off will potentially allow a refinement of relative age discrimination among different geological units, with similar and different absolute model ages.

The shape evolution of simple impact craters inner wall was suggested by the negative *profile curvature* distribution, that shown a trend in function of diameter that enlightens a decreasing of mean *concavity* with both increasing diameters and raising degradation status: larger and more degraded craters have lower *concavities* and might eventually reach positive *profile curvatures* (*convex* shape).

The development of morphometric variables classification described in this research, may be also useful for semi-automatic detection and characterization of the degradation classes of simple craters, potentially helpful for geological mapping and age determination of planetary surfaces.

AKNOWLEDGEMENTS

This research was supported by the *Italian Space Agency* (ASI) within the SIMBIO-SYS Project (ASI-INAF agreement no. I/022/10/0).

REFERENCES

Albani, M. , Klinkenberg, B. , Andison, D.W. and Kimmins, J.P., 2004: The choice of window size in approximating topographic surfaces from digital elevation models . International Journal of Geographic Information Science 18, 577—93.

Arrell K.E., Fisher PF, Tate NJ and Bastin L, 2007, A fuzzy c-means classification of elevation derivatives to extract the morphometric classification of landforms in Snowdonia, Wales. Computers & Geosciences, 33:1366-1381.

Arthur, D.W.G., Agnieray, A.P., Horvath, R.A., Wood, C.A. , Chapman, C.R., 1963. The system of lunar craters. Quadrant I. Comm. Lunar Planet. Lab. 2, #30.

Aasim M. and I.M. Bahuguna, 2014. Depth-diameter ratios of lunar craters from chandrayaan-1 TMC images and DEM and its significance. International Journal Of Geomatics And Geosciences Volume 4, No4; ISSN 0976 – 4380.

Basilevsky A.T., Kreslavsky M.A., Karachevtseva I.P, and Gusakova E.N. 2014. Morphometry of small impact craters in the Lunokhod-1 and Lunokhod-2 study areas. Planetary and Space Science 92, 77-87.

Beyer R.A., 2015. An introduction to the data and tools of planetary geomorphology. Geomorphology 240, 137-145.

Chappelow J.E. 2013. Simple impact crater shape determination from shadows. Meteoritics & Planetary Science 48, 1863-1872.

Craddock R.A. and Howard A.D., 2000. Simulated degradation of lunar impact craters and a new method for age dating farside mare deposits. Journal of Geophysical Research 105, 20,387-20,401.

Cremonese G., Borin P., Lucchetti A., Marzari F., And Bruno M., 2013. Micrometeoroids flux on the Moon. Astronomy & Astrophysics - 551, A27.

Drăguţ L, Schauppenlehner T, Muhar A, Strobl J and Blaschke T, 2009, Optimization of scale and parametrization for terrain segmentation: an application to soil-landscape modeling. Computers & Geosciences, doi:10.1016/j.cageo.2008.10.008

Evans I.S., Hengl T. and Gorsevski P., 2009. Chapter 22 Applications in Geomorphology. In: Hengl T and Reuter HI (eds), Geomorphometry-Concepts, Software, Applications. Developments in Soil Science, vol. 33, Elsevier, Amsterdam, 497-525.

Evans I.S., 1998. What do terrain statistics really mean? In: S.N. Lane, K.S. Richards, J.H. Chandler (eds), Landform monitoring, modelling and analysis, Wiley Publications, 119-138.

Evans I.S., 2003. Scale-Specific Landforms and Aspects of the Land Surface. Eds. I. S. Evans, R. Dikau, E. Tokunaga, H. Ohmori and M. Hirano, pp. 61–84. Tokunaga E, Ohmori H and Hirano M (eds), Concepts and Modelling in Geomorphology: International Perspectives. Terrapub, Tokyo, 61-84.

Fassett C.I., Head J.W., Kadish S.J., Mazarico E., Neumann G.A., Smith D.E., and Zuber M.T. 2012. Lunar impact basins: Stratigraphy, sequence and ages from superposed impact crater populations measured from Lunar Laser Altimeter (LOLA) data. Journal of Geophysical Research 117, E00H06.

Fassett C.I. and Thomson B.J. 2014. Crater degradation on the lunar maria: Topographic diffusion and the rate of erosion on the moon. Journal of Geophysical Research: Planets 119, 2255-2271.

Florinsky I.V. and Kuryakova G.A., 2000, Determination of grid size for digital terrain modelling in landscape investigations - exemplified by soil moisture distribution scale. International Journal of Geographical Information Science, 14:815-832

Garvin J.B. and Frawley J.J. 1998. Geometric properties of Martian impact craters: Preliminary results from the Mars Orbiter Laser Altimeter. Geophysical Research Letters 25, 4405-4408.

Garvin J.B., Robinson M.S., Frawley J., Tran T., Mazarico E., and Neumann G. 2011. Linne: simple lunar mare crater geometry from LRO observations. 42nd Lunar and Planetary Science Conference (2011), #2063.

Hapke B. 2001. Space weathering from Mercury to the asteroids belt. J.Geophys.Res., 106, I0039-I0074.

Haruyama, J., Matsunaga T., Ohtake M., Morota T., Honda C., Yokota Y., Torii M., Ogawa Y., and the LISM Working Group (2008. Global lunar-surface mapping experiment using the Lunar Imager/Spectrometer on SELENE. Earth Planets Space, 60, 243- 255.

Hartmann W.K. and Wood C.A. 1971. Moon: origin and evolution of multi-ring basins. The Moon 3, 3-78.

Head J.W. 1979. Serenitatis multi-ringed basin: regional geology and basin ring interpretation. The Moon and the Planets 21, 439-462.

Hengl T., 2006. Finding the right pixel size. Computers & Geosciences, 32:1283–1298.
Hiesinger H., J.W.Head, U. Wolf, R. Jaumann and G. Neukum, 2011. Ages and stratigraphy of lunar mare basalts: A synthesis. Geological Society of America Special Papers 2011;477;1-51 doi: 10.1130/2011.2477(01).
Hiesinger H. and Head J.W. 2006. New views of Lunar geoscience: an introduction and overview. In: Reviews in Mineralogy & Geochemistry 60, 1.81.
Hiesinger H., J. W. Head III, U. Wolf, R. Jaumann, and G. Neukum, 2003. Ages and stratigraphy of mare basalts in Oceanus Procellarum, Mare Nubium, Mare Cognitum, and Mare Insularum, J. Geophys. Res., 108, 5065, doi:10.1029/2002JE001985, E7.
Hiesinger H., Head J.W., and Wolf U. 2001. Lunar mare basalts: Mineralogical variations with time. 32nd Lunar and Planetary Science Conference, #1826.
Hiesinger H., Jaumann R., Neukum G., and Head J.W. 2000. Ages of mare basalts on the lunar nearside. Journal of Geophysical Research 105, 29,239-29,275.
Isbell C., Gaddis L., Garcia P., Hare T., and Bailen M., 2014. Kaguya Terrain Camera mosaics. 45th Lunar and Planetary Science Conference, Abstract #2268.
Kato, M., Y. Takizawa, and S. Sasaki, 2007. LPS XXXVIII, Abstract #1402.
Mahanti P., Robinson M.S., Humm D.C., and Stopar J.D. 2014. A standardized approach for quantitative characterization of impact crater topography. Icarus 241, 114-129.
MacMillan RA and Shary PA, 2009, Chapter 9 Landforms and landform elements in geomorphometry. In:Hengl T and Reuter HI (eds), Geomorphometry-Concepts, Software,Applications. Developments in Soil Science, vol. 33, Elsevier, Amsterdam, 227-254.
Martellato E., V. Vivaldi, G. Cremonese, M.Massironi, A. Ninfo, F. Marzari, J. Haruyama. Is Linné morphology influenced by the lunar stratigraphy? Insights from numerical modeling. Submitted to Meteoritics & Planetary Science, ISSN: 1945-5100 - Under review 2016.
Melosh H.J. 2011. Planetary surface processes. Cambridge University Press, 500 p. NASA
Melosh H.J. and Ivanov B.A. 1999. Impact crater collapse. Annual Review of Earth and Planetary Sciences 27, 385-415.
Melosh H.J. 1989. Impact cratering: A geologic process. New York: Oxford University Press. 245 p.
Melosh, H.J. and Gaffney, E.S. 1983. Acoustic fluidization and the scale dependence of impact crater morphology. J. Geophys. Res. 88, Suppl., A830-A834.
Neukum G., 1983. Meteoritenbombardement and datierung planetarer oberfluchen. Habilitation Dissertation for Faculty Membership, University of Munich. 186 pp.
Neukum G. and Ivanov B. A., 1994. Crater size distribution and impact probabilities on Earth from lunar, terrestrial-planet, and asteroid cratering data. In Hazards Due to Comets and Asteroids (T. Gehrels, ed.), pp. 359–416. Univ. of Arizona, Tucson.
Neukum G. and Horn P. 1976. Effects of lava flows on lunar crater populations. The Moon 15, 205-222.

Neukum G., König B., and Arkani–Hamed J. 1975. A study of lunar impact crater size–distributions. The Moon 12, 201-229.

Nickerson, R.D.,G.D. Bart,M.T. Lawder,H.J. Melosh, 2011. Global lunar regolith depths revealed. 42nd Lunar and Planetary Science Conference, #2607.

Pieters C.M. and 16 colleagues, 2012. Distinctive space weathering on Vesta from regolith mixing processes. Nature, 491, 79-82.

Pike R.J., I.S. Evans and T. Hengl, 2008. Geomorphometry: A Brief Guide. Developments in Soil Science, Volume 33 © 2009 Elsevier B.V.

Pike R.J., 2002. A bibliography of terrain modeling (geomorphometry), the quantitative representation of topography — supplement 4.0. Open-File Report 02-465. U.S. Geological Survey, Denver, 116 pp. http://geopubs.wr.usgs.gov.

Pike R.J., 1995. Geomorphometry – progress, practice and pros-pect. Zeitschrift für Geomorphologie, N.F., SupplementBand 101 221–38

Pike R.J. 1974. Depth/diameter relations of fresh lunar craters – Revision from spacecraft data. Geophysical Research Letters 1, 291-294.

Pommerol A., Kofman W., Audouard J., Grima C., Beck P., Mouginot J., Herique A., Kumamoto A., Kobayashi T., and Ono T. 2010. Detectability of subsurface interfaces in lunar maria by the LRS/SELENE sounding radar: Influence of mineralogical composition. Geophysical Research Letters 37, L03201.

Robinson M.S., Brylow S.M., Tschimmel M., Humm D., Lawrence S.J., Thomas P.C., Denevi B.W., Bowman-Cisneros E., Zerr J., Ravine M.A., Caplinger M.A., Ghaemi F.T., Schaffner J.A., Malin M.C., Mahanti P., Bartels A., Anderson J., Tran T.N., Eliason E.M., McEwen A.S., Turtle E., Jolliff B.L., and Hiesinger H. 2010. Lunar Reconnaissance Orbiter Camera (LROC) Instrument Overview. Space Sceince Reviews 150, 81-124.

Salamunićcar G., Lončarić S., and Mazarico E. 2012. LU60645GT and MA132843GT catalogues of Lunar and Martian impact craters developed using a Crater Shape-based interpolation crater detection algorithm for topography data. Planetary and Space Science 60, 236-247.

Sharpton V.L 2014. Outcrops on lunar crater rims: Implications for rim construction mechanisms, ejecta volumes and excavation depths. Journal of Geophysical Research 119, 154-168.

Sharpton V.L., Krochuk R.V., and Herrick R.R. 2013. Characterization and morphological reconstruction of the Terny impact structure, central Ukraine. Meteoritics & Planetary Science 48, 806-818.

Schmidt J. and R. Andrew, 2005. Multi-scale landform characterization. Royal Geographical Society, p.37.3, 341–350

Stöffler D., Ryder G., Ivanov B.A., Artemieva N.A., Cintala M.J., and Grieve R.A.F. 2006. Cratering History and Lunar Chronology. In: Reviews in Mineralogy & Geochemistry 60, 519-596.

Tran T., Rosiek M.R., Beyer R.A., Mattson S., Howington-Kraus E., Robinson M.S., Archinal B.A., Edmundson K., Harbour D., Anderson E., and the LROC Science Team 2010. Generating digital terrain models using LROC NAC images. ASPRS/CaGIS.

Vernazza P., Binzel R.P., Rossi A., Fulchignoni M., and Birlan M., 2009. Solar wind as the origin of rapid reddening of asterioid surfaces. Nature, 458, 993-995.

Vivaldi V., A. Ninfo, M. Massironi, E. Martellato, G. Cremonese. Morphometric analysis of a fresh simple crater on the Moon. Mem. S.A.It. Vol. 87, 19., 2016.

Watters W.A., Geiger L.M., Fendrock M., and Gibson R. 2015. Morphometry of small recent impact craters on Mars: Size and terrain dependence, short-term modification. Journal of Geophysical Research Planets 120, 226-254.

Weider S.Z., Crawford I.A., and Joy K.H. 2010. Individual lava flow thicknesses in Oceanus Procellarum and Mare Serenitatis determined from Clementine multispectral data. Icarus 209, 323-336.

Wilhelms D.E., McCauley J.F., and Trask N.J. 1987. The geologic history of the Moon. USGS Report 1348, 302 p.

Wood J., 2009. Chapter 14: Geomorphometry in LandSerf. In: Hengl T and Reuter HI (eds), Geomorphometry-Concepts, Software, Applications. Developments in Soil Science, vol. 33, Elsevier, Amsterdam, 333-349.

Wood, J., 1996. The geomorphological characterization of digital elevation models. PhD Thesis, University of Leicester, UK.

Xiao Z., Zeng Z., Ding N., and Molaro J. 2013. Mass wasting features on the Moon – how active is the lunar surface? Earth and Planetary Science Letters 376, 1-11.

CHAPTER 3

COMPARISON BETWEEN SIMPLE IMPACT CRATERS MORPHOMETRY FROM DIFFERENTLY AGED LUNAR MARIA: A POTENTIAL TOOL FOR ABSOLUTE AGE ESTIMATION

Vivaldi V.[1,2], Massironi M.[2,1], Ninfo A.[3], Cremonese G.[1]

(1) INAF-Astronomical Observatory of Padua, Italy, (2) Dept. of Geosciences, University of Padua, Italy. (3) Dipartimento di Fisica e Scienze della Terra, University of Ferrara, Italy

ABSTRACT

Crater degradation can be employed to constrain the chronological evolution of a planetary surfaces. The degradation of lunar simple impact craters is influenced indeed by gravitative processes as well as space weathering, that induce a continuous and diffusive smoothing effect on crater morphology.

This research is focused on finding a correlation between the distribution of the morphometric variables of simple impact craters and the absolute model ages of the units where they were emplaced. At this purpose we have applied an objective numerical approach based on a topographic survey to evaluate and characterize the simple impact craters degradation within different lunar maria. In particular, a geomorphometric analysis was carried out using the global DTM "SLDEM2015" in order to retrieve morphometric variables, such as slope and curvatures.

We analysed over 1000 simple impact craters from several geological units to compare the distribution of crater morphology population pertaining to six differently aged lunar basins.

A power law function has been identified between inner wall mean slopes and crater diameters, for each of the six basins considered. The mean slope values have shown a relation between crater morphology and the absolute model ages of the lava units where they reside. The older is the unit the lower are the mean slopes values in function of crater diameters. Older lava units are indeed characterized by a dominance of older craters with lower mean slope values in their crater populations, whereas younger units, with higher mean slope values, show a crater populations dominated by more recent impacts. This

trend is the expression of the morphological degradation, which is strictly connected to the lunar maria age.

INTRODUCTION

Impact craters are the most widespread landforms on rocky bodies surfaces of the Solar System [Melosh, 1989]. They are one of the most important geological features that characterize the local and global morphology of planetary surfaces, being an essential element for understanding the formation and the evolution of the Solar System. Indeed the morphologic evolution of a planetary surface results from cumulative effects of subsequent impacts, volcanic emplacements, tectonics, landslides, aeolian activity, and space weathering [Neukum et al., 1975; Melosh, 1989].

Impact craters morphology results from the interaction between gravity and target strength under dynamical load. Progressively post-impact modification processes, as for instance crater degradation, might deeply affect the observed structures. Fresh craters are the best expression of the original morphology of an impact crater, and can be distinguished from their sharp profiles and the high reflectance of their ejecta [e.g. Head, 1979].

In 1970 Soderblom formulated a theoretical basis that suppose a diffusional form of degradation, confirmed by Fassett [2014]. Particularly active processes of degradation on the Moon are the gravitative ones, dominated by post impact landslides, and space weathering, due to micrometeorites bombardment and cosmic rays alteration [Neukum 1976]. Thermal expansion and contraction [Molaro and Byrne, 2012] or seismic shaking [Schultz, 1995] are other active processes involved in regolith movement on the Moon. Those processes may have a contribution to the topographic diffusion, but their importance relative to space weathering is still unknown.

Crater degradation can be used to constrain the chronological evolution of planetary surfaces as relative dating [Fassett, 2014]. On the Moon, pre-Copernican craters were subjected to heavy erosional rate due to volcanism infilling and continuous impact phenomena. By contrast post-Copernican craters are undergone to a moderate erosional rate. They can be modified indeed only by space weathering or eventually by later impacts in their proximity, which caused rim crest smoothing or collapse and floor infilling with external ejecta [Garvin et al., 1998]. Recent works attempted even absolute age determinations based on the concept that older terrains should have craters in a more advanced state of degradation than younger ones, exposed for a shorter period to erosional processes. In particular a diffusive erosional process was demonstrate to be the main cause of the crater's morphologic evolution [Fassett, 2014].

Geomorphometry allows a qualitative description of planetary morphology and can be used to quantitatively characterize crater morphologies through surface landform parameters such as the *elevation*, the *slope* and the *curvatures* [Pike, 1995, 2002; Pike et al., 2009].
Nowadays morphometric analysis on planetary surfaces is mainly conducted through topographic profiles [e.g., Aasim and Bahuguna 2014, Basilevsky et al. 2014, Fassett and Thomson 2014, Pike 1974, Salamumićcar et al. 2012, Watters et al. 2015] which might not be well representative of the real 3D surface complexity. This can be instead retrieved by a continuous areal analysis of high resolution topography (DTMs).
Here we propose an objective method to determine and quantify the degradation of simple impact craters, by applying areal geomorphometric techniques on DTMs. Morphometric analysis indeed has twofold benefits as topographic based survey and quantitative approach of investigation. In particular we have tested and applied a method of surface analysis, based on the geomorphometry of all the area covered by each impact crater.
In this research we have recognized only simple, circular and symmetric impact craters with no elliptical shape, in order to guarantee as uniform initial morphology. Moreover we have mainly investigated the crater inner walls, one of the more susceptible crater sectors to morphologic modifications by degradation processes [Vivaldi et al., 2017].

GEOLOGICAL SETTING OF THE TARGET AREAS

We have performed a wide survey on the nearside of the Moon, considering most of the main *maria*, which are characterized by different average age and excluding from the analysis surfaces dominated by obvious clusters or secondary crater chains. Lunar *maria* are smooth plains with relative young surfaces not saturated by cratering and their basaltic composition suggests a homogeneous rheology when the impacts occurred. In this context only a thin regolith layer might influence small impacts (diameters <200m).
We analysed simple crater of several geological units from six lunar basaltic basins.
Crater within units with a comparable absolute model age and pertaining to the same basin, were considered together obtaining six chronological subsets as shown in *Tab.1*. All chronological subsets areas covers a total of about 15% (about 850,000 km^2) of the *maria* in the nearside of the Moon (*Fig.1A*).

CHRONOLOGICAL SUBSET	GEOLOGICAL UNITS (Hiesinger et al., 2011)	MEAN AGE	SURFACE AREA	N° CRATERS
Procellarum	P60 (1.20Ga); P58 (1.33Ga); P55 (1.67Ga); P56 (1.49Ga); P53(1.68Ga)	1.47 Gy	200,000 km^2	164
Serenitatis	S26 (2.94 Ga); S27 (2.90 Ga); S28 (2.84 Ga)	2.89 Gy	100,000 km^2	181
Imbrium	I19 (3.10 Gy); I20 – I21 (3.01 Gy); I22 (2.96 Ga).	3.02Gy	400,000 km^2	178
Crisium	U1 (3.65±0.05 Ga); U2 (3.50±0.10 Ga)	3.57 Gy	100,000 km^2	159
Endymion	(3.63–3.70 Ga)	3.66 Gy	25,000 km^2	174
Australe	A2 (3.80 Ga); A22 (3.57Ga)	3.68 Gy	25,000 km^2	158

Table 1- Summary of lunar maria and geological units used in this research. The table include the average absolute modes ages of the units and the count of the extracted craters.

Oceanus Procellarum is a wide lunar basaltic mare located on the western edge of the Moon near side. *Procellarum* is called "*oceanus*" because it's the largest of the lunar *maria* covering over 4000000 km^2, with a diameter from the northern to the southern edge of 2500 km.

This basin was interested by a long period of volcanism, occurred from 1.3 to about 3.7 billion years. There are some basalt flows covering the bright rays of Lichtenberg crater (Eratosthenian age) and confirming the youngness of lava flows in *Procellarum* [McAlpin et al., 2008] This lava flows are probably Copernican in age and they may be a marker of the end of volcanism on the Moon [Hiesinger et al., 2000]. The central regions of the basin, considered in our analysis, are characterized by younger ages with respect to the western sector (1.47 Ga on average).

The crater size frequency distribution on *oceanus Procellarum* shows an absolute ages range from 1.2 to 3.93Ga [Hiesinger et al., 2003]. It was subdivided into 60 geological units, five of which are Copernican in age (P56, P57, P58, P59, P60) [Hiesinger et al., 2011]. We considered impact craters within the younger geological units, P60 (1.20 Gy), P58 (1.33Ga), P55 (1.67 Ga), P56 (1.49 Ga) and P53 (1.68 Ga) [Hiesinger et al., 2011].

Mare Imbrium is a wide basaltic plain on the nearside of the Moon and with its diameter of 1160 km and an area of 890000 km^2 is the second largest basin after *Oceanus Procellarum* [Spudis, 1993]. It was emplaced on one of the larger impact craters in the Solar System, probably due to the collision between the Moon and a proto-planetary body, during the Late Heavy Bombardment [Wetherill, 1975]. Later the large basin was covered by basaltic lava floods shaping the flat volcanic maria we can see today. The basin is located within different surrounding concentric rings of mountains that are the morphologic evidence of the dramatic uplift due to the impact event.

Imbrium was subdivided into 30 units defined by morphological boundaries and spectral analysis and with an absolute model age ranging from 2.01 to 3.57 Ga [Hiesinger et al., 2000]. We have chosen units with intermediate ages I19 (3.10 Gy), I20, I21 (3.01 Gy) and I22 (2.96 Gy) [Hiesinger et al., 2011].

Mare Serenitatis is located on the nearside of the Moon and it is a large multiring basin, with a diameter of 920 km and an area of about 400000 km^2. The age of *mare Serenitatis* basin is not yet clearly known. Recent works based on crater counting placed *Serenitatis* in the *Nectarian* period (3.87 Gy), at the time of the Late Heavy Bombardment (LHB), when the Moon was exposed to impacts of asteroids hundred-kilometers in size [Hiesinger 2003, Stöffler et al., 2006]. The *Serenitatis* stratigraphic sequence could reach few kilometers of depth from the *maria* surface and it is characterized by solidified lava flows, with a thickness up to around several hundred meters [Pommerol et al., 2010; Weider et al., 2010]. The thickness of lava units, which can change in function of the pre-emplacement local topography and erosional processes, is constrained by the spectral analyses of impact craters and their ejecta that can reveal possible distinct material ejected by impacts or exposed at the craters floors at different depths [Weider et al., 2010].

The *mare Serenitatis* basin was subdivided into 29 geological units differing in albedo, thickness and spectral properties and belonging to successive lava flows emplaced from 2.44 to 3.81 Ga ago [Hiesinger et al., 2011]. From the 29 units we extracted simple impact craters only from the latest ones: S26 (2.94 Gy), S27 (2.90 Gy), S28 (2.84 Gy).

Mare Crisium is located in the northeast quadrant of the lunar near side. This basin is Nectarian in age (about 3.9 Gy) and cover an area of 176,000 km^2. The measurements from LOLA altimeter revealed that the floor of *mare Crisium* is approximately 1.8 km below the lunar datum, while the outer rim is about 3.34 km above it. *Mare Crisium* regional topography appears clearly annular. Mare surface slopes and the annular nature of unit boundaries suggest that the present topographic configuration of the mare is not simply the result of continued accumulation of lavas on the *Crisium* basin floor [Adams et al, 1978]. Lava flows indeed are prominent enough in this mare to be seen in the LOLA topographic data. The Soviet mission "*Luna 24*" landed in mare *Crisium* in 1976 and returned samples from the lunar surface to Earth.

The model age measurements for *mare Crisium* basalts enlighten a wide range of ages from 2.71 to 3.65 Ga, suggesting an emplacement period spanning from Eratosthenian to Imbrian ages. In particular the sectors in proximity with the highlands boundary at the NE quadrant have 2.5 Ga whereas the ages in the central and the western regions of the basin range from 3.5 to 3.65 Ga [Hiesinger et al., 2011].

The basin was subdivided into 3 main groups (Units) being the group II (Unit II) the wider with an absolute model age of 3.5±0.1 Gy, the group I (Unit I) the older (absolute age 3.65±0.07) and the group III (Unit III)the younger one (absolute age 2.5±0.4 Gy) [Boyce & Johnson, 1977]. The Unit II age was also fixed by the radiometric ages from "*Luna 24*" mission giving 3.4 Ga [Hiesinger et al., 2011].

Endymion is a small basin located to the east of *mare Frigoris*, and north of the *lacus Temporis* close to the northeast limb of the Moon. It cover an area of about 19000 km^2 with a dimeter of about 180 km. The basin floor was interested by basalt lava floods 3.63–3.70 Ga in age [Hiesinger et al., 2011]. The infilling materials are characterized by a particularly low albedo. Given the small size of this basin we have extracted simple impact craters from entire surface.

Mare Australe is located in the southeastern hemisphere of the Moon and its central selenographic coordinates are 38.9° S, 93.0° E. This lunar mare has a diameter of 880km and interests both the near and far sides of the Moon [Spudis, 1993]. *Mare Australe* is characterized by dark volcanic basalts that was emplaced in the Upper Imbrian age, infilling the basin which was formed in Pre-Nectarian time. Hence the estimated model ages of *Australe* infillings are between 3.08 and 3.91 Ga. In the late Imbrian was formed the main part of the lava flows of *Australe*, ranging from 3.6 to 3.8 Ga [Hiesinger et al., 2000]. Within *Australe* basin we have limited our analysis to the units A2 (3.80 Gy) and A22 (3.57Gy).

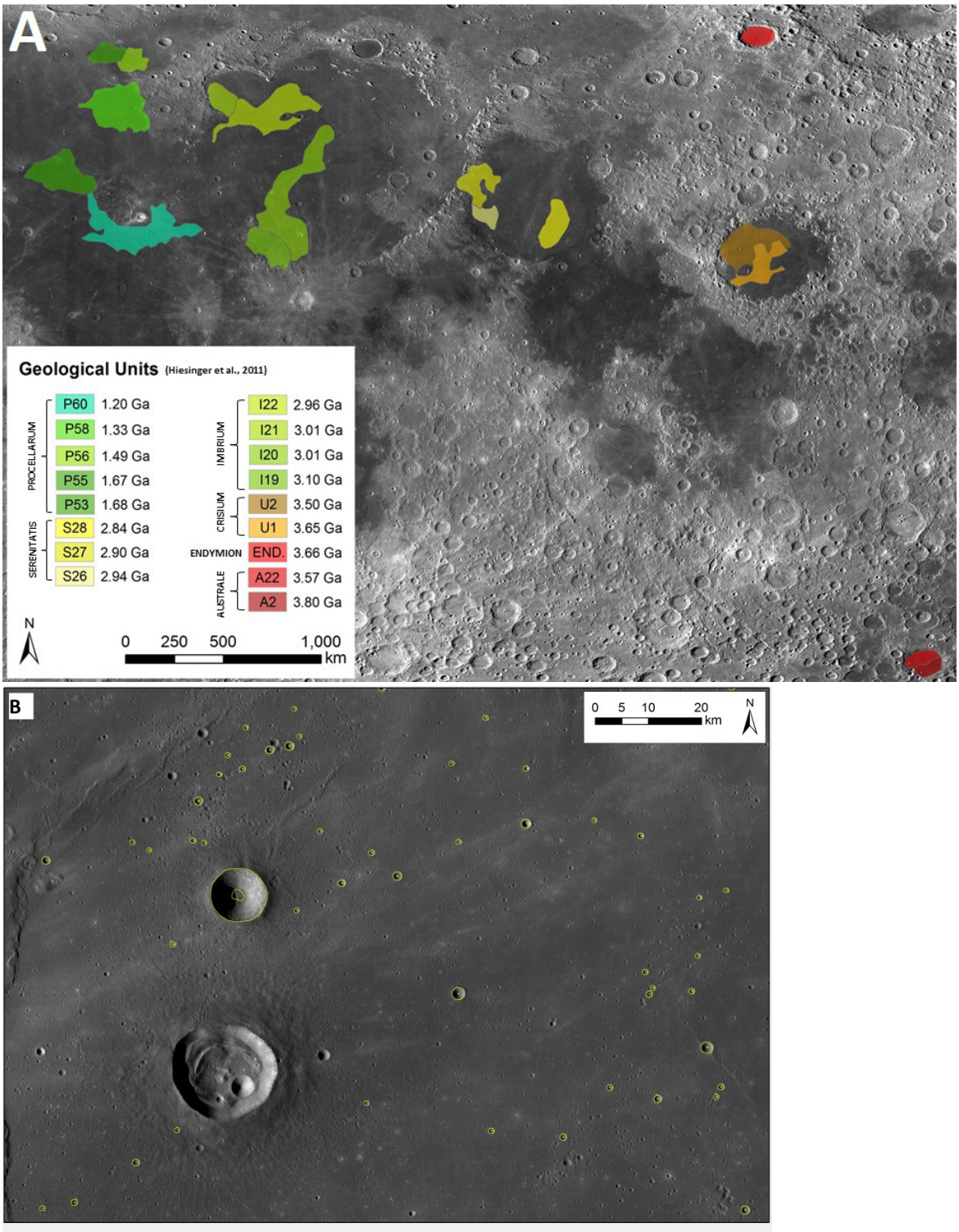

Fig.1A- *Geological units with their absolute model ages [Hiesinger et al., 2011]. The units are gathered into the six datasets considered in this research.*

Fig1B- *Particular of crater extraction masks.*

DATA AND METHODS

Our analysis was performed on the *"SLDEM2015"* product, a global DTM produced by *United States Geological Survey* (USGS) with a spatial resolution of 59m at the equator and a vertical accuracy of about 1-2 m [Baker et al., 2016].

"*SLDM2015*" was obtained by merging the data of the *Lunar Orbiter Laser Altimeter* (LOLA), onboard the *Lunar Reconnaissance Orbiter* (LRO), and the DTMs derived by the *Kaguya-Selene Terrain Camera* (TC). In particular, LOLA produced a global topographic model as well as a global geodetic framework, with a resolution of 118m/px. Moreover it covered also the permanently shadowed polar regions of the lunar surface [Beyer et al. 2015]. The optical high-performance of the *Terrain Camera* (TC), integrated in the Lunar Imager/Spectrometer (LISM) instrument suite onboard *Kaguya-Selene* mission (JAXA), produced a 7.4-meter spatial resolution global DTM [Kato, 2007].

The "*SLDEM2015*" was generated from $\sim 4.5 \times 10^9$ geodetically-accurate topographic heights from LOLA, to which were co-registered 43,200 stereo-derived DTMs (1°x1°) from the *Kaguya-Selene Terrain Camera* (TC) (~1010 pixels in total) with less than 5 m of vertical residuals with the LOLA data [Baker et Al, 2016]. The global "*SLDEM2015*" was clipped into six DTM tiles, one for each chronological unit, to reduce time processing for the calculation of the morphometric variables. From the topography of each "*SLDEM2015*" DTM tile we extracted two morphometric variables, *slope* and *profile curvature*, calculated in *ENVI*.

Since the *profile curvature* is sensitive to morphologic variations along the maximum plane of declivity, we employed this morphometric variable to automatically isolate the inner walls of the analyzed impact craters [see Vivaldi et al., submitted, for details]. At this purpose we have classified the *profile curvature* raster to detect the rim/inner wall and inner wall/floor transitions. Those transitions are characterized by a significant change of *slope* and maximum values of *profile curvature* highlighting the inner scarp perimeter and allowing the extraction of the sector. The classified rasters were successively converted into vector layers (shapefiles) which are used as extracting masks for inner walls (*Fig.1B*). In addition those shapefiles allowed to calculate area and diameter of the impact craters.

The analysis was carried out by extracting 1024 impact craters with a diameter ranging from 0.5 to 12 km. Impact craters with a diameter lower than 0.5 km have not enough pixels on the "*SLDEM2015*" mosaic to assure significant morphometric statistic: from a small crater (diameter of 0.5 km) we could extract about 80 pixels, whereas from a large crater (diameter 12 km) we could extract about 3×10^4 pixels. On the other side diameters of 12 km define the transition from simple to complex craters. Finally we have extracted all *slope* pixel values within each crater inner wall, retrieving a robust geomorphometric statistics: 1024 craters were extracted into six datasets, one of each pertaining to distinct chronological units.

The statistical analysis was performed using *Esri Arc Map*, *Past* and *Stat-Graphics*. We have performed several descriptive and comparative statistical analyses on all datasets, with the aim to find out potential morphologic evidences of datasets that differ in absolute model age.

RESULTS

Datasets statistical description

A preliminary descriptive statistics of the six datasets related to mean *slope* values of crater inner walls was carried out and shown in *Tab.2* where are reported crucial statistical parameters, such as *mean*, *Standard Deviation* (SD), *Coefficient of Variation* (CV), *Minimum and Maximum* (MIN – MAX), *Range*, *Skewness* and *Kurtosis*. Particularly interesting are the *Skewness* and the *Kurtosis* parameters, that can be used to determine if samples are close to normal distribution. In our datasets the values of five datasets over six are out of the range -2 to +2, indicating significant deviations from a normal distribution. As shown in *Tab.2*, *Skewness* and *Kurtosis* indexes enlighten indeed that dataset *Australe, Endymion, Crisium, Serenitatis* and *Procellarum* exceed the normal distribution, suggesting the presence of several outliers craters.

	AUSTRALE	ENDYMION	CRISIUM	SERENITATIS	IMBRIUM	PROCELLARUM
MEAN	12.179	12.3539	16.5903	18.6754	22.563	23.89
SD	2.27781	1.38362	3.24444	2.34444	2.07081	2.46577
CV	18.7027%	11.1999%	19.5563%	12.5536%	9.17788%	10.3213%
MIN	9.00432	10.3485	9.50141	15.3043	18.7631	20.5139
MAX	22.759	18.5111	28.401	28.6229	28.5036	32.1432
RANGE	13.7547	8.16265	18.8996	13.3187	9.74054	11.6292
SKEWNESS	8.96786	8.5535	4.52839	7.55988	1.95987	4.16107
KURTOSIS	11.3365	10.9903	2.84107	8.10599	-0.866503	0.177323

Table 2 – *Summary of statistical parameter: mean, Standard Deviation (SD), Coefficient of Variation (CV), Minimum and Maximum (MIN – MAX), Range, Skewness and Kurtosis. The underlined Skewness and Kurtosis values are exceeding the normal distribution.*

Tab.3 summarizes the datasets average absolute age, the number of extracted craters, the *minimum-maximum* mean *slope* value and the *Standard Error of the Mean* (SEM). In particular the SEM was useful to evaluate the precision in the crater mean *slope* estimation, taking into account both the value of the *Standard Deviation* (SD) and the crater population count. SEM index decreases with the number of craters in each population. In other words the SEM helped us to estimate the variability between samples, since the SD describes only

the deviation of each sample from the normal distribution. From the SEM values evaluation we can observe that the estimation of crater mean *slope* was homogeneously calculated, being the number of craters comparable for all datasets. SEM varies indeed only from 0.19° to 0.20° for all datasets, hence the mean value of the population is in a confidence interval of 95%.

DATASET	ABSOLUTE AGE	CRATER COUNT	MIN MEAN SLOPE	MAX MEAN SLOPE	SEM
PROCELLARUM	1.47 Gy	164	20.5	31.80	0.20
SERENITATIS	2.89 Gy	181	18.76	30.40	0.19
IMBRIUM	3.02Gy	178	15.30	29.45	0.19
CRISIUM	3.57 Gy	159	9.50	28.55	0.20
ENDYMION	3.66 Gy	174	10.35	19.60	0.19
AUSTRALE	3.68 Gy	168	9.00	22.8	0.20

Table 3 - *Summary of the datasets, related to their average absolute age, the number of extracted craters, the minimum-maximum mean slope value and the SEM.*

Afterwards we have applied the *Kolmogorov-Smirnov Normality Test* for each dataset to confirm the non-normal distribution of those datasets, previously identified by *Skewness* and *Kurtosis* indexes (*Tab.2*). This test verify the normality or non-normality of the shape of the sample distribution. If the p-value is <0.05 the distribution is non-normal while if it is >0.05 the distribution is normal (*Fig.2,3*). In our datasets the normal distribution was proven only for the Serenitatis dataset (*p-value* >0.05); the other datasets are non-normal, with a confidence level of 95% (*Tab.4*).

DATASET	P-VALUE
PROCELLARUM	0.0190
IMBRIUM	0.0026
SERENITATIS	0.4481
CRISIUM	0.0210
ENDYMION	0.0008
AUSTRALE	0.0068

Table 4 - *Kolmogorov-Smirnov Normality test with p-values for each dataset.*

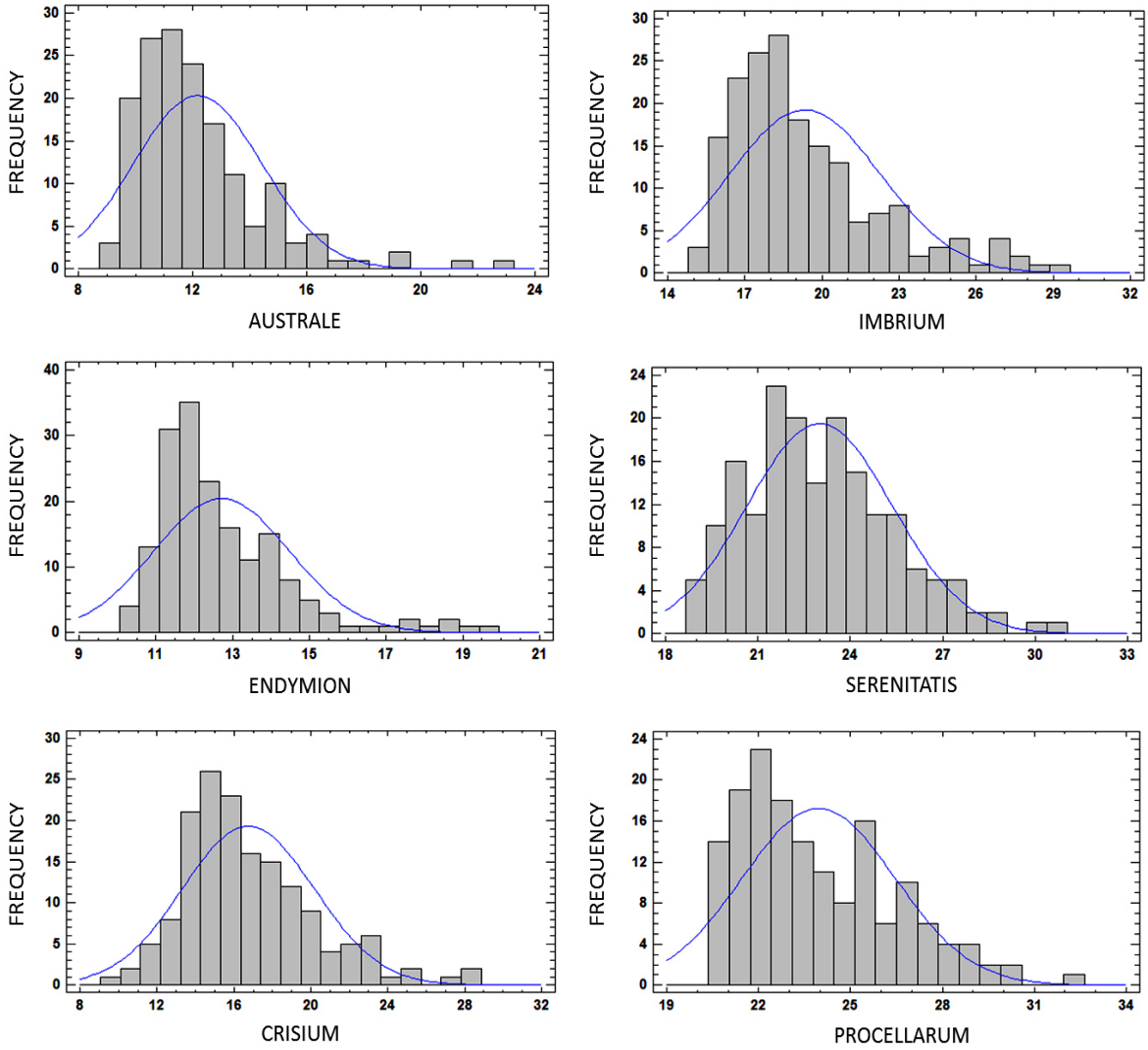

Fig.2 – *Frequency histograms of the six datasets. The blue lines are the estimated normal distributions of datasets. Serenitatis is the only dataset normal distributed. On x axes are plotted the craters mean slope values.*

Datasets statistical comparison

In this section provide different statistical tests and diagrams, in order to compare our datasets and understand if there are significant statistical variations among them. The importance of finding a significant statistical variations is related to the correlation between

the geomorphometry of simple impact craters and the absolute model ages of the surfaces where they are superposed.
Given that the samples of all datasets are non-normal distributed, a non-parametric test is more advisable [Field, 2000]. At this purpose we have performed the non-parametric *one-way Kruskal-Wallis* test, comparing the medians instead of averages, as shown in *Tab.5*. The *p-value* of this test is <0.05 and it confirms there is a significant variation among the datasets, in a confidence level of 95%.

SURFACE DATASET	SAMPLE SIZE	AV. RANK	TEST RESULTS
PROCELLARUM	158	828.633	
SERENITATIS	181	578.619	*Statistical Test* = 770.004
IMBRIUM	178	784.410	
CRISIUM	159	442.805	*P-value* = 0
ENDYMION	174	208.489	
AUSTRALE	158	168.190	

Table 5 - *Kruskal-Wallis test. The table reports the number of craters extracted, the average Rank and the test result with the p-value.*

Since the *Kruskal-Wallis* test enlightens a statistically significant variance among the six datasets we performed the Multiple Range Test (MRT) in order to quantify the differences among diverse combinations of datasets. As shown in *Tab.6* the MRT confirmed that there are significant differences (S.D.) in all datasets matchings where surfaces of different model age occur. The only exception is the Australe-Endymion combination, that have not a significant statistical variation (difference=0.53492) as expected, given their similar average absolute age models (3.66-3.68 Ga).

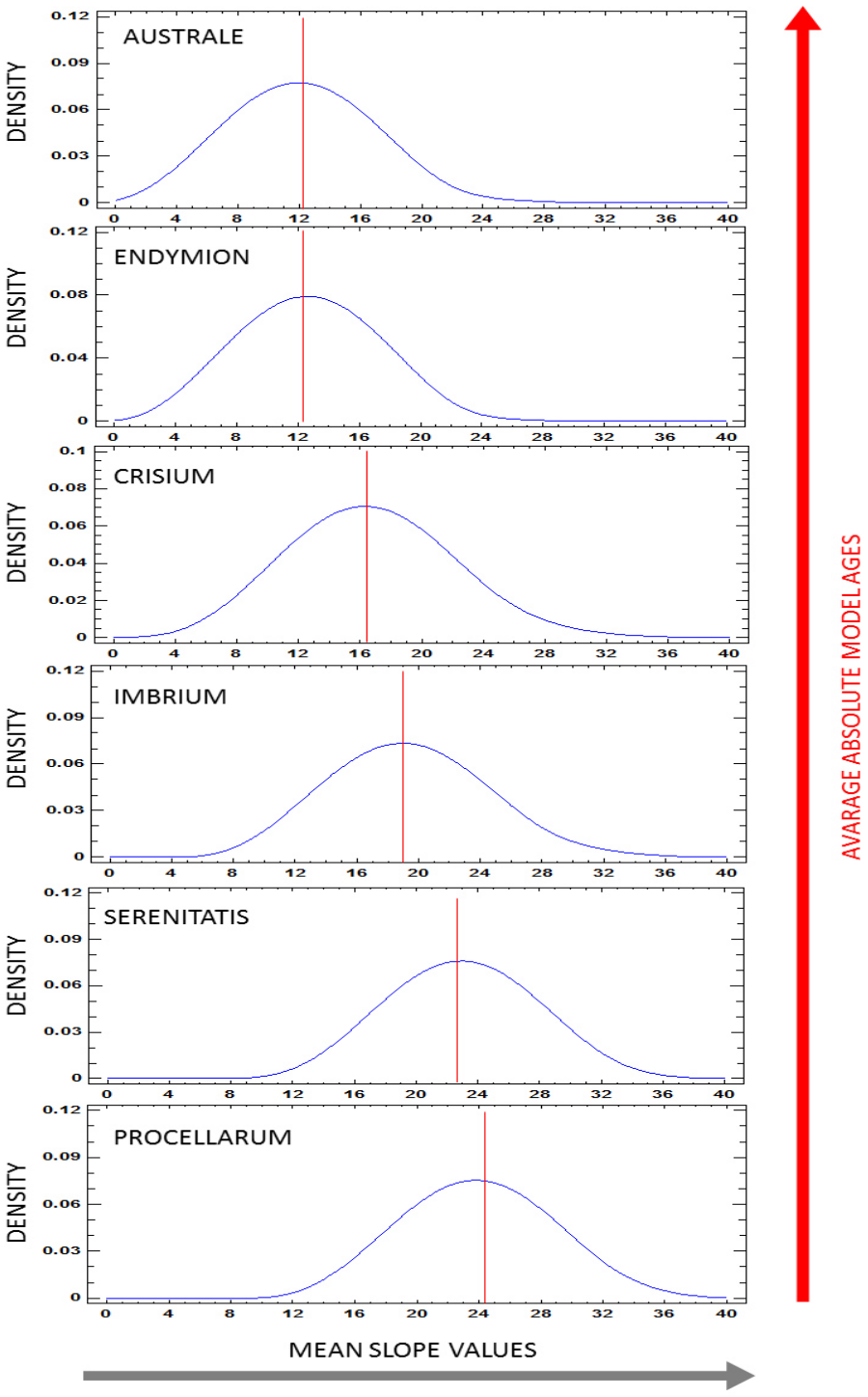

Fig.3 – *Density distribution of the six datasets. The red lines mark the peak of the sample distributions density for each datasets. The peaks shift from lower to higher men slope values from the older to the younger surfaces.*

DATASET COMPARISON	S.D.	DIFFERENCE	+/-
AUSTRALE - ENDYMION	NO	-0.53492	0.558702
AUSTRALE - CRISIUM	YES	-4.56965	0.571106
AUSTRALE - SERENITATIS	YES	-7.15546	0.553537
AUSTRALE - IMBRIUM	YES	-10.8268	0.555707
AUSTRALE - PROCELLARUM	YES	-11.7785	0.572006
ENDYMION - CRISIUM	YES	-4.03473	0.557781
ENDYMION - SERENITATIS	YES	-6.62054	0.539777
ENDYMION - IMBRIUM	YES	-10.2918	0.542002
ENDYMION - PROCELLARUM	YES	-11.2436	0.558702
CRISIUM - SERENITATIS	YES	-2.58581	0.552607
CRISIUM - IMBRIUM	YES	-6.25711	0.554780
CRISIUM - PROCELLARUM	YES	-7.20883	0.571106
SERENITATIS - IMBRIUM	YES	-3.67130	0.536676
SERENITATIS - PROCELLARUM	YES	-4.62302	0.553537
IMBRIUM - PROCELLARUM	YES	-0.95171	0.555707

Table 6 – *Multiple Range Test. The table reports the combinations of datasets, the Significant Difference (S.D.), the Difference values and the approximation limits.*

The analysis of variance *one-way ANOVA* is a parametric test and it would be not suggested for non-normal population analysis [Fisher, 1942; Snedecor & Cochran, 1967]. However we have also tried to check the statistical difference among the datasets by performing the parametric *one-way ANOVA* test, bisecting the data variance into two components: a component between datasets and an intra-dataset component. In the *ANOVA* table (*Tab.7*) the *p-value* is less than 0.05 confirming that there is a significant statistical difference among the averages of the six datasets, with a confidence level of 95.0%.

ANOVA TEST	SS	DF	MS	F	P-VALUE
AMONG DATASETS	20853.7	5	4170.73	619.84	0.0000
WITHIN EACH DATASET	6742.15	1002	6.7287		
TOTAL	27595.8	1007			

Table 7 – *ANOVA table parameters: the table summarize the Sum of Squares (SS), the Degrees of Freedom (DF), the Mean Sum of Squares due to the source (MF), the F-statistic and the P-value.*

After we ensured that datasets were characterized by significant statistical differences among them, related only to morphological variations, we were able to hypothesize that the morphometry of the dominant population of craters superposed on a specific surface could be dependent on the surface age. We have therefore plotted in a box-plot diagram the frequency of the mean *slope* values from all six datasets (*Fig.4*). The main result clearly shows how the mean *slope* decreases with the increase of absolute model ages of the units. This means that the main crater population of the older surfaces is dominated by impact craters with lower values of inner wall mean slope, suggesting the massive presence of craters in advanced status of degradation. On the other hand younger surfaces, such as Procellarum (1.47 Ga), Serenitatis (2.89 Ga) and Imbrium (3.02 Ga) are characterized by a dominance of craters with higher inner wall declivity, that is due to their more pristine morphologies.

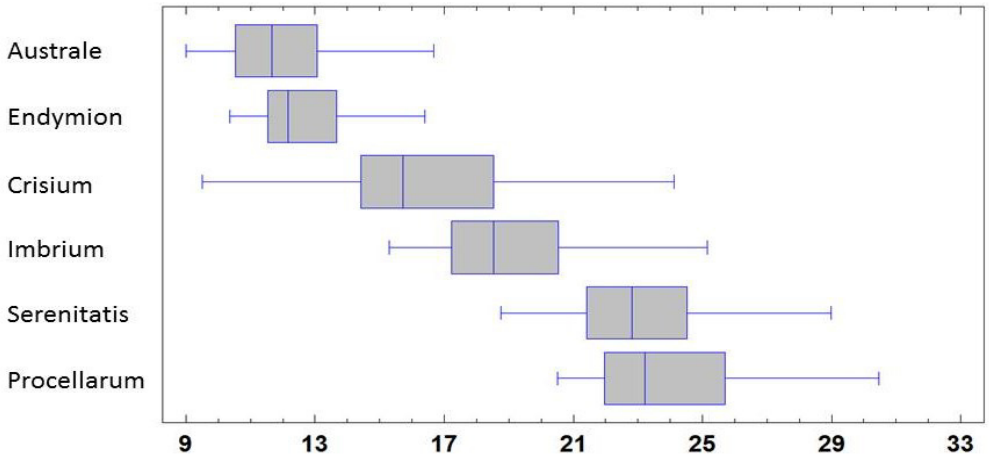

Fig.4 – *Box-plot diagrams of the frequency related to mean slope values of the six datasets. The boxes represent the 95% of craters populations. The blue lines are the medians and the error bars are related to the outliers craters.*

Relationships between inner scarp mean slopes and crater diameters

The previous results allowed us to plot the mean *slope* values against the craters diameters (Fig.5). The regression analysis of craters inner wall mean *slope* in function of craters diameters displayed a similar trend for each dataset of values. In particular all those trends show how the average inner wall declivity tends to increase from smaller to larger diameters in all the analysed surfaces. Moreover large craters have a more scattered distribution on the older terrains. Australe and Endymion datasets indeed shown (3.68 Ga

and 3.66 Ga) a population of large craters that range from C4 to C1 degradation classes, whereas in the younger surfaces large craters appear mainly fresh (C1-C2).

The distribution of the datasets clearly displays a decrease of mean *slope* values from younger to the older terrains, confirming the correlation with the absolute model age of the surface. Hence the comparison among the six datasets from different lunar *maria* shows a clear discrimination of their absolute ages.

Afterwards we found out the best trend line fitting the datasets samples distributions. The six datasets follow trend lines that fit the 40-50% of the samples, with R^2 ranging from 42% to 55%.

The related trend lines four parallel one each other out of six, are representative of the average age of the specific units dataset and can be potentially used as isochrones.

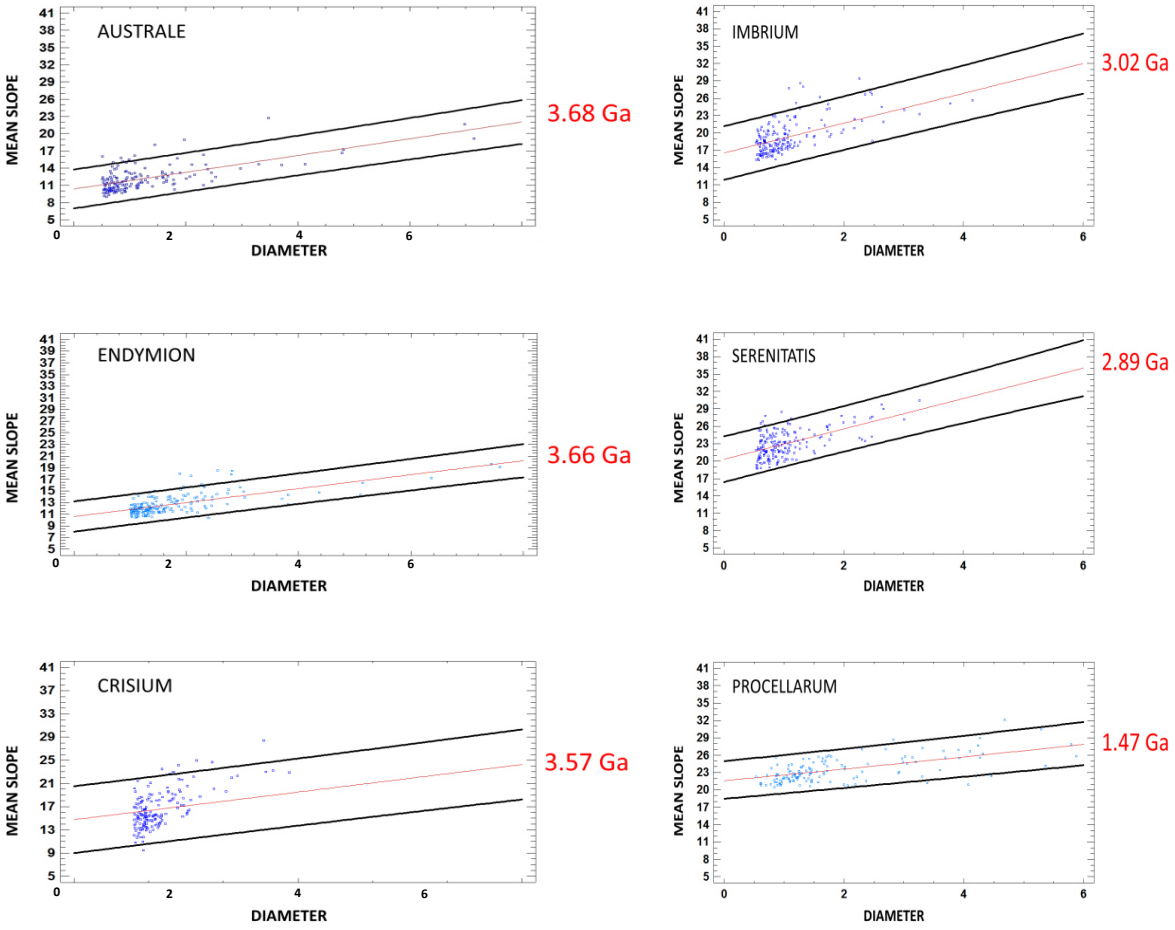

Fig.5 – *Regression analysis of mean slope values from crater inner wall in function of craters diameter The power-law trend of the six datasets allow to fix potential isochrones based on the morphologic variations of craters inner walls. Black lines mark the interval related to the 95% of craters population.*

DISCUSSIONS

The results obtained from the statistical analysis highlighted a correlation between the morphologic distribution of simple impact craters and the absolute ages of the surface where they reside. Since we have considered only homogeneous basaltic surfaces we have isolated the crater degradation as the only one variable determining crater morphologies. From the non-parametric *one-way Kruskal-Wallis* and the parametric *ANOVA* tests, the resulting *p-values* of <0.05 (*Tab.5*) have highlighted that the six datasets pertaining to different basins and ages show significant variations among them, confirming the different morphological distribution of their simple crater populations. This observation allows us to suppose a correlation between the absolute model age of a surface and the statistical distribution of the values of inner wall mean *slope* of their simple craters. Indeed the morphological modifications involving craters inner walls mainly depends on the erosional processes that smooth and infill the craters.

On the Australe, Endymion, Crisium, Imbrium and Procellarum surfaces the crater population has a scattered distribution of mean *slope* values, suggesting broad ranges of crater degradation states, as confirmed by the *Skewness* and *Kurtosis* indexes (*Tab.2*) and the *Kolmogorov-Smirnov Normality Test*. This is more evident for the ancient lunar terrains such as Australe and Endymion that have collected craters over more than 3.5 Ga. The infilling of those two basins present the largest deviation from the normal distribution of mean *slopes* and are covered by craters with a wider range of degradation states, from C4 to C1. Differently, more recent surfaces are characterized by a lower relative amount of highly degraded craters (C4) and by a smaller deviation from normal distribution of inner mean *slopes*.

The mean *slope* box-plot enlightens the distribution of the crater population of each surface; it clearly shows how the mean *slope* on the inner wall decreases with the increase of absolute model ages (*Fig.3*). Indeed, observing the frequency of the mean *slope* values (*Fig.2,3*), is clearly visible that the distributions of the inner wall mean *slopes* shift towards lower values from younger surfaces to older ones. This means that the main crater population of the more ancient surfaces, such as Endymion (3.66 Ga) and Australe (3.68 Ga), is dominated by impact craters with lower values of inner wall mean slope, suggesting the massive presence of old craters in advanced status of degradation (C3-C4). On the other hand younger surfaces, such as Procellarum (1.47 Ga), Serenitatis (2.89 Ga) and Imbrium (3.02 Ga) are dominated by craters with higher inner wall declivity, typical of fresh craters (C1-C2).

The following step is to understand how these morphological variations are distributed in function of crater diameter and ages. We compared the four degradation classes taking into account that the degradation rate a non-linear function of crater size and age and considering the uncertainty in modelling its evolution. The quantification of the inner wall

morphologic modifications among craters within the same degradation class enlighten a power law trend in function of diameter [Vivaldi et Al, 2017]. Similarly the regression analysis of the six datasets shows a trend line of the mean *slope* values in function of craters diameters. As shown in *Fig.5* larger craters present a limited range of mean *slope* values (~10°) whereas smaller ones shown a broad range of slope values (>30°). This can be due to two different effects: the mechanics of impacts and the velocity of erosion. Indeed we can hypothesize that small impacts involve mainly the regolith layers and the underlying highly fractured basalts, generating impact craters with blender morphologies. Those craters may be affected by instantaneous gravitative phenomena smoothing inner scarps of the freshly formed craters. In addition smaller craters are more susceptible to a quick erosion than the larger ones [Fassett & Thomson, 2014]. The average lunar diffusivity is indeed ~5.5m^2/Ga in the past 3Ga; in this time range and a 1km diameter craters may degrade approximately up to 52% of their initial depth, 300m diameter craters up to 7%, and craters smaller than 200–300m are totally degraded [Fassett & Thomson, 2014].

The distribution of the datasets show a clear decreasing of the average declivity shifting from the younger to the older terrains, confirming that the dominant crater population of the more ancient datasets is mainly composed by eroded craters (C3-C4) in coherence with the absolute age of the surface. Large craters present also a more scattered distribution in older surfaces being present C4 to C1 craters all together. This is because ancient surfaces had enough time to erode large craters from C1 to C4, whereas in the younger surfaces large craters are less eroded (C1-C2) [see Vivaldi et al., 2017].

Finally the six regression analysis trends derived from the datasets regression analysis suggest a relation between the trend lines of crater distribution and potential isochrones. The trend lines indeed are expression of about the 50% of the population from each dataset of craters and depend on the absolute model age of the surface where craters reside.

CONCLUSIONS

In this research we have applied morphometric analysis on a global topographic DTM (*SLDEM2015*) in order to find out a correlation between the degradation of simple impact craters and the absolute model age of the surfaces where they are superposed.

The analysis allowed us to better interpret the statistical distribution and compare the crater morphometry of differently aged surfaces.

In particular, we extracted the mean *slope* values from the inner walls of 1024 impact craters, on six differently aged surfaces. The statistical distribution of the mean *slope* has shown that older surfaces are characterized by a lower mean *slope* values in function of crater diameters with respect to the younger surfaces. This suggests a dominance of more

eroded craters (C3-C4) within old units. By contrast younger surfaces are dominated by more recent impacts (C1-C2), with higher mean slopes of their walls. Hence the statistical analysis of crater geomorphometry allowed us to fix absolute age thresholds following the morphologic trends of simple craters from differently aged lunar maria in function of diameters [Vivaldi et al., 2017, submitted].

The morphometric approach described in this research, supported by a robust statistical analysis, can be potentially useful for the age refinement of lunar geological units as well as of other planetary surfaces (e.g. Mercury, small bodies).

AKNOWLEDGEMENTS

This research was supported by the *Italian Space Agency* (ASI) within the SIMBIO-SYS Project (ASI-INAF agreement no. I/022/10/0).

REFERENCES

Aasim M. and I.M. Bahuguna, 2014. Depth-diameter ratios of lunar craters from chandrayaan-1 TMC images and DEM and its significance. International Journal Of Geomatics And Geosciences Volume 4, No4; ISSN 0976 – 4380.

Adams J.B., Head J.W., McCord T.B., Pieters C., Zisk S., 1978. Mare Crisium: Regional Stratigraphy And Geologic History. Geophysical Research Letter , VOL. 5, NO. 4.

Albani, M. , Klinkenberg, B. , Andison, D.W. and Kimmins, J.P., 2004: The choice of window size in approximating topographic surfaces from digital elevation models . International Journal of Geographic Information Science 18, 577—93.

Arrell K.E., Fisher PF, Tate NJ and Bastin L, 2007, A fuzzy c-means classification of elevation derivatives to extract the morphometric classification of landforms in Snowdonia, Wales. Computers & Geosciences, 33:1366-1381.

Arthur, D.W.G., Agnieray, A.P., Horvath, R.A., Wood, C.A. , Chapman, C.R., 1963. The system of lunar craters. Quadrant I. Comm. Lunar Planet. Lab. 2, #30.

Baker M.K., Mazarico E., Neumann G.A., Zuber M.T., Haruyama J., and Smith D.E., 2016. A new lunar digital elevation model from the Lunar Orbiter Laser Altimeter and SELENE Terrain Camera. Icarus 273, 346-355.

Basilevsky A.T., Kreslavsky M.A., Karachevtseva I.P, and Gusakova E.N. 2014. Morphometry of small impact craters in the Lunokhod-1 and Lunokhod-2 study areas. Planetary and Space Science 92, 77-87.

Beyer R.A., 2015. An introduction to the data and tools of planetary geomorphology. Geomorphology 240, 137-145. Chappelow J.E. 2013. Simple impact crater shape determination from shadows. Meteoritics & Planetary Science 48, 1863-1872.

Boyce J. M., and D. A. Johnson, 1978. Ages of flow units in the far eastern maria and implications for basin-filling history. Proc. Lunar Planet. Sci Conf.9th, 3275 – 3283.

Craddock R.A. and Howard A.D., 2000. Simulated degradation of lunar impact craters and a new method for age dating farside mare deposits. Journal of Geophysical Research 105, 20,387-20,401Cremonese G., Borin P., Lucchetti A., Marzari F., and Bruno M., 2013. Micrometeoroids flux on the Moon. Astronomy & Astrophysics - 551, A27.

Drăguţ L, Schauppenlehner T, Muhar A, Strobl J and Blaschke T, 2009, Optimization of scale and parametrization for terrain segmentation: an application to soil-landscape modeling. Computers & Geosciences, doi:10.1016/j.cageo.2008.10.008

Evans I.S., Hengl T. and Gorsevski P., 2009. Chapter 22 Applications in Geomorphology. In: Hengl T and Reuter HI (eds), Geomorphometry-Concepts, Software, Applications. Developments in Soil Science, vol. 33, Elsevier, Amsterdam, 497-525.

Evans I.S. 1998. What do terrain statistics really mean? In: S.N. Lane, K.S. Richards, J.H. Chandler (eds), Landform monitoring, modelling and analysis, Wiley Publications, 119-138.

Evans IS, 2003, Scale-Specific Landforms and Aspects of the Land Surface. In: Evans IS, Dikau R,

Field A., 2000. Discovering Statistics Using SPSS for Windows: Advanced Techniques for Beginners. Sage Publications, Inc. Thousand Oaks, CA, USA ©2000-ISBN:0761957553.

Fassett C.I. and Thomson B.J. 2014. Crater degradation on the lunar maria: Topographic diffusion and the rate of erosion on the moon. Journal of Geophysical Research: Planets 119, 2255-2271.

Fassett C.I., Head J.W., Kadish S.J., Mazarico E., Neumann G.A., Smith D.E., and Zuber M.T. 2012. Lunar impact basins: Stratigraphy, sequence and ages from superposed impact crater populations measured from Lunar Laser Altimeter (LOLA) data. Journal of Geophysical Research 117, E00H06.

Fisher, R.A., 1942. The Design of Experiments. Third Edition, Edinburgh: Oliver & Boyd.

Florinsky I.V. and Kuryakova G.A., 2000, Determination of grid size for digital terrain modelling in landscape investigations - exemplified by soil moisture distribution scale. International Journal of Geographical Information Science, 14:815-832

Garvin J.B. and Frawley J.J. 1998. Geometric properties of Martian impact craters: Preliminary results from the Mars Orbiter Laser Altimeter. Geophysical Research Letters 25, 4405-4408.

Garvin J.B., Robinson M.S., Frawley J., Tran T., Mazarico E., and Neumann G. 2011. Linné: simple lunar mare crater geometry from LRO observations. 42nd Lunar and Planetary Science Conference (2011), #2063.

Haruyama, J. et al. and the LISM Working Group, 2008. Earth Planets Space, 60, 243- 255.
Hartmann W.K. and Wood C.A., 1971. Moon: origin and evolution of multi-ring basins. The Moon 3, 3-78.
Head J.W., 1979. Serenitatis multi-ringed basin: regional geology and basin ring interpretation. The Moon and the Planets 21, 439-462.
Hengl T., 2006, Finding the right pixel size. Computers & Geosciences, 32:1283–1298.
Hiesinger H., J.W.Head, U. Wolf, R. Jaumann and G. Neukum, 2011. Ages and stratigraphy of lunar mare basalts: A synthesis. Geological Society of America Special Papers 2011;477;1-51 doi: 10.1130/2011.2477(01).
Hiesinger H. and Head J.W. 2006. New views of Lunar geoscience: an introduction and overview. In: Reviews in Mineralogy & Geochemistry 60, 1.81.
Hiesinger H., J. W. Head III, U. Wolf, R. Jaumann, and G. Neukum, 2003. Ages and stratigraphy of mare basalts in Oceanus Procellarum, Mare Nubium, Mare Cognitum, and Mare Insularum, J. Geophys. Res., 108, 5065, doi:10.1029/2002JE001985, E7.
Hiesinger H., Head J.W., and Wolf U. 2001. Lunar mare basalts: Mineralogical variations with time. 32nd Lunar and Planetary Science Conference (2001), #1826.
Hiesinger H., Jaumann R., Neukum G., and Head J.W. 2000. Ages of mare basalts on the lunar nearside. Journal of Geophysical Research 105, 29,239-29,275.
Kato, M., Y. Takizawa, and S. Sasaki ,2007. LPS XXXVIII, Abstract #1402.
Mahanti P., Robinson M.S., Humm D.C., and Stopar J.D. 2014. A standardized approach for quantitative characterization of impact crater topography. Icarus 241, 114-129.
MacMillan RA and Shary PA, 2009, Chapter 9 Landforms and landform elements in geomorphometry. In: Hengl T and Reuter HI (eds), Geomorphometry-Concepts, Software, Applications. Developments in Soil Science, vol. 33, Elsevier, Amsterdam, 227-254.
Martellato E., V. Vivaldi, G. Cremonese, M. Massironi, A. Ninfo, F. Marzari, J. Haruyama. Is Linné morphology influenced by the lunar stratigraphy? Insights from numerical modeling. Submitted to Meteoritics & Planetary Science, ISSN: 1945-5100 - Under review 2016.
McAlpin D.B., J.I. Nuñez, A.R. Griffin, S.B. Porter, M.S. Robinson, 2008. The case for a lunar sample return mission: Lichtenberg crater. Lunar and Planetary Science XXXIX-1443.
Melosh H.J. 2011. Planetary surface processes. Cambridge University Press, 500 p, NASA.
Melosh H.J. and Ivanov B.A. 1999. Impact crater collapse. Annual Review of Earth and Planetary Sciences 27, 385-415.
Melosh H.J. 1989. Impact cratering: A geologic process. New York: Oxford University Press. 245 p.
Melosh, H.J. and Gaffney, E.S. 1983. Acoustic fluidization and the scale dependence of impact crater morphology. J. Geophys. Res. 88, Suppl., A830-A834.

Neukum G., König B., and Arkani–Hamed J. 1975. A study of lunar impact crater size–distributions. The Moon 12, 201-229.

Neukum G. and Horn P. 1976. Effects of lava flows on lunar crater populations. The Moon 15, 205-222.

Nickerson, R.D.,G.D. Bart,M.T. Lawder,H.J. Melosh, 2011. Global lunar regolith depths revealed. 42nd Lunar and Planetary Science Conference, #2607.

Pike R.J., I.S. Evans and T. Hengl, 2009. Geomorphometry: A Brief Guide. Developments in Soil Science, Volume 33,Elsevier B.V.

Pike R.J., 2002. A bibliography of terrain modeling (geomorphometry), the quantitative representation of topography — supplement 4.0. Open-File Report 02-465. U.S. Geological Survey, Denver, 116 pp. http://geopubs.wr.usgs.gov.

Pike R.J., 1995. Geomorphometry – progress, practice and pros-pect. Zeitschrift für Geomorphologie, N.F., SupplementBand 101 221–38

Pike R.J. 1974. Depth/diameter relations of fresh lunar craters – Revision from spacecraft data. Geophysical Research Letters 1, 291-294.

Pommerol A., Kofman W., Audouard J., Grima C., Beck P., Mouginot J., Herique A., Kumamoto A., Kobayashi T., and Ono T. 2010. Detectability of subsurface interfaces in lunar maria by the LRS/SELENE sounding radar: Influence of mineralogical composition. Geophysical Research Letters 37, L03201.

Robinson M.S., Brylow S.M., Tschimmel M., Humm D., Lawrence S.J., Thomas P.C., Denevi B.W., Bowman-Cisneros E., Zerr J., Ravine M.A., Caplinger M.A., Ghaemi F.T., Schaffner J.A., Malin M.C., Mahanti P., Bartels A., Anderson J., Tran T.N., Eliason E.M., McEwen A.S., Turtle E., Jolliff B.L., and Hiesinger H. 2010. Lunar Reconnaissance Orbiter Camera (LROC) Instrument Overview. Space Science Reviews 150, 81-124.

Salamunićcar G., Lončarić S., and Mazarico E., 2012. LU60645GT and MA132843GT catalogues of Lunar and Martian impact craters developed using a Crater Shape-based interpolation crater detection algorithm for topography data. Planetary and Space Science 60, 236-247.

Sharpton V.L 2014. Outcrops on lunar crater rims: Implications for rim construction mechanisms, ejecta volumes and excavation depths. Journal of Geophysical Research 119, 154-168.

Sharpton V.L., Krochuk R.V., and Herrick R.R. 2013. Characterization and morphological reconstruction of the Terny impact structure, central Ukraine. Meteoritics & Planetary Science 48, 806-818.

Schmidt J. and R. Andrew, 2005. Multi-scale landform characterization. Royal Geographical Society, p.37.3, 341–350.

Schultz R.A., 1995. Limits on Strength and Deformation Properties of Jointed Basaltic Rock Masses. Rock Mechanics and Rock Engineering 28, 1-15.

Snedecor, G.W., and W.G. Cochran., 1967. Statistical Methods. Sixth Edition, Ames: Iowa State University Press.

Soderblom L.A., 1970. The distribution and ages of regional lithologies in the lunar maria. Ph.D. thesis, California Institute of Technology, Pasadena.

Spudis P.D., Wilhelms D.E., and Robinson M.S., 2011. The Sculptured Hills of the Taurus Highlands: Implications for the relative age of Serenitatis, basin chronologies and the cratering history of the Moon. Journal of Geophysical Research 116, E00H03.

Spudis P. D., 1993. The Geology of Multi-ring Impact Basins, Cambridge Planet.Sci. Ser., vol. 8, 263 pp., Cambridge Univ. Press, New York.

Stöffler D., Ryder G., Ivanov B.A., Artemieva N.A., Cintala M.J., and Grieve R.A.F. 2006. Cratering History and Lunar Chronology. In: Reviews in Mineralogy & Geochemistry 60, 519-596.

Tokunaga E, Ohmori H and Hirano M (eds), Concepts and Modelling in Geomorphology: International Perspectives. Terrapub, Tokyo, 61-84.

Vivaldi V., A. Ninfo, M. Massironi, E. Martellato, G. Cremonese. Morphometric analysis of a fresh simple crater on the Moon. Mem. S.A.It. Vol. 87, 19., 2016.

Vivaldi V., M. Massironi, A. Ninfo, G. Cremonese, 2017 (submitted). AGU Geophysical Monograph on "3D digital geological models: from terrestrial outcrops to planetary surfaces".

Watters W.A., Geiger L.M., Fendrock M., and Gibson R. 2015. Morphometry of small recent impact craters on Mars: Size and terrain dependence, short-term modification. Journal of Geophysical Research Planets 120, 226-254.

Weider S.Z., Crawford I.A., and Joy K.H. 2010. Individual lava flow thicknesses in Oceanus Procellarum and Mare Serenitatis determined from Clementine multispectral data. Icarus 209, 323-336.

Wetherill, G.W., 1975. Late heavy bombardment of the Moon and terrestrial planets. Lunar Science Conference, 6th, vol.2 (A78-46668 21-91), p. 1539-1561.

Wilhelms D.E., McCauley J.F., and Trask N.J. 1987. The geologic history of the Moon. USGS Report 1348, 302 p.

Wood, J., 1996. The geomorphological characterization of digital elevation models. PhD Thesis, University of Leicester, UK.

Wood J., 2009. Chapter 14 Geomorphometry in LandSerf. In: Hengl T and Reuter HI (eds), Geomorphometry-Concepts, Software, Applications. Developments in Soil Science, vol. 33, Elsevier, Amsterdam, 333-349.

Xiao Z., Zeng Z., Ding N., and Molaro J. 2013. Mass wasting features on the Moon – how active is the lunar surface? Earth and Planetary Science Letters 376, 1-11.

CONCLUSIONS

In planetary sciences age estimation of different surfaces is mainly performed by means of crater counting. Here we have attempted to find a possible correlation between crater degradation and absolute model age of geological units where craters are superposed. This purpose was carried out by applying morphometric analysis on simple impact craters.

The research can be summarized in three points: i) a topographic investigation on very high resolution data (LROC-NAC, with a cell size of 2m/pixel) to fix the typical morphometry of differently degraded craters, ii) a topographic analysis on medium resolution data (Kaguya TC DTM mosaic, with a cell size of 7.4m/pixel) to quantitatively compare the different degradation classes and iii) topographic survey on global data at low resolution (SLDEM2015, with a cell size of 59m/pixel) to correlate the statistical distribution of inner walls mean slopes of simple crater population to the absolute age of the surfaces where craters are superposed.

The first research step was to constrain the morphometric signature of a suitable example of a fresh simple impact crater, representative of the C1 degradation class. For this reason, we carried out a morphometric analysis on the Linné crater, which can be considered one of the best preserved simple impact crater on lunar maria. From the high resolution Linné DTM we calculated the main morphometric variables, such as slope, profile curvature, planar curvature and topographic openness that allowed us to characterize the morphology of the outer and inner scarps, the rim and the crater floor. In addition, from the detailed analysis of the Linné cavity, we found three uphill scarps running along the crater inner wall. Those features may be the morphological expression of subsequent emplacements of thin lava flows within mare Serenitatis and can be potentially useful to infer the stratigraphy at the impact site.

The quantification of the Linné inner wall was fundamental for the subsequent morphologic characterization of craters pertaining to the other three classes of increasing degradation (C2, C3, and C4). In particular we applied the morphometric analysis to several simple craters within the same geological unit in mare Serenitatis, finding a common power-law trend of inner slope degradation, going from larger to smaller craters, within each of the first three classes. We have also found a diameter upper cut-off at about 1 km of the most degraded crater class (C4). This can be explained by the relative young age of the considered unit in mare Serenitatis, for which there were not enough, time to degrade craters larger than 1 km up to C4. Indeed the upper diameter cut-off is present on all the degradation classes and increases from C4 to C3. These cut-offs will potentially allow a refinement of the relative age discrimination among different geological units.

The shape evolution of simple impact craters was also highlighted by the distribution of negative profile curvature (concavity) among different craters. In particular, the mean concavity decreases with increasing diameters and with the raising of degradation status. In other words, larger and more degraded craters are characterized by lower concavities and might eventually reach positive profile curvatures (convex shape). In particular larger craters have steep inner walls and flat floors, since they approximate the complex crater morphology, whereas more degraded craters are filled by the sediments driven by degradation processes that introduce the presence of convex landforms.

Since impact craters morphology is related to the absolute age of the area where they were emplaced, we expanded our analysis to six lunar maria, extracting over ~1000 simple impact craters from units with different absolute ages. The morphometric analysis on those craters have shown how the mean inner slopes can be a significant morphological marker to constrain the absolute age of the surfaces. In particular, older surfaces were characterized by lower mean slope values in function of crater diameters, suggesting dominance of old eroded craters (C3-C4) within their population. By contrast, the younger surfaces have shown higher mean slope values, suggesting a crater population dominated by recent fresh impacts (C1-C2). This trend is the expression of the morphological degradation, which is strictly connected to the lunar maria age. Moreover the geomorphometry distribution of impact craters population on a homogeneous surface is influenced by the surface absolute model age. Hence we can hypothesize to fix absolute age thresholds based on the morphological variations of impact craters and to constrain potential isochrones in function of crater diameters.

However this research represents only a preliminary attempt towards a new method for planetary surface age discrimination and surely needs to be further improved and calibrated by considering more surfaces on other lunar maria. Anyway the study has unambiguously shown that the surface morphometric approach, supported by a robust statistical analysis, is useful for the characterization and semi-automatic detection of the degradation classes of simple craters as well as for the age refinement of lunar geological units. In addition, being independent from impactor fluxes and scaling laws, this approach can be considered for future employments on other airless planetary bodies (such as Mercury and minor bodies), where the surface chronology is still uncertain, taking into consideration the differences of the target surfaces, such as for example strength, porosity, grain size and presence of ice.

APPENDIX

IS LINNÉ MORPHOLOGY INFLUENCED BY THE LUNAR STRATIGRAPHY? INSIGHTS FROM NUMERICAL MODELING

E. Martellato[1], V. Vivaldi[2,3], G. Cremonese[2], M. Massironi[3], A. Ninfo[3], F. Marzari[4], J. Haruyama[5]

1 Museum für Naturkunde, Leibniz Institut an der Humboldt-Universität Berlin, Invalidenstraße 43, 10115 Berlin, Germany
2 INAF-Osservatorio Astronomico di Padova, vic. Osservatorio 5, 35122, Padova, Italy
3 Dipartimento di Geoscienze, Università degli Studi di Padova, via Gradenigo 6, I-35131 Padova, Italy
4 Dipartimento di Fisica e Astronomia "Galileo Galilei", Università degli Studi di Padova, via Marzolo 8, 35131, Padova, Italy
5 Department of Solar System Sciences, Institute of Space and Astronautical Science, Japan Aerospace Exploration Agency, Sagamihara, Kanagawa 252-5210, Japan

In this paper my contribution concerned the geological setting introduction as well the topographic data description and analysis. In particular the main contribution of my research in this paper was the morphologic observations and the morphometric analysis of Linné crater, reported in the "*Results*", "*Discussions*" and "*Conclusions*" chapters.

ABSTRACT

Linné crater is a 2.22-km diameter and 0.53-km deep simple crater located in northwestern Mare Serenitatis. Recent high resolution data acquired by the Lunar Reconnaissance Orbiter Camera revealed that the interior of this crater is best described as an inverted truncated cone. Using the iSALE shock physics code, we modeled the Linné impact event to investigate the dependence of the final crater morphology on target properties, including material parameters and layering. Model results were compared to the topographic expression of the crater interior provided by the related Digital Terrain Model, slope and profile curvature, which highlighted the presence of a topographic step 100 m below the pre-impact surface. Comparison with numerical simulations showed that this interface can develop along the crater wall if the local surface is modeled as a double-layered target, where the upper layer has thicknesses ranging from 100 to 200 m, while the lower layer (basement) is at least 200 to 300 m thick. These two layers can be interpreted as the expression of two "compound individual flows", each one characterized by a similar composition. Alternatively, they may represent a unique volcanic inflated-like event.

INTRODUCTION

Impact cratering is one of the most important geological processes in terms of the formation and evolution of solid bodies (planets, asteroids, comets). Craters have accumulated on planetary and small bodies since the early phases of the formation of the Solar System, and record the cumulative effects of later collisions, volcanic emplacements, tectonics, landslides, aeolian activity, and space weathering (e.g., Chapman and Jones 1977, Neukum et al. 1975). During an impact event, the projectile transfers its kinetic energy to the target body (e.g., Collins et al. 2012, Melosh, 1989). The subsequent excavation flow opens a cavity, while target material is displaced, compacted or ejected. The growth of the crater is halted by strength and gravitational forces (e.g., O'Keefe and Ahrens 1993). In the "strength regime", the crater size is determined by the strength of the target material, and is proportional to cube root of the kinetic energy (e.g., Holsapple 1993). In the "gravity regime", gravity and target material properties are the main factors in constraining crater sizes. The transient cavity established at the end of the excavation flow undergoes further gravity-driven collapse that causes enlargement of the crater diameter and decrease of its depth (e.g., Wünnemann et al. 2011). The extent of such modification depends on the crater sizes. Simple craters are among the smaller impact structures (range of crater diameter D<15 km on the Moon, D<7 km on Mars and Mercury, D<4 km on the Earth, e.g., Melosh and Ivanov 1999), and they form by minor modifications of the transient cavity, including collapse of unshocked and/or melt materials from crater rim and walls down onto the floor, folding over of the crater lip and negligible elastic rebounding (e.g., Kenkmann et al. 2013, O'Keefe and Ahrens 1993). In homogenous targets, simple craters can be described by a bowl-shaped either parabolic- or cone-like morphology, with depth-to-diameter ratio (d/D) of about 1/5 (e.g., Chappelow and Sharpton 2002). However, the structure and composition of planetary crusts may deviate significantly from relatively homogeneous competent rocks. For instance, the Moon and small bodies are covered by regolith (e.g., Bart et al. 2011, Fa et al. 2015, Housen and Wilkening 1982), Mars is characterized by icy, regolith and rocky layers (e.g., Holt et al. 2008, Nowicki and Christensen 2007, Plaut et al. 2007, Schultz 2002), whereas, the Earth experiences the largest variations in terms of different lithologies and water content. Such variations within planetary crusts have a significant effect on the cratering process, and the final crater shape results from the balance between strength, composition, layering and the gravity field (e.g., Holsapple and Housen 2007, Housen and Holsapple 2003). Therefore, impact structures reflect the characteristics of planetary crusts, and can be used to explore near-surface stratigraphy.

Linné (Figure 1B) is an impact structure defined by circular raised and sharp rim with high-reflectance ejecta, suggesting that its current shape was not undergone significant degradation processes. It likely formed in the late Copernican period, within the last 10 Ma (e.g., Stickle et al. 2016). Due to its young age, Linné is one of the most striking examples

of pristine crater, and therefore it has been used so far as the archetype of simple craters by several authors (e.g., Hiesinger and Head 2006, Garvin et al. 2011, Wilhelms et al. 1987). It has been observed by several space missions (e.g., Lunar Orbiter, Apollo, Clementine, SELENE-Kaguya, and Lunar Reconnaissance Orbiter (LRO)). However, only the Lunar Reconnaissance Orbiter Narrow Angle Camera (LROC/NAC) (Robinson et al. 2010) acquired high resolution images (1 m pixel scales) from different points of view, allowing derivation of a Digital Terrain Model (DTM) of the crater. These new data of Linné crater revealed it to be a 2.22-km diameter and 0.53-km deep, with truncated-cone shape (Garvin et al. 2011), even though Linné was previously described as an example of a parabolic-shaped crater (e.g., Chappelow 2013, Melosh 2011). Chappelow (2013) used shadow measurement method on NAC images to evaluate the Linné profile, and found that it lies between the parabolic and pure "conic" shape.

Linné is located near the northwestern edge of Mare Serenitatis (27.74°N 11.76°E), and is likely to lie on top of a complex stratigraphic sequence of distinct volcanic events that piled up and formed a stack of solidified lava flows. Chronological studies based on crater counting techniques (Hiesinger et al. 2000) showed that Mare Serenitatis underwent magmatic activity from 2.44 to at least 3.81 Gyr ago. Estimation of the type of lunar volcanism and thicknesses of magmatic events was fulfilled in several studies, and the current widely accepted hypothesis relies on the idea that a mare unit is emplaced as multiple low-rate effusion events close to the same source vent (Schaber 1973b, Whitaker 1972). The thickness of the individual flows was estimated by using different approaches, from in-situ measurements by the Apollo astronauts (Howard et al. 1972), to photogrammetric measurements (e.g., Schaber 1973a), to chemical investigations on lunar samples (e.g., Brett 1975), to the presence of S-shaped kinks in the crater size-frequency distribution (Neukum and Horn 1976, Hiesinger et al. 2002), or the identification of layering in lava tube pit walls on remote sensing image (Robinson et al. 2012). All these studies indicated thin thicknesses of each individual flow within a given mare unit, from few meters to a few tens of meters.

Alternative approaches used radargrams from the Kaguya Lunar Radar Sounder (LRS) experiment (e.g., Ono et al. 2009, Pommerol et al. 2010). These data showed the presence of multiple reflectors in mare regions, which were associated with buried regolith layers between two subsequent magmatic events, and therefore may provide constraints on the thickness of a geologic unit (Oshigami et al., 2009, 2012, 2014). The upper stratigraphy of the lunar surface has been also inferred from impact crater shapes and associated ejecta deposits (e.g., De Hon 1979, Weider et al. 2010). The presence of a layered stratigraphy, where an upper weak layer overlays a competent one can cause the development of a flat-floor morphology when the ratio of crater diameter and the thickness of the upper weak layer is 8-10 (Quaide and Oberbeck, 1968, Senft and Stewart, 2007). On the other hand, as ejecta represent material excavated from depth, it can reveal the presence of a layered

stratigraphy if it is spectrally distinct from the surrounding surface (e.g., Ernst et al. 2010). For example, workers mapped color of ejecta from Clementine multispectral data and derived flows to be as much as several hundreds of meters thick in southeastern Mare Serenitatis (Ono et al. 2009, Pommerol et al. 2010, Weider et al. 2010). These estimates were referred to the thicknesses of mare units, since they were derived from composition-based approaches that were not able to discriminate individual magmatic events within a homogeneous mare unit (Robinson et al. 2012).

Therefore, Linné crater is expected to cross several individual lava flow emplacements, but it is not clear if it lies within one homogeneous mare unit or more. The truncated-cone shape of Linné can be explained either by specific characteristics of a homogeneous surface or by the cumulative effects of shock waves propagating into a number of layers with different rheological properties. It was indeed advanced that the composition of mare basalts can vary over time, and therefore distinct compound lava flows may display specific mechanical characteristics (Stickle et al. 2016 and references therein).

In this paper, we aim to investigate the origin of the truncated-cone shape of Linné by numerically modeling this impact event. By comparing the results of simulations with the crater DTM profiles, we discuss the characteristics of near-surface stratigraphy in the area where the crater formed. Additionally, we performed geomorphometric analyzes, in order to better constrain the near-surface stratigraphy, and discuss our findings in view of the geological evolution of the Serenitatis basin.

DATA

In this study, we used LROC images and derived topographic data to compare the results of our modeling, and provide constraints on the target properties and layering within Linné crater. The LROC NAC images we used (available through the Planetary Data System (PDS)) have a pixel scale of 0.5 m. The NAC images were orthorectified accounting for topographic and camera distortions, radiometrically calibrated to reflectance (Robinson et al. 2010, Humm et al. 2015), and map-projected through the U.S. Geological Survey Integrated Software for Images and Spectrometers (ISIS) software (e.g., Gaddis et al. 1997, Anderson et al. 2004). The NAC-derived DTM (also available through PDS) has 2 m/pixel scale with a m scale vertical accuracy. Since LROC was not designed as a stereo camera, the stereo observations of Linné crater were obtained by combining NAC images collected during two adjacent orbits on September 2010, with nearly identical solar illumination conditions and camera-surface orientation (Tran et al. 2010), and Lunar Orbiter Laser Altimeter (LOLA) profiles acquired along the crater center between June and September 2010 (e.g., Baker et al. 2016 and ref. therein).

The crater morphology was analyzed through ENvironment for Visualizing Images (ENVI) software package, and further processed on Environmental Systems Research Institute's (ESRI's) ArcGIS (Beyer 2015).
The elevation values provided by the NAC-derived DTM are the distance with respect to a reference sphere of radius equal to the mean lunar radius (1737.4 km) (Mazarico et al. 2010, Smith et al. 2010). However, the grid of the numerical simulations defined zero elevation at the pre-impact surface, which was given by the average elevation of the mare surrounding Linné crater, and correspond to -2620 m in the "DTM system". Therefore, in our analysis we adopted zero elevation as the reference of lunar elevation, by subtracting the elevation mean value to the DTM data.
Notwithstanding the Linné crater displays a symmetrical and smooth topography (Mahanti et al. 2014), local asymmetries due to gravitational landslides may occur. Therefore, the representative profile to be compared with modeling outputs is obtained by averaging eight topographic profiles starting from the crater center towards the rim following different directions.

GEOLOGICAL SETTING AND CRATER DESCRIPTION

Serenitatis basin, with its diameter of 920 km, is one of the three largest multiring structures located in the lunar Nearside. It is characterized by other four rings with diameters of 410, 620, 1300 and 1800 km (e.g., Head 1979). The time of its formation was inferred on the basis of both crater-counting techniques and radiogenic isotope measurements on lunar samples. However, while the first suggested a quite old age for Serenitatis (Hartmann and Wood 1971), the second produced no more than a range of ages spanning from 3.86 to 3.93 Ga, given the controversial correlation of the rocks collected at the Apollo landing sites to the Serenitatis impact event (e.g., Stoffler et al. 2006, Fassett et al. 2012, Spudis et al. 2011, and reference therein). The re-interpretation of the lunar samples constrained the age of the basin to 3.89 Ga, within the Nectarian period, when the Moon was undergoing a heavy bombardment by hundred-kilometer size asteroids (e.g., Stöffler et al. 2006). More recently, the new high-resolution data acquired by NASA LRO mission provided new clues for the understanding of the lunar stratigraphic sequence of large basins and supported a formation of the Serenitatis within the pre-Nectarian epoch (Fasset et al. 2012, Spudis et al. 2011).
The original floor of the Serenitatis basin was emplaced by multiple lava flows within a period spanning from 2.44 to 3.81 Ga ago (Figure 1A, modified from Hiesinger et al. 2000). The result of this long magmatic activity is a smooth plain, where 29 spectrally homogeneous lithological units can be distinguished on the basis of albedo, spectral properties and age. According to Hiesinger et al. (2000) geologic map (cf. also Figure 9 in Hiesinger et al. 2000), Linné is located in unit S14, which is dated back to 3.49 Ga ago.

This geological unit lies in contact with overlying younger geological units, having ages between 3.43 and 2.90 Ga ago, and it can likely superpose only unit S10 (3.60 Ga).

Measurements on the NAC-derived DTM of Linné showed that the crater is (2.22 ± 0.02) km in diameter and (0.53 ± 0.01) km in depth, and therefore it is defined by a depth-to-diameter (d/D) ratio of (0.24 ± 0.04). The crater rim has a sharp and edge-like appearance, and it is lined by a sequence of ridges and chutes, features observed also in other fresh craters (e.g., Watters et al. 2015). The uppermost 50-m steep walls of Linné are characterized by basaltic layer outcrops (see white arrow in Figure 1C) (Sharpton 2013). The upper inner wall is lined with patches of impact melt (see black arrow in Figure 1D) that were ejected, coalesced under gravity and then flowed back into the crater, forming drainage channels. These melt flows were recognized in only one part of the crater walls.

Furthermore, crater walls are superposed by debris flows (e.g., Garvin and Frawley 1998, Stopar et al. 2014, Xiao et al. 2013). Debris and rocky blocks up to few tens of meters in size are completely strewn over the floor of Linné, and form a lens extending up to a depth of about -200 m below the pre-impact surface, where the crater experiences a change in albedo (see black arrow in Figure 1D). Differences in albedo may be associated to either a different composition or a different degree of maturity of the soil (e.g., Blewett et al. 2005). In the case of Linné, the high-reflectance deposit might be associated to boulder and debris flows veneering the crater lower walls and floor, and characterized by a different composition and/or heterogeneous granulometry (see white arrow in Figure 1D).

This rocky sheet obscures, if present, any melt ponds. Melt can pool on smooth low-reflectance deposits on crater floors, and is recognizable for the presence of cooling fractures, pressure ridges and flow textures (Denevi et al. 2012, Neish et al. 2014, Stopar et al. 2014). Furthermore, the crater slope is expected to have undergone a steep change at the point of transition from crater walls to melt ponds (Stopar et al. 2014). Plescia and Cintala (2012) performed quantitative study on melt ponds based on statistics of highland simple craters observed by LROC, deriving the trend of impact melt pool size in function of their parent craters. For a Linné-sized crater, the melt pond diameter is about 500 m, which matches the bottom of Linné (also characterized by a clear-cut change with the crater walls). Therefore, even though no smooth terrain is identified on the floor of Linné, nor is the presence of low-albedo material, the presence of a melt pond under the rocky deposit cannot be completely ruled out.

Stickle et al. (2016) used the data acquired by the Miniature Radio Frequency (Mini-RF) instrument on board LRO to compute the radial circular polarization ratio (CPR) and derive the surface roughness of Linné. They found a low CPR at the crater rim, suggesting a region of fine-grained material in a shallow near-surface layer. They observed in addition that the CPR rises on the proximal ejecta, which likely denotes the presence of unweathered meter-sized blocky material. The continuous ejecta of Linné, which extends up to 8 km

from the crater center, is indeed characterized by a high albedo emblematic of very young surfaces (e.g., Nettles et al. 2011).

METHODS

Approach to Numerical Modeling

Our current understanding of the impact process results from a multidisciplinary approach including geological and structural mapping, remote sensing, geophysical imaging, petrographic analysis of impact products, laboratory-scale analogue experiments, isotopic and elemental geochemical analysis, and real-scale computer simulations. The latter, numerical modeling of dynamic processes is carried out by means of the so-called shock physics codes (Johnson and Anderson 1987). Such codes allow for a quantitative simulation of the propagation of shock waves and the behaviors of matter over a broad range of stress states and deformation rates (e.g., Pierazzo et al. 2008). They are based on the equations of conservation of mass, momentum, and energy (the so-called compressible Navier-Stokes equations). The material response is quantified by constitutive equations, which are formulated as Equations of States (EoS) and strength models, governing the bulk thermodynamic material response and deviatoric deformations, respectively.
iSALE is one shock physics code (Wünnemann et al., 2006) largely employed in impact cratering studies (e.g., Collins et al. 2008, Wünnemann et al. 2008). This code is a multi-rheology, multi-material extension of the SALE hydrocode (Amsden et al. 1980), which relies on an elasto-plastic constitutive model, fragmentation models, a number of EoS, multiple materials, and the ε-α porosity compaction model (Collins et al. 2004, 2011a, Ivanov et al. 1997, Melosh et al. 1992, Wünnemann et al. 2006). It is well tested against laboratory experiments at low and high strain-rates (Wünnemann et al. 2006), and other hydrocodes (Pierazzo et al. 2008).

Initial conditions

We simulated the formation of Linné crater by means of iSALE. We use an Eulerian approach, which describes the instantaneous state of the material in each fixed cell, but is unable to follow a point in the material through the mesh. Since information regarding the thermodynamic history of these points is lost, we used Lagrangian tracer particles to record the material position and state during crater formation.
A number of simulations were carried out to test different models, varying the projectile dimensions, material parameters and the number of layers used to describe the lunar surface in order to obtain the best agreement between models and observations. The grid where the crater forms is made up by a high resolution zone covering the impact area, which had

dimensions on the real world of 2.3 × 2.5 km. This zone was surrounded by a zone of progressively lower resolution, where the cell is increased by a factor of 1.05 from the previous cell, in order to avoid spurious shock wave reflections at the target boundaries.

The projectile was simplified to a basaltic homogeneous sphere, due to the higher probability of an asteroidal composition for the impactor population on the Earth-Moon system (>90%: Chyba 1991, Pierazzo and Chyba 1999). The radius was varied between 38 and 48 m, in order to obtain a 2.22-km diameter crater and preserve a good fit with the measured crater diameter while testing target properties and layering. The crater size obtained from the various model setups resulted highly sensitive to the target characteristics, in particular layering. However, we kept constant the projectile resolution to 10 cppr (cell per projectile radius), a value that allowed to have the completion of the simulations in reasonable computational time (lower projectile dimensions needs more computation time). Cell resolutions therefore ranged between 3.8 and 4.8 m. The mean impact velocity of asteroids on the Moon is 18 km/s (Marchi et al. 2009). Due to the 2D nature of iSALE, the impact is modeled as perpendicular to the target surface. Notwithstanding perpendicular impacts are not common in nature, craters show no evidence of an oblique incidence of the impactors until very low impact angles (e.g., Collins et al. 2011b, Gault and Wedekind 1978). On the other hand, ejecta may represent a better marker of an eventual projectile obliquity (e.g., Pierazzo and Melosh 2000a). In the case of Linné, its ejecta are quite symmetric and display no peculiar pattern. Therefore, vertical impact at 18 km/s is a good approximation for our simulations.

The target was approximated as an infinite half-space, with a basaltic composition, which best represents the material of lunar maria. The thermodynamic behavior and compressibility of basalt is given by the ANalytical Equation Of State (ANEOS) (Pierazzo et al. 2005). A lunar surface gravitational acceleration of 1.62 ms−2 was used. The lunar interior was modeled with a uniform temperature of 273 K. This assumption can be a good approximation for the upper few hundreds of meters of a relatively young lunar surface. According to the thermal evolution of the Moon, the lithosphere was growing to the detriment of the partial melt zone which ceased between 3.4 and 2.2 Ga ago (Spohn et al. 2001), well before of the 10 Ma suggested for the Linné impact event.

We tested several target configurations for the formation of Linné, aiming at exploring whether the truncated-cone shape of the crater derives from either the peculiar property and state of basaltic lava flows or the presence of layering influencing the propagation of impact-generated shock waves. The first approach (case A) treated the target as one homogeneous layer (hereafter referred as the basement). The further approaches increased the target complexity, adding one or more layers atop the basement. Such layers approximated more recent magmatic events emplaced over older solidified lava flows (reproduced in our model by the basement). These lava flows can differ in composition and mechanical properties, due to variations of magma emplaced in different geologic times

and/or through different volcanic vents (e.g., Hiesinger et al. 2001). Therefore, it is not unrealistic to describe the additional upper layers with different material properties from the basement. In order to clearly distinguish the upper layers/younger lava units from the basement/older lava units, we modeled the first ones with fractured basalt. In the second approach (case B), the target is thus made up by an upper layer with variable thickness ranging between 50 and 400 m on top of the intact basement. In the last approach (case C), two 100 m thick upper layers, with the lower stronger than the upper one, are laying atop the basement.

A last word about our model assumptions regards regolith, the unconsolidated fine-grained material that covers the lunar surface and is produced by subsequent impacts and space weathering. Such a regolith layer is not included in neither of our three models, because it would be barely resolved. Earlier estimates based on the Surveyor mission landers indicated that this weakly cohesive material can be found at 1 to 20 m depths (e.g., Jaffe 1969b). Other in-situ estimates based on the analyzes of impact craters and ejecta morphologies provided values ranging from few meters to a few tens of meters (e.g., Basilevsky et al. 2015). A 4-m thick regolith layer was found at Mare Serenitatis on the basis of Earth-based radar and optical data (Shkuratov and Bondarenko 2001). A mean thickness of 2-4 m in mare regions were also found from the analysis of crater geometry (Bart et al. 2011), while the same methodology applied to the Sinus Iridum region gave a regolith thickness ranging from about 5 to 11 m (Fa et al. 2015). These works suggested that the regolith blanket at the Linné impact site can be likely a very thin layer, resolvable by at most a couple of cells according to the resolutions used in our models, and thus it would have had only a negligible effect on the final results.

A crude estimate of the regolith thickness at the Linné impact site can be performed by using eq. 9 in Bart and Melosh (2010). They studied the effects of a regolith blanket on the ejecta emplacement for craters in the range of hundreds of meters, finding that shallower the regolith layer is, further the distance rocky blocks are ejected from the crater. Eq. 9 allowed to compute the maximum distance of boulders ejected on a 45° ballistic trajectory, when the target is made up of a layer of regolith on top a consolidated substratum. In the case of a 4-m regolith layer, the expected maximum ejecta range is about 7 km for a Linné-sized crater, while it can reach 20 km if the regolith thickness drops down to 1 m. In the case of Linné, the discontinuous ejecta can be observed as far as 30-40 m from the crater center, which is almost twice the value found with the relation provided by Bart and Melosh (2010). Although the equation was derived for a different crater diameter range than the Linné size, it may suggest that the regolith may have not played an important role in the formation of the crater, and a regolith-free target can be a proxy for the lunar surface at Linné impact site.

Strength model for the target

The layering distinction in cases B and C are implemented as differences in the rheological model and in the strength values. The upper fractured layer is described by a linear-dependent strength model, the Drucker-Prager model (e.g., Drucker and Prager 1952). In this case, the shear strength Y is computed as a function of the cohesive strength at zero pressure Y0 and the coefficient of internal friction μ: the fractured nature of this layer is also given by the activation of porosity (Wünnemann et al. 2006). Porosity was fixed to 10%, which is a likely value for basaltic maria from laboratory density measurements Apollo samples (e.g., Kiefer et al. 2012) and Kaguya LRS data on Mare Serenitatis lava flows (e.g., Ishiyama et al. 2013).

The basement layer, which corresponds to the whole target in case A and the lower competent layer in cases B and C and, is instead described by a pressure and damage-dependent strength model described and implemented by Collins et al. (2004). The strength Y depends on the deformational history, as given in the following equation (Ivanov et al. 1997):

where Yi and Yd are the static strength of the intact and damaged material respectively, and D is the damage and can varies between 0 and 1, and increases as a function of plastic strain (see Collins et al. 2004, for details). In our simulations, we set the basement to be initially partially damaged (damage = 0.25). The static strength of the intact basement was represented by the Lundborg (1968) approximation:

where Yi0 is the shear strength at zero pressure (cohesion of the intact material at zero pressure), μi is the coefficient of internal friction, and YM is the von Mises plastic limit of the material. In the presence of a fully fractured material, the damaged strength at zero pressure is given by frictional forces between the fragments, and represented by Drucker-Prager model:

where Yd0 is the effective cohesion of the damaged material, μd is the coefficient of friction at low pressure. No porosity was set for the basement, in order to make more substantial the difference between the two layers.

Furthermore, no acoustic fluidization is assumed. Firstly theorized by Melosh (1979), this mechanism was implemented in iSALE in a simpler mathematical approximation called "block model" (Wünnemann and Ivanov 2003). Acoustic fluidization causes the material to weaken and flow in a fluid-like manner when subjected to strong vibrations, and it is invoked in the formation of complex crater to allow deep-seated gravitational collapse of the transient cavity (Melosh 1979, Melosh and Ivanov 1999). Being the Linné structure of modest dimensions, the acoustic fluidization would have only a negligible contribution on the rock debris flow and the final crater morphology, and thus it was not taken into account in our models (Senft and Stewart 2007).

RESULTS

In this section, we present the results of the simulations, for the three cases: (A) 1-layer target, (B) 2-layer target, and (C) 3-layer target. The best-fit models for all the three cases were determined by comparing the outcome of the simulations with the Linné DTM profile. The expected errors on the crater dimensions are about 10%, according to validation tests of iSALE simulations against laboratory experiments of an aluminum on aluminum impact (Pierazzo et al. 2008).
In Table 1, we summarized the projectile dimensions we adopted to run the different model configurations. It also lists the target rock strength model parameters implemented in this study to obtain the best fit with the topographic profile (see Collins et al. 2004 for further parameter description).

The formation process

Figure 2 illustrates the impact process simulated with iSALE shock code for two Linné-sized impacts into target with different layering. On the right side, it is shown the 1-layer configuration, while on the left one, the 2-layer configuration with an upper 100-m thick crust. During the first minutes after the impact event, an approximately hemispherical cavity is produced and expands (Figure 2A) by material displacement from the impact point until its maximum depth is reached (~500 m, cf. Figure 2B). Part of melt and high-shocked material lines the cavity, while part is ejected away from the impact site and covers the region surrounding the cavity (Figure 2C). At this stage, both the two models present a similar bowl-shaped cavity, but they experience a different degree of crater collapse. The 1-layer configuration remains mostly unaltered from the transient cavity (Figure 2D, right side). On the other hand, the 2-layer configuration undergoes modification, as material collapse into the crater floor (Figure 2D, left side). The result is a shallower crater with respect to the 1-layer case. Strain is greater on the crater wall and floor, and is thicker in the 2-layer configuration, but it rapidly decreases outwardly and remains localized in a thin sheet near the surface.

<u>Setup A: 1-layer target</u>

In order to investigate the effect of material properties on crater formation, we used a 3.8 m radius projectile impacting on a single homogeneous basaltic layer, varying both the intact and damaged cohesions and friction coefficients. A number of studies has been focused in the understanding of the lunar surface characteristics, in particular in quantifying its density, porosity, cohesion and angle of friction. Strengths of geological materials range from kPa for soils to tens of MPa for the competent rocks. Earlier works based on the

Apollo mission sample analyzes and strength experiments estimated cohesions ranging from ~0.2 to 3 kPa for the upper few centimeters of the lunar surface, but stronger material was expected with increasing depths (e.g., Carrier et al. 1991, Costes and Mitchell 1970, Jaffe 1969a,1969b, 1973). A cohesion of 10 MPa for intact basalt rocks was used by Pierazzo et al. (2005) and derived from fits to laboratory quasi-static triaxial test data. However, this value might not be representative of large-scale geology, since the lunar surface is subject to deformations in the brittle regime, including faults and dilatant cracks (Holsapple 1993, Schultz 1995). Therefore, crustal cohesion can be one to two orders of magnitude lower than the corresponding values for intact basalt.

The results of the one-layer configuration were shown in Figure 3, where the Linné topographic profile is outlined by a solid thick line, while the modeled crater profiles are represented as a shadowed region. Variations of the intact cohesion Yi0 (from 0.1 MPa to 10 MPa) did not produce large modifications in the crater shape, but it caused the decrease of about 12% in the diameter and 9% in the depth values (Figure 3A). The d/D changed slightly from 0.26 to 0.25 with increasing cohesion. The crater slope did not vary significantly, being about 34-35° in all the cases. The increase of μi (from 1.2 to 2) caused a diameter decrease of 9%, and a depth decrease of 3%. The d/D experienced an increase from 0.26 to 0.27, and the crater slope varied from 35 to 37° (Figure 3B).

We found that the damaged cohesion Yd0 is the parameter responsible for the most severe variations in the final crater morphology. We tested cohesion values from 10 Pa to 1 MPa, while keeping constant all the other material parameters (cf. Figure 3C and 3D). Craters developing in low cohesion targets displayed a conic shape with rims poorly defined (Figure 3C), while craters forming in higher cohesion targets were bowl-shaped (Figure 3D). Figure 4 illustrates the model results for a sample of tested damaged cohesions, and precisely 10 Pa, 10 kPa and 1 MPa. Each plot displays the plastic strain map on a grey scale, overlaid by Lagrangian tracer particles. The tracers measure the deformation of the target caused by the shock waves propagation and the consequent material displacement. At higher cohesions (1 MPa), deformation was mainly localized at the crater rim, where the target rocks were uplifted and overturned (Figure 4C). The final crater was bowl-shaped, with raised rims and no material deposit on the floor. It thus developed after a negligible modification of the transient cavity. As cohesion decreases, the final impact structure showed the presence of fragmentation along the crater walls and floor, which derived from target rock slumping (Figures 4A and B). The lower the cohesion, the higher the fragmentation extent, the thicker the breccia lens on the crater floor was (10 Pa vs. 10 kPa). The resulting crater developed therefore a conic-like shape, which was ascribed to a greater amount of debris flows. Such dependence of the impact process on the target cohesion can therefore explain the differentiation in the final crater morphology, i.e. either conic- or parabolic-shape, observed in the simple crater population on the lunar landscape.

Furthermore, Figures 3C and 3D highlight that the transition from conic-shaped to bowl-shaped craters is not progressive, but there is instead a sudden jump in the morphology at the cohesion Yd0 of 10 kPa. In the case of conic-shaped craters (Yd0≤10 kPa), the crater diameter ranges from (2.23 ± 0.22) to (2.32 ± 0.23) km, and the depth varied between (0.50 ± 0.05) and (0.58 ± 0.06) km (d/D ranges from 0.22 to 0.26). On the other hand, in the case of bowl-shaped craters (Yd0>10 kPa), crater depth was higher than (0.63 ± 0.06) km. For the higher value of cohesion tested, the diameter decreased as much as (1.56 ± 0.16) km (d/D=0.40). This trend was also underlined by the crater wall slopes. At lower cohesion values, slope exhibit a modest increase of 3° (from 27° to 30°) over three orders of cohesion magnitude. At Yd0 =10 kPa, the slope undergoes a sudden jump to 35°. In the higher cohesion range, slope is higher than 40°. Significant variations in the final crater morphology were found also by varying the friction coefficient. We observed that the smaller the coefficient of friction μd, the shallower the resulting crater was (Figure 3E). In particular, when setting the value of 0.35 characteristics of weaker target, we obtained a truncated-cone crater, with larger diameter and lower depth (D=(2.82 ± 0.28) km, d=(0.30 ± 0.1) km, d/D=0.11) than the 0.6 case. As shown in Figure 5, the 0.35-ud crater (Figure 5A) developed after a much more severe slumping of the rim material into the crater floor, in comparison with the 0.6 case (Figure 5B) where the slumping was negligible. We determined that in low friction coefficient targets the transient cavity can be filled up to 50% its depth. Such higher material collapse caused the inner wall slope to drop down to ~10°.

Setup B: 2-layer target

As shown by the results of one layer configuration (setup A), truncated-cone shapes can develop in homogeneous low damaged cohesion Yd0 targets. However, the observed Linné morphology was not perfectly reproduced in the 1 layer configuration. Even though the depth difference between the best fit simulation and observations was within the modeling accuracy, the modeled crater slope differed by 4° from the measured one. Therefore, we tested if any increase in the complexity of the target stratigraphy can lead to a better agreement between model and observation. In this second configuration, we modeled the target as a doubled-layered half-space, where the two layers are characterized by a different degree of fracturation. For the basement, we set the damaged cohesion to 10 kPa, i.e. the value identified as threshold between the conic- and the bowl-shaped crater morphology, while we set the intact cohesive strength one order of magnitude weaker than in quasi-static laboratory tests. We tested different thickness of the upper layer, ranging from 50 to 400 m. Figure 6 illustrates the results of this analysis. Plots on the left column show strain and deformation within the crater, post-impact, overlaid by a Lagrangian grid. The comparison

of the models with the topographic profile of Linné is provided on the right column of Figure 6.

In the case of thinner fractured layers, i.e. 50 and 100 m (Figures 6A and 6B), a smaller projectile is needed to fit the Linné diameter (2.22 km). It was 38 and 40 m in radius, respectively for the two thicknesses. The forming craters fully penetrated the upper layer, and hence they predominantly developed in the harder crust material (basement). During the crater formation, target material was displaced and ejected from the excavated zone of the transient cavity. Target stratigraphy was preserved all around the crater, but was uplifted and overturned at its rim creating an isoclinal recumbent fold (e.g., Collins et al. 2012, Melosh 1989, Reimold et al. 1998, Sharpton 2014). In this case of thin upper layers, the rim of the modeled craters was composed by the basement material. Plastic strain accumulated during the impact was localized on the crater walls. The floor resulted poorly fractured for the 50 m-case, while it was covered by a slightly thicker breccia deposit in the 100 m-layer case (10% of transient cavity depth). The crater diameters were (2.18 ± 0.21) km and (2.24 ± 0.22) km, while depths were (0.59 ± 0.06) km and (0.55 ± 0.05) km, respectively for the two cases. The final d/D ratio turned out to be 0.27 and 0.24, respectively. Finally, the crater wall slopes were 34° and 32°, respectively in the 50 m- and 100 m-layer configurations.

A 42 m radius projectile was adopted to fit Linné topographic profile when an intermediate thickness (200 and 250 m) of the upper layer was set (Figures 6C and D). The crater diameters were (2.21 ± 0.22) and (2.12 ± 0.21) km, and depths were (0.59 ± 0.06) and (0.58 ± 0.06) km, respectively. A d/D ratio of 0.27 was obtained in both cases. The crater slope resulted slightly higher in the 250-m case (37° vs. 35°). In these models with intermediate upper layer thicknesses, the crater formed prevalently in the upper fractured layer, but its final depth and morphology were affected by the presence of the harder lower basement. The inner walls were fractured, but the upper layer material did not contribute to the thin breccia lens covering the crater floor.

We finally considered thicker upper layers, with values of 300 (Figure 6E) and 400 m (Figure 6F). In order to derive the best fit with the measured crater diameter, projectiles of 45 and 48 m were used respectively in the 300 m- and 400 m-layer. The modeled crater diameters were (2.24 ± 0.22) and (2.19 ± 0.22) km, respectively. Being the depth equal to (0.60 ± 0.06) and (0.52 ± 0.05) for the two cases, the d/D ratio resulted of 0.27 and 0.24 respectively. In the case of a 300 m upper layer (Figure 6E), the crater developed in both the fractured and the basement layers. The upper layer material flowed into the crater floor, and originated a very thin veneer of rocky debris. The resulting crater had an inner slope of 36°. On the other hand, when the upper layer was fixed to 400 m (Figure 6F), the modeled crater did not succeed in penetrating the fractured layer and reaching the basement, and hence it formed entirely in the upper weaker layer. In this last model setup, the crater

exhibited a thicker breccia lens (10% of the transient cavity) lining its floor than the previous cases.
We noticed that all these models originated a relatively thin breccia lens lining the crater floor, reaching a maximum value of 10% the transient cavity depth (100-m and 400-m upper layer thicknesses).

Setup C: 3-layer target

In this last target configuration, we modeled the formation of the Linné crater in a 3-layer target, where the layer transitions were set to 100 and 200 m under the pre-impact surface. The simulated target stratigraphy was therefore made up by 100 m of fractured basalt on top of 100 m of an intermediate basaltic layer, which in turn overlaid the (basaltic) basement. Each layer was described by specific rheological and/or mechanical properties, in order to represent a clearly distinguishable layer. The upper layer is distinguishable for the strength model adopted (Drucker-Prager vs. Collins et al. 2004), whereas the lower two basaltic layers differ each other for the implemented strength values (cf. Tab. 1).
We tested several projectile dimensions, finding that the Linné diameter was matched when adopted a 42-m radius projectile. In this 3-layer configuration (Figure 7), the model did not fit the Linné morphology, because the simulated crater exhibited a concentric terrace within the inner wall. Such wall change may likely develop from the severe strength differences we set between the three layers. The choice of a less extreme difference in the strength values between the target layers might lead to a better match between model and observation, but, at the same time, suggest that except the potential presence of an upper fractured layer, only small strength variations can occur at the impact site. Therefore, if present, any layering below the upper fractured layer (100 m in this specific model configuration) can not be resolved by the modeling, and the lunar surface can be considered homogenous.

Crater Morphometry

Morphometric studies on impact craters have been a long used practice to quantitatively characterize such landforms. These investigations mainly relied on shadow measurements (e.g., Chappelow 2013, Chappelow and Sharpton 2002, Pike 1980) or photoclinometry (e.g., Bray et al. 2008, Craddock and Howard 2000, Davis and Soderblom 1984, Fasset and Thomson 2014), however, the recent availability of elevation data allowed to derive more accurate and detailed description of impact craters (e.g., Basilevsky et al. 2014, Herrick and Sharpton 2000, Salamunićcar et al. 2012, Watters et al. 2015). The present study analyzed the morphology of Linné crater by processing the elevation topographic map of the crater through ENVI and ArcGIS softwares and quantitatively determining specific morphometric

characteristics of this impact structure. Our goal is to compare these morphometric variables extracted from the crater DTM to the results of numerical simulations and test the predictions of our models.

First of all, we fit the shape of the Linné crater with a nonlinear least-squares power law and derived the exponent αc (cf. Watters et al. 2015 for details). We found a value of αc=1.40 ± 0.44 on the mean DTM profile, and is in agreement with the αc=1.46 value found by Garvin et al. (2011). According to Watters et al. (2015), this value lies between the two extremes of craters with a conic- (αc=1) and parabolic- (αc=2) shape, and it is similar to the exponent found for Martian small unmodified craters forming in low strength targets (αc=1.56).

The variables computed from topographic elevation of Linné were slope and curvature. The topographic slope is the first derivative of elevation, geometrically seen as the plane tangent to the surface at a certain elevation point, and represents the absolute value of the topographic gradient (e.g., Kreslavsky and Head 2016). Figure 8B shows the bidimensional slope map of Linné crater, while Figure 9B the slope values taken along the profile AA' in Figure 8. We found that the rim crest is characterized by a mean slope of nearly 0°, a value that is representative of very sharp rims. The presence of steep rims has been widely referred to as parameter to identify fresh craters (e.g., Barlow 2004, Craddock et al., 1997, 2000, Garvin et al. 2000). However, recent studies highlighted that this is not a global property to identify fresh impact structure. As for instance, Watters et al. (2015) showed that on Mars, pristine impact structures smaller than 1 km in diameter have rim less sharp than older larger simple craters. Scaling to the Moon, Linné-sized craters fall within the class of large simple craters, having steep rims as parameter qualifying their freshness. Surficial degradation processes then work to modify the impact structure, causing the rim to lower, widen, and round up to loose any topographic elevation (e.g., Craddock et al. 1997). The upper cavity slope of Linné was 45°, and is similar to the slope measured on the Martian unmodified craters with diameter larger than 1 km (Watters et al. 2015).

The inner wall is defined by a mean slope of ~31°, which fell in the angle of repose range expected for normal dune slope faces (30°-35°; Atwood-Stone and McEwen 2013, Watters et al. 2015). This value was lower than the maximum angle of repose associated to parabolic-shaped craters (~35°, Daubar et al. 2014), whereas is in agreement with the angle of repose observed in the lunar regolith (~31°, Bart et al. 2011). This may denote that the crater wall is composed by broken rock debris fallen down from the rim (Melosh 1989). The unmodified crater population on Mars (with diameter larger than 1 km) turned to have inner wall slopes somehow higher than the Linné case (about 35°, cf. Figure 12a in Watters et al. 2015). The outer scarp presents a mean slope of ~10°.

Profile curvature is the second derivative of elevation and represents the curvature in the gradient direction (e.g., Bue and Stempiski 2007). Since it measures variations in the slope angle of surfaces, it identifies and emphasizes the areas of concavity and convexity

(negative and positive values, respectively) at the sides of points of topographic inflection. Therefore, profile curvature is the best terrain attribute to reveal changes distributed perpendicular to the maximum slope direction in the crater morphology, as for instance the rim down-faulted annular trough located along the inner wall. Such trough can originated during the impact cratering process, ranging from the stepped terraces separated by scarps on large (complex) craters (Kenkmann et al. 2013), to subtle steps marking shocked and unshocked debris lens on smaller (simple) craters (Grieve 1987). On the other hand, troughs can be also found at the interface between two different layers. Layers can be found on lunar maria, which formed by overlapping lava flow emplacements within billions of years. During this lapse of time, the composition and characteristics of magma can have likely varied (Hiesinger et al. 2001), causing differences in the rheological properties of two contiguous layers/lava units. Therefore, if compositionally different layers are exposed by an impact, they likely degrade at a different rate, producing subtle trough along the inner wall.

In order to reliably estimate the profile curvature, we applied a smoothing filter to the elevation map (e.g., Bue and Stempiski 2007, Kreslavsky and Head 2013, Rosenburg et al. 2011). The second derivative is indeed very sensitive to any roughness of the surface, as well as to the accuracy and resolution of the DTM, and the algorithm used for computation (Evans 1998). Therefore, we convolved each point of the DTM with a kernel. We tested different kernel sizes and finally chose a kernel size of 33×33, which represented a compromise between maximization of visual sharpness of the map and lower noise.

The 33×33 kernel was applied to Linné elevation map to create a binary image of the crater and draw the map of profile curvature. Figure 8C shows the result of this processing sequence, where we notice the presence of three faint rings that runs with a different degree of continuity along the wall of Linné. These rings were also shown in a profile curvature vs. crater radial profile plot (Figure 9C). In Figure 9A we indicated with arrows the corresponding points along the crater inner wall where such inflection points occur.

These negative curvature peaks occur in correspondence of oscillations of the topographic slope of the crater wall. However, being such rings very faint features, we further post-processed the profile curvature map in order to make them more clearly distinguishable from the background. We enhanced crater concavities (negative values) through a "3-threshold classification" method. Such technique relied in merging the zero, positive and negative values of the profile curvature in three separate classes, then setting to zero all the positive values, and finally showing only the negative ones. The result of this procedure is given in Figure 10, which emphasizes and resolves the three rings only perceived on the profile curvature map. These rings are located along the inner crater wall at +20, -100 to -120, and -200 to -220 m.

Even though these three rings might be only an overemphasis of tiny variations of the crater slope ascribable to subtle effects of the cratering mechanics, at least two of these rings can

be associated to observed features. The ring at elevation +20 m is fully continuous along the crater wall, and thus it can identify a strong material interface such the transition from the ejecta deposit to the structurally-uplifted rim. At this elevation, layered outcrops were observed (Sharpton 2014). The ring at depth -200 m occurred at the albedo transition, and it may mark the extent of the breccia lens. This ring is indeed defined by large discontinuities along the crater wall, suggesting that it is associated to asymmetries caused by local variations of debris flows.

The median ring at -100 m is mostly continuous along the entire crater wall. If it may represent real crater features like the other two topographic steps, it denotes the presence of a convex morphology developed after mass wasting or differential erosional rate between layers with different composition and mechanical properties (Hiesinger et al. 2001). However, a debris deposit originated by gravitational collapse of target material already occurs at a deeper depth (-200 m), and it seems unlikely that it can extend up to a further shallower depth (-100 m) developing a symmetrical face. Even though we can not completely rule out the gravitational hypothesis, we supported that the median ring at -100 m identifies an interface between two layers characterized by a different rheology.

DISCUSSION

In this section, we provide a discussion of the results, including implications for understanding the stratigraphic evolution of Mare Serenitatis, on the basis of the numerical analysis and morphometric considerations. In this study, we performed numerical modeling of the Linné crater, a 2.22 km diameter and 0.58 km deep truncated-cone shaped impact structure, located in the northwestern side of Mare Serenitatis. It distinguishes among the crater population for its high freshness degree, which is suggested by crispy rims and high-reflectance ejecta. Therefore, it has long been used as proxy for simple craters, and this raised the necessity to better understand how the crater formed and in which impact conditions (e.g., projectile and target properties).

Given a natural impact structure, it is not straightforward to retrieve information about the projectile that have originated it, since different combinations of composition, speed and angle of impact can produce similar results (e.g., Melosh 1989). Many studies have focused on the effects of impact angle on the final shape of impact structures (e.g., Gault and Wedekind 1978, Pierazzo and Melosh 2000a), but they all agreed on the circularity of the final crater down to impact angle of about 30°. However, experimental and numerical studies highlighted that the impact angle does have a great effect on quantities like crater efficiency, vaporization energy, shock pressure and melt production (e.g., Pierazzo and Melosh 2000a, Schultz 1996). As for instance, the volume of melt decreases to 80%, 50% and 90% in comparison to a vertical impact, at the respective impact angles of 45°, 30° and 15° (Pierazzo and Melosh 2000b). However, the total volume of impact melt can not be

directly measured on natural impact craters, thus it can not be used to constrain the impact angle. In remote sensing image, the ejecta distribution can be rather the more suitable parameter to provide some clues on the projectile direction (Gault and Wedekind 1978). At impact angle below 45°, ejecta become asymmetric and develop a characteristic "butterfly wing" pattern.

In the LROC NAC image of Linné crater, we did not notice any asymmetric pattern on the ejecta blanket, hence the Linné impact might plausibly have occurred at an impact angle greater than 45°, though is expected to be at least moderately oblique. Laboratory experiments performed on different substances ranging from metals to rocky materials highlighted the independence of the d/D ratio for angles varying between 0° and 45° when impact velocities are above the target sound speed (e.g., Burchell and Whitehorn 2003, Gault 1973, Love et al. 1994, Michikami et al. 2014). Therefore, the assumption adopted in our numerical models of vertical impact and the use of the full velocity value of incoming meteoroids on the Moon (18 km/s) without any angle correction can be a reliable proxy for the formation of Linné crater, and any small dependence of the d/D ratio on the impact angle can be accounted within the model uncertainties.

The final morphology of craters depends in addition on the target properties. Therefore, we spanned several target configurations, including layering. In the 1-layer target, we observed that the highest variations occurred when varying cohesive strength (Figures 3B, 3C, and 4) or friction coefficient (Figures 3E and 5) for damaged material. We tested damaged cohesive strengths ranging from 10 Pa to 1 MPa. We observed that craters forming in low cohesion targets ($Yd0 \leq 10$ kPa) developed a conic shape, which varied about 15% in the d/D ratio and 3° in the inner slope over three orders of cohesion magnitude. On the other hand, craters forming in high cohesion targets ($Yd0 > 10$ kPa) are rather closer to a parabolic shape, with higher d/D ratio (0.4 for $Yd0 = 1$ MPa) and higher inner crater slope (~63°). A similar result was also found by Watters et al. (2015), who performed a morphometric analysis on a statistical sample of Martian craters. Even though they did not provide any ultimate conclusion on how the cavity shape depends on terrain type, they had observed indeed a predominance of conic-shaped craters in weaker terrains. On the other hand, several investigations showed that the d/D ratio is larger for fresh craters forming in high-cohesion target, since stronger materials can better support steeper slopes (e.g., Atwood-Stone and McEwen 2013, Daubar et al. 2014).

The friction coefficient is the parameter responsible of the degree of slumping of the rim into the crater floor. We indeed observed that a coefficient of friction of 0.35 caused the formation of a breccia lens as thick as half the depth of transient cavity. This lens shallows the final crater and decreases the inner crater slope (Figure 5). At the same time, the diameter widened as much as 25% with respect to the simulation considering a friction coefficient of 0.6.

According to all the simulations performed in a 1-layer target, the better fit with the Linné crater was obtained by assuming a 1 MPa intact cohesive strength and a 10 kPa damaged cohesive strength. The final diameter resulted (2.24 ± 0.22) km. This specific model did not perfectly match the measured topographic profile, because it had a higher depth (9%), slope (13%), and aspect ratio d/D (8%). Even though these values fall within the model uncertainties, a better agreement between models and observations considering a homogeneous 1-layer target configuration may be obtained by including dilatancy in the modeling. However, this parameter was not implemented on the iSALE version we used to run our models, therefore we can only discuss here the possible effects of dilatancy on crater formation.

Dilatancy represents the development of porosity in the crater wall and floor due to fracturing and brecciation created during the shear-dominated cratering flow (Collins 2014). Only few study have been conducted so far to explore how the final crater morphometry is modified by dilatancy (Artemieva et al. 2004, Collins 2014, O'Keefe et al. 2001). These studies highlighted that dilatancy accounts for correctly explaining the breccia lens in terrestrial simple impact structure, and can decrease the final crater depth as much as 20% (Collins 2014). On the other hand, the effects of dilatancy on the formation of lunar craters are less straightforward, since two facing aspects contribute to the final result. Dilatancy is more efficient on smaller planetary bodies, but, at the same time, it is less efficient in high-porosity terrains (Collins 2014). On the basis of these considerations, we can only observe that dilatancy may indeed account for the mismatch in crater depth between the best fit model and Linné topographic elevation.

Nevertheless the role of dilatancy, another interesting picture of the formation of Linné can be drawn when considering a double layered target. We examined the effects on the final crater shape of an upper fractured layer with thicknesses varying between 50 and 400 m. The modeled craters are all truncated-cone shaped, with a variation of 12% in the d/D ratio and 15% in the inner crater slope, over the range of the thicknesses tested. In Figure 6 (column on the right side), we compared the modeling result with Linné topographic elevation, finding that the better agreement is obtained when the upper fractured layer is either 100 m or 400 m thick. However, on the basis of the only elevation datum, all the thickness of the upper fractured layer considered in this study can account for the shape of Linné, since the final depth of the simulated craters differ by up to ~13% from the topographic profile, value which is of the order of the model uncertainties.

In both the 1-layer and 2-layer configurations, we noticed that a relatively thin breccia lens deposited on the crater floor, typically of negligible thickness up to a maximum value of ~10% the transient cavity depth. The only exception was given by the model with a damaged friction coefficient of 0.35, where the rim collapse reached 50% the transient cavity depth. On terrestrial craters, a breccia lens is expected to be 1/2 to 1/3 the crater depth (e.g., Melosh 2011). As discussed above, these "deeper" craters may arise from not

having implemented dilatancy into the modeling. However, regardless the model assumptions, we noticed that (i) the depth mismatch between the modeled crater and the real impact structure reached up 13%, and (ii) the d/D ratio measured on Linné falls within the d/D trend inferred for lunar and Martian simple craters (Pike 1974, Watters et al. 2015). These observations seem to suggest that any rim collapse was not a very efficient mechanism during the formation of Linné crater, in comparison to the terrestrial case. This can arise from either the smaller Linné size with respect to terrestrial craters approaching the simple-to-complex transition, or differences in the near-surface characteristics. Therefore, the high-albedo deposit lining the crater floor and lower wall can possibly be fragmental material due to a nearly-vertical impact, rather than the inward collapse of the crater rim. The LROC NAC image of Linné highlighted indeed the presence of small-sized debris on the crater floor. Being of few meters the resolution of our models, our simulation can not follow the overall emplacement of this high-albedo deposit.

Some further considerations can be done if comparing the modeling results with other observational data, including the morphometric analysis of the crater. The slope and profile curvature maps computed on the topographic elevation of Linné showed the presence of three topographic steps along the inner crater wall (Figure 10). The first one, at +20 m above the pre-impact surface, can be associated to the transition from the structurally-uplifted rim to the ejecta blanket. The 200 m deep ring occurred together with the albedo variation, and likely represents the top area of the breccia lens. The ring at -100 m is a small mostly continuous feature along the crater wall highlighted by the morphometric analysis, but no impact-related product seemed associated to it. We suggest that this ring at -100 m might possibly occur at the interface between two different layers. Such layer may represent two lava flow units that emplaced in different geologic times or through different volcanic vents, and can be expected to possess an own specific rheology (Hiesinger et al. 2001). Independent measurements about the Linné morphology were made by Stickle et al. (2016) on LROC NAC images. These authors observed the presence of an outcrop along the crater wall, finding a thickness of 120 m (once corrected for the wall slope measured from the topographic profile). This value is in agreement with the morphological ring we extracted from the curvature profile map, and thus a layered stratigraphy can be a realistic description of the Linné impact site.

These observations about crater morphometry can be compared to the material displacement plots derived from our models (Figure 6, column on the left). At the smaller thickness values (50 and 100 m, Figures 6A and B), the upper layer is completely embedded within the basement material. Indeed, the basement is found at shallow depth, thus it is uplifted and overturned during crater formation, sandwiching the thin upper layer. In the 100 m case, a roughly 100 m thick breccia lens is observed on the crater floor, while it is nearly absent in the 50 m case, where the major fracturation occurs along the crater wall. At intermediate thicknesses (200 and 250 m, Figures 6C and D), the rim and the upper

wall are instead made up by the uplifted and overturned fractured layer. The lower crater wall is made up of fractured basement, while the floor is lined with material coming from the upper layer. It is worthy to note that, after crater formation, the interface between the two layers moved to a 100-150 m depth below the pre-impact surface. Indeed the crater rim and upper wall were formed by an outward and upward flow-field operating during the excavation stage, which originated a raised structure (e.g., Kenkmann et al. 2013, Melosh 1989). Finally, at higher thicknesses (300 and 400 m, Figures 6E and F), the interior of the final crater is made up by the only upper layer material. However, in the 300 m configuration, rim material slumped down and filled the crater wall and floor except for an exposed area at 300 m depth, whereas in the 400 m case, the opening cavity was not able to penetrate into the basement, and thus it entirely formed within the upper layer.

Our simulations seemed to suggest that the 100 m deep layer interface revealed by morphometric analysis can be explained if an intermediate thick upper layer (~200 m) is considered. Indeed, it is only in this model configuration that the boundary between the two layers developed at the measured depth. However, the configuration with an upper layer 100 m thick cannot be completely ruled out if further post-impact gravitational landslides occur and work to expose the crater rim and upper wall. Mass wasting can indeed expose the embedded layer, and at the same time produce debris flows that then cluster on the crater floor and shallow the final crater (improving the fit between model and topographic elevation profiles).

From the overall discussion presented here, we outlined that numerical modeling on both one homogeneous and double layered target can account for the truncated-cone shape of Linné, given the model assumptions (high impact velocity and no dilatancy) and uncertainties (accuracy within 10%). Evidences from morphometric data suggested that a complex stratigraphy at the Linné impact site is more reliable, and can have various interpretations among the evolutionary history of Mare Serenitatis. One first hypothesis (Figure 11A) relies on the idea that the two layers represent two compound mare units.

Mare units formed as a homogeneous layer of several individual lava flows flooded by the same volcanic vent. As noticed from the 3-layer configuration results, numerical simulations were not able to discriminate individual lava flows of similar composition. The upper fractured layer suggested by both simulations and morphometric analyzes represented therefore a multiple flow unit. Its proposed thickness of 100 to 200 m accounted for the topographic step measured on the crater wall at 100 m below the pre-impact surface, and is in agreement with previous estimates of mare thicknesses (e.g., Ono et al. 2009, Weider et al. 2010). According to Hiesinger et al. (2000) geologic map, the upper 100-200 m thick layer should correspond to S14 unit, where Linné is located. This unit, which is dated 3.49 Ga ago, is surrounded by several younger units, with ages ranging between 3.43 and 2.90 Ga ago. The closer unit emplaced before S14 is S10 (3.60 Ga), and it might represent the underlying consolidated layer modeled in the numerical simulations

(the basement). Both these units are the result of successive thin lava emplacements, possibly interleaved by regolith and/or volcanic ash deposits. The difference in the rheology, which was accounted in our numerical simulation as differences in the cohesion values, can be explained as variations in the magma compositions with time (Hiesinger et al. 2001). Alternatively, S10 unit did not undergo heavy space weathering since it was covered by unit S14 relatively shortly after its emplacement, while the younger S14 unit experienced stronger impact cratering and/or fracturing after cooling processes.
A double-layer stratigraphy at the Linné impact site can be either explained as one single volcanic event (Figure 11B). In fact, an inflated lava flow is generally made up of a competent core that is sheltered by a film of a chilled brittle and often fractured material. The outer shell developed fractures and joints because the higher cooling rate with respect to the inner core, and the exposition to space weathering. According to this scenario, unit S14 where Linné formed is at least 400 m thick (100-200 m of a weak shell above ≥200 m of lava core).

CONCLUSION

In this paper, we presented the study about Linné crater, a simple impact structure located in the northwestern edge of Mare Serenitatis. High-resolution images of the Lunar Reconnaissance Orbiter Camera highlighted that Linné is a 2.22 km diameter and 0.58 km deep crater characterized by a truncated-cone shape. It has long been used as proxy for simple craters since it is a pristine landform, as suggested by its sharp rim and high-reflectance ejecta. Therefore, it is valuable to better understand how the crater formed and in which impact conditions (e.g., projectile and target properties).
The analysis was performed by numerical modeling through iSALE shock physics code the impact event that formed the crater. We focused our investigation in testing the effects of target properties (material parameters and layering) on the final crater shape. The best-fit models were then constrained by comparing simulation results to observational data, including the representative mean topographic profile of Linné and morphometric measurements on the crater cavity including slope and profile curvature. These data highlighted the presence of three topographic steps along the inner crater wall, at the elevations of +20, -100 and -200 m. While the first and the last ring can be impact-related features associated to the transition from the structurally-uplifted rim to the ejecta blanket and the upper boundary of breccia lens on the crater floor, respectively, the ring at -100 m can possibly represent an interface between two different rheological layers.
When simulating the formation of Linné in one single homogeneous target, we obtained the higher variations in crater appearance when varying either the cohesive strength or friction coefficient for damaged material. We observed that craters forming in low cohesion targets (Yd0≤10 kPa) developed a conic shape, with a 15% d/D and 3° slope variations over three

orders of cohesion magnitude. On the other hand, crater forming in high cohesion targets (Yd0>10 kPa) are rather closer to a parabolic shape, with higher d/D ratio (up to 0.4) and higher inner crater slope (~63°). The implementation of a low friction coefficient (0.35) led to the formation of a breccia lens as thick as half the depth of the transient cavity.
The better agreement between models and topographic elevation of the crater was found by using a 1 MPa intact cohesive strength and a 10 kPa damaged cohesive strength. The final diameter resulted (2.24 ± 0.22) km. This specific model did not perfectly match the measured topographic profile, because it had a higher depth (9%), slope (13%), and aspect ratio d/D (8%), nevertheless such discrepancies can be explained by the model uncertainties (10%) and assumptions (high impact velocity and no dilatancy model).
In the double layer configuration, we introduced an upper fractured layer over a basement (with the material parameters set to the one layer best fit). We varied the upper layer thickness between 50 and 400 m, finding that the modeled craters are all truncated-cone shaped, with a variation of 12% in the d/D ratio and 15% in the inner crater slope, over the range of the thicknesses tested. The better agreement between models and the mean topographic profile was found with an upper layer thickness of 100 and 400 m. Even though the discrepancies between numerical simulations and crater topographic elevation can be explained by model uncertainties, the analysis of displaced material provided further details on the expected crater morphology. Only when considering intermediate thicknesses (~200 m) for the upper layer, the resulting crater had a clearly exposed interface between the two layers along its wall at 100 m below the pre-impact surface. Conversely, in the borderline cases of either thinner or larger thicknesses of the upper fractured layer, the crater wall was entirely made up by only one type of material that obscured, if present, any layering transition. However, the configuration with an upper layer 100 m thick can not be completely ruled out, if post-impact gravitational landslides occurred and worked to expose the crater rim and upper wall.
The layered stratigraphy suggested by this analysis can have two different interpretations. A first hypothesis suggested that these two layers are two mare (compound flow) units, where the upper one experienced stronger impact cratering and/or fracturing after cooling processes, and emplaced soon afterwards the lower one. The second hypothesis proposed that the two modeled layers represent the brittle shell over a competent core of a single volcanic inflated-like event.

ACKNOWLEDGMENTS

We gratefully acknowledge the developers of iSALE-2D/Chicxulub version (www.isale-code.de), including Gareth Collins, Kai Wünnemann, Dirk Elbeshausen, Boris Ivanov and Jay Melosh. Some plots in this work were created with the pySALEPlot tool written by Tom Davison.

The authors would also like to acknowledge M. Robinson and Harald Hiesinger for helpful discussion. The manuscript was significantly improved by the comments from G. Collins and V.L. Sharpton.
E.M. would like to acknowledge the University of Padova under the 2013 Junior Fellowship and INAF-Osservatorio Astronomico di Padova under grant 1.05.04.29.04 "BepiColombo" and 1.05.04.49.03 "JUICE".
This research was supported also by the Italian Space Agency (ASI) within the SIMBIOSYS Project (ASI-INAF agreement no. I/022/10/0)

REFERENCES

Amsden A.A., Ruppel H.M., and Hirt C.W. 1980. SALE: A simplified ALE Computer Program for Fluid Flows at all speeds. Los Alamos National Laboratories, Report LA–8095.

Anderson J.A., Sides S.C., Soltesz D.L., Sucharski T.L., and Becker K.J. 2004. Modernization of the Integrated Software for Imagers and Spectrometers. 35th Lunar and Planetary Science Conference (2004), #2039.

Artemieva N., Karp T., and Milkereit B. 2004. Investigating the lake bosumtwi impact structure: Insight from numerical modeling. Geochemistry Geophysics Geosystems 5, Q11016.

Atwood-Stone C. and McEwen A.S. 2013. Avalanche slope angles in low-gravity environments from active Martian sand dunes. Geophysical Research Letters 40, 2929-2934.

Baker M.K., Mazarico E., Neumann G.A., Zuber M.T., Haruyama J., and Smith D.E. 2016. A new lunar digital elevation model from the Lunar Orbiter Laser Altimeter and SELENE Terrain Camera. Icarus 273, 346-355.

Barlow N.G. 2004. Martian subsurface volatile concentrations as a function of time: Clues from layered ejecta craters, Geophysical Research Letters 31, L05703.

Bart G.D. and Melosh H.J. 2010. Impact into lunar regolith inhibits high-velocity ejection of large blocks. Journal of Geophysical Research 115, E08004.

Bart G.D., Nickerson R.D., Lawder M.T., and Melosh H.J. 2011. Global survey of lunar regolith depths from LROC images. Icarus 215, 485-490.

Basilevsky A.T., Kreslavsky M.A., Karachevtseva I.P, and Gusakova E.N. 2014. Morphometry of small impact craters in the Lunokhod-1 and Lunokhod-2 study areas. Planetary and Space Science 92, 77-87.

Basilevsky A.T., Abdrakhimov A.M., Head J.W., Pieters C.M., Wu Y., and Xiao L. 2015. Geologic characteristics of the Luna 17/Lunokhod 1 and Chang'E-3/Yutu landing sites, Northwest Mare Imbrium of theMoon. Planetary and Space Science 117, 385-400.

Beyer R.A. 2015. An introduction to the data and tools of planetary geomorphology. Geomorphology 240, 137-145.

Blewett D.T., Hawke B.R., and Lucey P.G. 2005. Lunar optical maturity investigations: A possible recent impact crater and a magnetic anomaly. Journal of Geophysical Research 110, E04015.

Bray V.J., Collins G.S., Morgan J.V., and Schenk P.M. 2008. The effect of target properties on crater morphology: Comparison of central peak craters on the Moon and Ganymede. Meteoritics & Planetary Science 43, 1979-1992.

Brett R. 1975. Thicknesses of some lunar mare basalt flows and ejecta blankets based on chemical kinetic data. Geochimica et Cosmochimica Acta 39, 1135-1141.

Bue B.D. and Stepinski T.K. 2007. Machine Detection of Martian Impact Craters From Digital Topography Data. IEEE Transactions on Geoscience and Remote Sensing 45, 265-274.

Burchell M.J. and Whitehorn L. 2003. Oblique incidence Hypervelocity impacts on rock. Mon Not R Astron 341, 192-198.

Carrier W.D., Olhoeft G.R., and Mendell W. 1991. Physical Properties of the Lunar Surface. In: G. Heiken, D. Vaniman, B.M. French (eds), Lunar Sourcebook, Cambridge University Press, 475-594.

Chapman C.R. and Jones K.L. 1977. Cratering and obliteration history of Mars. Annual Review of Earth and Planetary Sciences 5, 515-538.

Chappelow J.E. 2013. Simple impact crater shape determination from shadows. Meteoritics & Planetary Science 48, 1863-1872.

Chappelow, J.E. and Sharpton V.L. 2002. An improved shadow measurement technique for constraining the mrophometry of simple impact craters. Meteoritics & Planetary Science 37, 479-486.

Chyba C.F. 1991. Terrestrial mantle siderophiles and the lunar impact record. Icarus 92, 217-233.

Collins G.S. 2014. Numerical simulations of impact crater formation with dilatancy. Journal of Geophysical Research Planets 119, 2600-2619.

Collins G.S., Melosh H.J., and Ivanov B.A. 2004. Modeling damage and deformation in impact simulations. Meteoritics & Planetary Science 39, 217-231.

Collins G.S., Kenkmann T., Osinski G.R., and Wünnemann K. 2008. Mid–sized complex crater formation in mixed crystalline–sedimentary targets: Insight from modeling and observation. Meteoritics & Planetary Science 43, 1955-1977.

Collins G.S., Melosh H.J., and Wünnemann K. 2011a. Improvements to the ε-α porous compaction model for simulating impacts into high-porosity solar system objects. International Journal of Impact Engineering 38, 434-439.

Collins G.S., Elbeshausen D., Davison T.M., Robbins S.J., and Hynek B.M. 2011b. The size-frequency distribution of elliptical impact craters. Earth and Planetary Science Letters 310, 1-8.

Collins, G.S., Melosh H.J., and Osinski G.R. 2012. The impact-cratering process. Elements 8: 25-30.

Costes N.C. and Mitchel J.K., 1970. Apollo 11 soil mechanics investigation. Proceedings of the Apollo 11 Lunar Science Conference 3, 2025-2044.

Craddock R.A. and Howard A.D. 2000. Simulated degradation of lunar impact craters and a new method for age dating farside mare deposits. Journal of Geophysical Research 105, 20,387-20,401.

Craddock R.A., Maxwell T.A., and Howard A.D. 1997. Crater morphometry and modification in the Sinus Sabaeus and Margaritifer Sinus regions of Mars. Journal of Geophysical Research 102, 13,321–13,340.

Daubar I.J., Atwood-Stone C., Byrne S., McEwen A.S., and Russell P.S. 2014. The morphology of small fresh craters on Mars and the Moon. Journal of Geophysical Research Planets 119, 2620-2639.

Davis P.A. and Soderblom L.A. 1984. Modeling crater topography and albedo from monoscopic Viking Orbiter images: 1. Methodology. Journal of Geophysical Research 89, 9449-9457.

De Hon R.A. 1979. Thickness of western mare basalts. Proceedings of Lunar and Planetary Science Conference 10th, 2935-2955.

Denevi B.W., Koeber S.D., Robinson M.S., Garry W.B., Hawke B.R., Tran T.N., Lawrence S.J., Keszthelyi L.P., Barnouin O.S., Ernst C.M., and Tornabene L.L. 2012. Physical constraints on impact melt properties from Lunar Reconnaissance Orbiter Camera images. Icarus 219, 665–675.

Drucker D.C. and Prager W. 1952. Soil mechanics and plastic analysis or limit design. Quaterly of Applied Mathematics 10, 157-165.

Ernst C.M., Murchie S.L., Barnouin O.S., Robinson M.S., Denevi B.W., Blewett D.T., Head J.W., Izenberg N.R., Solomon S.C., and Roberts J.H. 2010. Exposure of spectrally distinct material by impact craters on Mercury: Implications for global stratigraphy. Icarus 209, 201-223.

Evans I.S. 1998. What do terrain statistics really mean? In: S.N. Lane, K.S. Richards, J.H. Chandler (eds), Landform monitoring, modelling and analysis, Wiley Publications, 119-138.

Fa W., Zhu M.-H., Liu T., and Plescia J.B. 2015. Regolith stratigraphy at the Chang'E-3 landing site as seen by lunar penetrating radar. Geophysical Research Letters 42, 10,179-10,187.

Fassett C.I. and Thomson B.J. 2014. Crater degradation on the lunar maria: Topographic diffusion and the rate of erosion on the moon. Journal of Geophysical Research: Planets 119, 2255-2271.

Fassett C.I., Head J.W., Kadish S.J., Mazarico E., Neumann G.A., Smith D.E., and Zuber M.T. 2012. Lunar impact basins: Stratigraphy, sequence and ages from superposed impact crater populations measured from Lunar Laser Altimeter (LOLA) data. Journal of Geophysical Research 117, E00H06.

Gaddis L., Anderson J., Becker K., Becker T., Cook D., Edwards K., Eliason E., Hare T., Kieffer H., Lee E.M., Mathews J., Soderblom L., Sucharski T., Torson J., McEwen A., and Robinson M. 1997. An Overview of the Integrated Software for Imaging Spectrometers (ISIS). 28th Lunar and Planetary Science Conference (1997), #387.

Garvin J.B. and Frawley J.J. 1998. Geometric properties of Martian impact craters: Preliminary results from the Mars Orbiter Laser Altimeter. Geophysical Research Letters 25, 4405-4408.

Garvin J.B., Sakimoto S.E.H., Frawley J.J., and Schnetzler C. 2000. North polar region craterforms on Mars: Geometric characteristics from the Mars Orbiter Laser Altimeter. Icarus 144, 329-352.

Garvin J.B., Robinson M.S., Frawley J., Tran T., Mazarico E., and Neumann G. 2011. Linne: simple lunar mare crater geometry from LRO observations. 42nd Lunar and Planetary Science Conference (2011), #2063.

Gault D.E. 1973. Displaced mass, depth, diameter, and effects of oblique trajectories for impact craters formed in dense crystalline rocks. The Moon 6, 32-44.

Gault D.E. and Wedekind, J.A. 1978. Experimental studies of oblique impact. Proceedings of the 9th Lunar Planetary Science Conference, 3843-3875.

Grieve R.A.F. 1987. Terrestrial Impact Structures. Annual Review of Earth and Planetary Sciences 15, 245-270.

Hartmann W.K. and Wood C.A. 1971. Moon: origin and evolution of multi-ring basins. The Moon 3, 3-78.

Head J.W. 1979. Serenitatis multi-ringed basin: regional geology and basin ring interpretation. The Moon and the Planets 21, 439-462.

Herrick R.R. and Sharpton V.L. 2000. Implications from stereo-derived topography of Venusian impact craters. Journal of Geophysical Research 105, 20,245-20,262.

Hiesinger H. and Head J.W. 2006. New views of Lunar geoscience: an introduction and overview. In: Reviews in Mineralogy & Geochemistry 60, 1.81.

Hiesinger H., Jaumann R., Neukum G., and Head J.W. 2000. Ages of mare basalts on the lunar nearside. Journal of Geophysical Research 105, 29,239-29,275.

Hiesinger H., Head J.W., and Wolf U. 2001. Lunar mare basalts: Mineralogical variations with time. 32nd Lunar and Planetary Science Conference (2001), #1826.

Hiesinger H., Head J.W., Wolf U., Jaumann R., and Neukum G. 2002. Lunar mare basalt flow: thicknesses determined from crater size-frequency distributions. Geophysical Research Letters 29, 89,1-4.

Holsapple K.A. 1993. The scaling of impact processes in planetary sciences. Annual Review of Earth and Planetary Sciences 21, 333-373.

Holsapple K.A. and Housen 2007. A crater and its ejecta: An interpretation of Deep Impact. Icarus 187, 345-356.

Holt J.W., Safaeinili A., Plaut J.J., Head J.W., Phillips R.J., Seu R., Kempf S.D., Choudhary P, Young D.A., Putzig N.E., Biccari D., and Gim Y. 2008. Radar Soounding Evidence for Buried Glaciers in the Southern Mid-Latitudes of Mars. Science 322, 1235-1238.

Housen K.R. and Wilkening L.L. 1982. Regoliths on small bodies in the Solar System. Annual Review of Earth and Planetary Sciences 10, 355-376.

Housen K.R. and Holsapple K.A. 2003. Impact cratering on porous asteroids. Icarus 163, 102-119.

Howard K.A., Head, J.W., and Swann G.A. 1972. Geology of Hadley Rille. Proceedings of the 3th Lunar Science Conference, 1-14.

Humm D.C., Tschimmel M., Brylow S.M., Mahanti P., Tran T.N., Braden S.E., Wiseman S., Danton J., Eliason E.M., and Robinson M.S. 2015. Flight Calibration of the LROC Narrow Angle Camera. Space Science Reviews 200, 431-473.

Ishiyama K., Kumamoto A., Ono T., Yamaguchi Y., Haruyama J., Ohtake M., Katoh Y., Terada N., and Oshigami S. 2013. Estimation of the permittivity and porosity of th lunar uppermost basalt layer based on observations of impact craters by SELENE. Journal of Geophysical Research: Planets 118, 1453-1467.

Ivanov B.A., Deniem D., and Neukum G. 1997. Implementation of dynamic strength models into 2D hydrocodes: Application for atmospheric breakup and impact cratering. International Journal of Impact Engineering 20, 411-430.

Jaffe L.D. 1969a. Strength-Density Relations in Particulate Silicates of Complex Shape and Their Possible Lunar Significance. Science 165, 1121-1123.

Jaffe L.D. 1969b. Recent observations of the Moon by spacecraft. Space Science Reviews 9, 491-609.

Jaffe L.D. 1973. Shear strength of lunar soil from Oceanus Procellarum. The Moon 8, 58-72.

Johnson W.E. and Anderson C.E. 1987. History and application of hydrocodes in hypervelocity impact. Internation Journal of Impact Engineering 5, 423-439.

Kenkman, T., Collins, G.S., and Wünnemann, K 2013. The modification stage of crater formation. In: G.R. Osinski and E. Pierazzo (eds), Impact Cratering: Processes and Products, Blackwell Publ., 60-75.

Kiefer W.S., Macke R.J., Britt D.T., Irving A.J., and Consolomagno G.J. 2012. The density and porosity of lunar rocks. Geophysical Research Letters 39, L07201.

Kreslavsky M.A. and Head J.W. 2000. Kilometer-scale roughness of Mars: Results from MOLA data analysis. Journal of Geophysical Research 105, 26,695–26,712.

Kreslavsky M.A. and Head J.W. 2016. The steepest slopes on the Moon from Lunar Orbiter Laser Altimeter (LOLA) Data: Spatial Distribution and Correlation with Geologic features. Icarus 273, 329-336.

Love S.G., Brownlee D.E., King N.L., and Hörz F. 1994. Morphology of meteoroid and debris impact craters formed in soft metal targets on the LDEF satellite. Interntional Journal of Impact Engineering 16, 405-418.

Lundborg N. 1968. Strength of rock-like materials. International Journal of Rock Mechanics and Mining Sciences 5, 427-454.

Mahanti P., Robinson M.S., Humm D.C., and Stopar J.D. 2014. A standardized approach for quantitative characterization of impact crater topography. Icarus 241, 114-129.

Marchi S., Mottola S., Cremonese G., Massironi M., and Martellato E. 2009. A new chronology for the Moon and Mercury. The Astronomical Journal 137, 4936-4948.

Mazarico E., Lemoine F.G., Han S.-C-, and Smith D.E. 2010. GLGM-3: A degree-150 lunar gravity model from the historical tracking data of NASA Moon orbiters. Journal of Geophysical Research 115, E05001.

Melosh H.J. 1979. Acoustic fluidization: a new geologic process? Journal of Geophysical Research 84, 7513-7520.

Melosh H.J. 1989. Impact cratering: A geologic process. New York: Oxford University Press. 245 p.

Melosh H.J. 2011. Planetary surface processes. Cambridge University Press, 500 p.

Melosh H.J. and Ivanov B.A. 1999. Impact crater collapse. Annual Review of Earth and Planetary Sciences 27, 385-415.

Melosh H.J., Ryan E.V., and Asphaug E. 1992. Dynamic Fragmentation in Impact: Hydrocode Simulation of Laboratory Impacts. Journal of Geophysical Research 97, 14,735-14,759.

Michikami T., Hagermann A., Miyamoto H., Miura S., Haruyama J., and Lykawka P.S. 2004. Impact cratering experiments in brittle targets with variable thickness: Implicatins for deep pit craters on Mars. Planetary and Space Science 96, 71-80.

Neish C.D., Madden J., Carter L.M., Hawke B.R., Giguere T., Bray V.J., Osinski G.R., and Cahill J.T.S. 2014. Global distribution of lunar impact melt flows. Icarus 239, 105-117.

Nettles J.W., Staid M, Besse S., Boardman J., Clark R.N., Dhingra D., Isaacson P., Klima R., Kramer G., Pieters C.M., and Taylor L.A. 2011. Optical maturity variation in lunar spectra as measured by Moon Mineralogy Mapper data. Journal of Geophysical Research 116, E00G17

Neukum G. and Horn P. 1976. Effects of lava flows on lunar crater populations. The Moon 15, 205-222.

Neukum G., König B., and Arkani–Hamed J. 1975. A study of lunar impact crater size–distributions. The Moon 12, 201-229.

Nowicki S.A. and Christensen P.R. 2007. Rock abundance on Mars from the Thermal Emission Spectrometer, Journal of Geophysical Research, 112, E05007.

O'Keefe J.D. and Ahrens T.J. 1993. Planetary Cratering Mechanics. Journal of Geophysical Research 98, 17,011-17,028.

O'Keefe J.D., Stewart S.T., Lainhart M.E., and Ahrens T.J. 2001. Damage and rock-volatile mixture effects on impact crater formation, International Journal of Impact Engineering 26, 543-553.

Ono T., Kumamoto A., Nakagawa H., Yamaguchi Y., Oshigami S., Yamaji A., Kobayashi T., Kasahara Y., and Oya H. 2009. Lunar Radar Sounder observations of subsurface layers under the Nearside maria of the Moon. Science 323, 909-912.

Oshigami S., Yamaguchi Y., Yamaji A., Ono T., Kumamoto A., Kobayashi T., and Nakagawa H. 2009. Distribution of the subsurface reflectors of the western nearside maria observed from Kaguya with Lunar Radar Sounder. Geophysical Research Letters 36, L18202.

Oshigami S., Okuno S., Yamaguchi Y., Ohtake M., Haruyama J., Kobayashi T., Kumamoto A., and Ono T. 2012. The layered structure of lunar maria: Identification of the HF-radar reflector in Mare Serenitatis using multiband optical images. Icarus 218, 506-512.

Oshigami S., Watanabe S., Yamaguchi Y., Yamaji A., Kobayashi T., Kumamoto A., Ishiyama K., and Ono T. 2014. Mare volcanism: reinterpretation based on Kaguya Lunar Radar Sounder data. Journal of Geophysical Research: Planets 119, 1037-1045.

Pierazzo E. and Chyba C.F. 1999. Amino acid survival in large cometary impacts. Meteoritics & Planetary Science 34, 909-918.

Pierazzo E. and Melosh H.J. 2000a. Understanding oblique impacts from experiments, observations, and modeling. Annual Review of Earth and Planetary Sciences 28, 141-167.

Pierazzo E. and Melosh H.J. 2000b. Melt Production in Oblique Impacts. Icarus 145, 252-261.

Pierazzo E., Artemieva, N.A., and Ivanov, B.A., 2005, Starting conditions for hydrothermal systems underneath Martian craters: Hydrocode modeling. In T. Kenkmann, F. Hörz, A. Deutsch (eds)., Large meteorite impacts III: Geological Society of America Special Paper 384, 443-457.

Pierazzo E., Artemieva N., Asphaug E., Baldwin E.C., Cazamias J., Coker R., Collins G.S., Crawford D.A., Davison T., Elbeshausen D., Holsapple K.A., Housen K.R.,

Korycansky D.G., and Wünnemann K. 2008. Validation of numerical codes for impact and explosion cratering: Impacts on strengthless and metal targets. Meteoritics & Planetary Science 43, 1917-1938.

Pike R.J. 1974. Depth/diameter relations of fresh lunar craters – Revision from spacecraft data. Geophysical Research Letters 1, 291-294.

Pike R.J. 1980. Control of crater morphology by gravity and target type—Mars, Earth, Moon. Proceedings of the 11th Lunar and Planetary Science Conference, 2159-2189.

Plaut J.J., Picardi G., Safaeinili A., Ivanov A.B., Milkovich S.M., Cicchetti A., Kofman W., Mouginot J., Farrell W.M., Phillips R.J., Clifford S.M., Frigeri A., Orosei R., Federico C., Williams I.P., Gurnett D.A., Nielsen E., Hagfors T., Heggy E., Stofan E.R., Plettemeier D., Watters T.R., Leuschen C.J., and Edenhofer P. 2007. Subsurface Radar Sounding of the South Polar Layered Deposits of Mars. Science 316, 92-95.

Plescia J.B. and Cintala M.J. 2012. Impact melt in small lunar highland craters. Journal of Geophysical Research 117, E00H12.

Pommerol A., Kofman W., Audouard J., Grima C., Beck P., Mouginot J., Herique A., Kumamoto A., Kobayashi T., and Ono T. 2010. Detectability of subsurface interfaces in lunar maria by the LRS/SELENE sounding radar: Influence of mineralogical composition. Geophysical Research Letters 37, L03201.

Quaide W.L. and Oberbeck V.R. 1968. Thickness determinations of the lunar surface layer from lunar impact craters. Journal of Geophysical Research 73, 5247.5270.

Reimold W.U., Brandt D., and Koeberl C. 1998. Detailed structural analysis of the rim of a large, complex impact crater: Bosumtwi crater, Ghana. Geology 26, 543-546.

Robinson M.S., Brylow S.M., Tschimmel M., Humm D., Lawrence S.J., Thomas P.C., Denevi B.W., Bowman-Cisneros E., Zerr J., Ravine M.A., Caplinger M.A., Ghaemi F.T., Schaffner J.A., Malin M.C., Mahanti P., Bartels A., Anderson J., Tran T.N., Eliason E.M., McEwen A.S., Turtle E., Jolliff B.L., and Hiesinger H. 2010. Lunar Reconnaissance Orbiter Camera (LROC) Instrument Overview. Space Sceince Reviews 150, 81-124.

Robinson M.S., Ashley J.W., Boyd A.K., Wagner R.V., Speyerer E.J., Hawke B.R., Hiesinger H., and van der Bogert C.H. 2012. Confirmation of sublunear voids and thin layering in mare deposits. Planetary and Space Science 69, 18-27.

Rosenburg M.A., Aharonson O., Head J.W., Kreslvsky M.A., Mazarico E., Neumann G.A., Smith D.E., Torrence M.H., and Zuber M.T. 2011. Global surface slopes and roughness of the Moon from the Lunar Orbiter Laser Altimeter. Journal of Geophysical Research 116, E02001.

Salamunićcar G., Lončarić S., and Mazarico E. 2012. LU60645GT and MA132843GT catalogues of Lunar and Martian impact craters developed using a Crater Shape-

based interpolation crater detection algorithm for topography data. Planetary and Space Science 60, 236-247.

Schaber G.G. 1973a. Lava flows in Mare Imbrium: Geologic evaluation from Apollo orbital photography. Proceedings of the 4th Lunar Science Conference, 73-92.

Schaber G.G. 1973b. Eratosthenian Volcanism in Mare Imbrium: Source of Youngest Flows. In: Apollo 17: Preliminary Science Report. NASA SP-330, 30,17-30,25.

Schultz R.A 1995. Limits on Strength and Deformation Properties of Jointed Basaltic Rock Masses. Rock Mechanics and Rock Engineering 28, 1-15.

Schultz R.A. 1996. Effect of impact angle on vaporization. Journal of Geophysical Research 101, 21,117-21,136.

Schultz R.A. 2002. Stability of rock slopes in Valles Marineris, Mars. Geophysical Research Letters 29, 1932.

Senft L.E. and Stewart S.T. 2007. Modeling impact cratering in layered surfaces. Journal of Geophysical Research 112, E11002.

Sharpton 2014. Outcrops on lunar crater rims: Implications for rim construction mechanisms, ejecta volumes and excavation depths. Journal of Geophysical Research 119, 154-168.

Sharpton V.L., Krochuk R.V., and Herrick R.R. 2013. Characterization and morphological reconstruction of the Terny impact structure, central Ukraine. Meteoritics & Planetary Science 48, 806-818.

Shkuratov Y.G. and Bondarenko N.V., 2001. Regolith Layer Thickness Mapping of the Moon by Radar and Optical Data. Icarus 149, 329-338.

Smith D:E., Zuber M.T., Neumann G.A., Lemoine F.G., Mazarico E., Torrence M.H., McGarry J.F., Rowlands D.D., Head J.W., Duxbury T.H., Aharonson O., Lucey P.G., Robinson M.S., Barnouin O.S., Cavanaugh J.F., Sun X., Liiva P., Mao D.-D., Smith J.C., and Bartels A.E. 2010. Initial observations from the Lunar Orbiter Laser Altimeter (LOLA). Geophysical Research Letters 37, L18204.

Spohn T., Konrad W., Breuer D., and Ziethe R. 2001. The Longevity of Lunar Volcanism: Implications of Thermal Evolution Calculations with 2D and 3D Mantle Convection Models. Icarus 149, 54-65.

Spudis P.D., Wilhelms D.E., and Robinson M.S. 2011. The Sculptured Hills of the Taurus Highlands: Implications for the relative age of Serenitatis, basin chronologies and the cratering history of the Moon. Journal of Geophysical Research 116, E00H03.

Stickle A.M., Patterson G.W., Cahill J.T.S., and Bussey D.B.J. 2016. Mini-RF and LROC observations of mare crater layering relationships. Icarus 273, 224-236.

Stöffler D., Ryder G., Ivanov B.A., Artemieva N.A., Cintala M.J., and Grieve R.A.F. 2006. Cratering History and Lunar Chronology. In: Reviews in Mineralogy & Geochemistry 60, 519-596.

Stopar J.D., Hawke B.R., Robinson M.S., Denevi B.W., Giguere T.A., and Koeber S.D. 2014 Occurrence and mechanisms of impact melt emplacement at small lunar craters. Icarus 243, 337-357.

Tran T., Rosiek M.R., Beyer R.A., Mattson S., Howington-Kraus E., Robinson M.S., Archinal B.A., Edmundson K., Harbour D., Anderson E., and the LROC Science Team 2010. Generating digital terrain models using LROC NAC images. ASPRS/CaGIS 2010.

Watters W.A., Geiger L.M., Fendrock M., and Gibson R. 2015. Morphometry of small recent impact craters on Mars: Size and terrain dependence, short-term modification. Journal of Geophysical Research Planets 120, 226-254.

Weider S.Z., Crawford I.A., and Joy K.H. 2010. Individual lava flow thicknesses in Oceanus Procellarum and Mare Serenitatis determined from Clementine multispectral data. Icarus 209, 323-336.

Whitaker E.A. 1972. Mare Imbrium Lava Flows and Their Relationship to Color Boundaries. In: Apollo 15: Preliminary Science Report. NASA Special Publication 289, 83-84.

Wilhelms D.E., McCauley J.F., and Trask N.J. 1987. The geologic history of the Moon. USGS Report 1348, 302 p.

Wünnemann K. and Ivanov B.A. 2003. Numerical modelling of the impact crater depth-diameter dependence in an acoustically fluidized target. Planetary and Space Science 51, 831-845.

Wünnemann K., Collins G.S., and Melosh H.J. 2006. A strain–based porosity model for use in hydrocode simulations of impacts and implications for transient crater growth in porous targets. Icarus 180, 514-527.

Wünnemann K., Collins G.S., and Osinski G.R. 2008. Numerical modelling of impact melt production in porous rock. Earth and Planetary Science Letters 269, 530-539.

Wünnemann K., Nowka D., Collins G.S., Elbeshausen D., and Bierhaus M. 2011. Scaling of impact crater formation on planetary surfaces – insights from numerical modeling. Proceedings of the 11th Hypervelocity Impact Symposium, 16 p.

Xiao Z., Zeng Z., Ding N., and Molaro J. 2013. Mass wasting features on the Moon – how active is the lunar surface? Earth and Planetary Science Letters 376, 1-11.

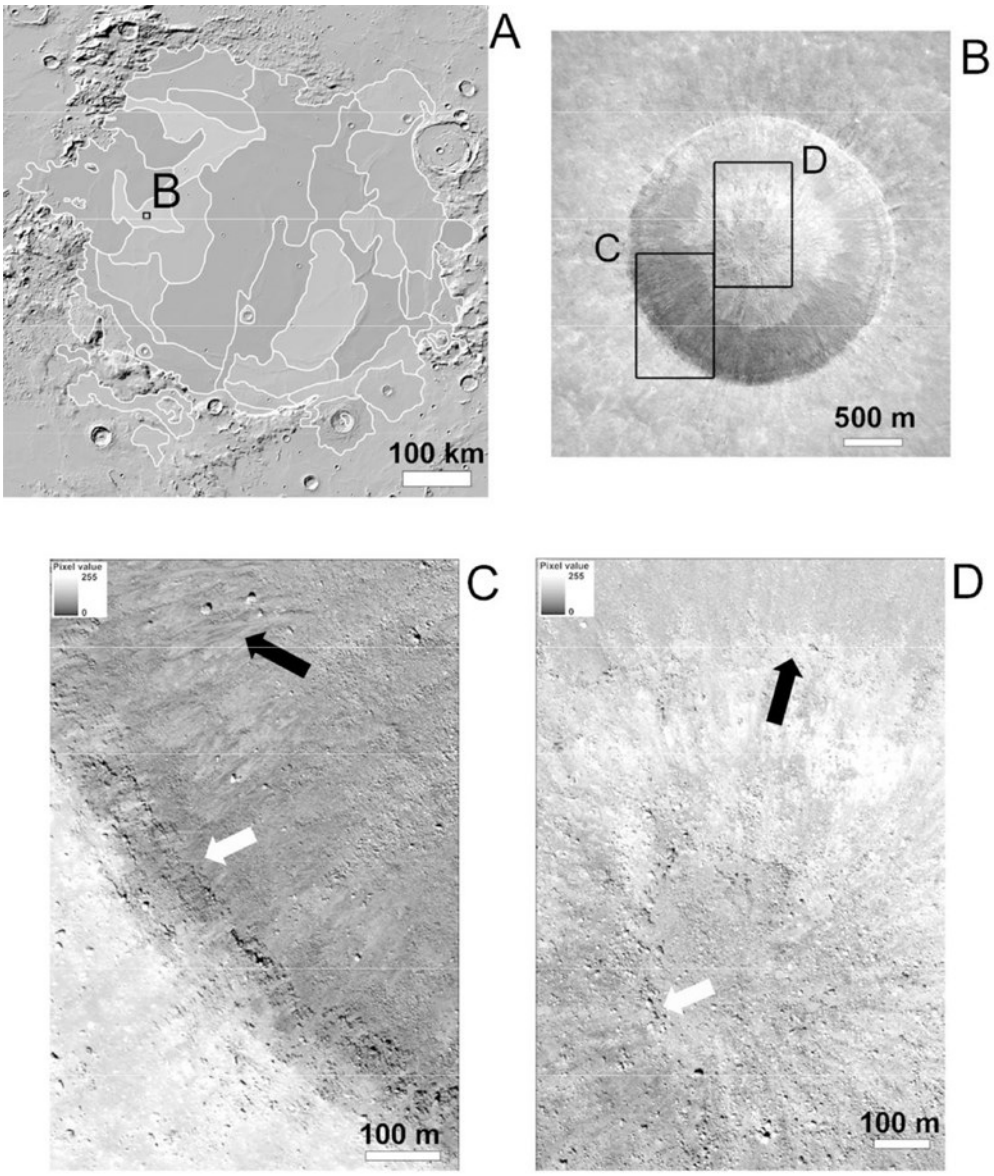

Figure 1. A) Map of Serenitatis basin, subdivided into the spectral units classified by Hiesinger et al. (2000). B) LROC NAC DTM derived from the orthorectified images M139829261 L/R and M139836046 L/R. It clearly shows the difference in albedo characterizing the crater floor. (http://lroc.sese.asu.edu/posts/305; credits: NASA/GSFC/Arizona State University). C) Detail of the rim of Linné; the white arrow outlines topographic uplift-ejecta transition outcrops, while the black arrow indicates impact melt patches; D) Detail of the central area of the crater, including the floor with its debris flow deposit (white arrow), and lower crater wall where the albedo variation occurs (black arrow); credits: NASA/GSFC/Arizona State University.

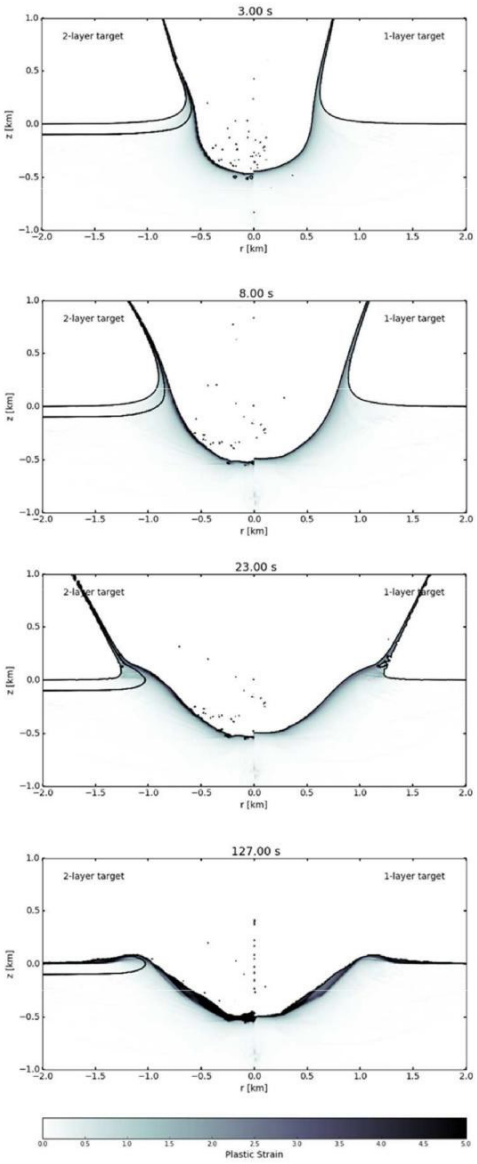

Figure 2. The crater-forming process for two Linné sized impact into (right) one layer, and (left) two layer target. Each model represents the best fit derived for the two target configurations (1 layer: 38 m radius projectile and Yd=10 kPa; 2 layers: 40 m radius projectile and 100 m thick upper crust; cf. Table 1 for further details).

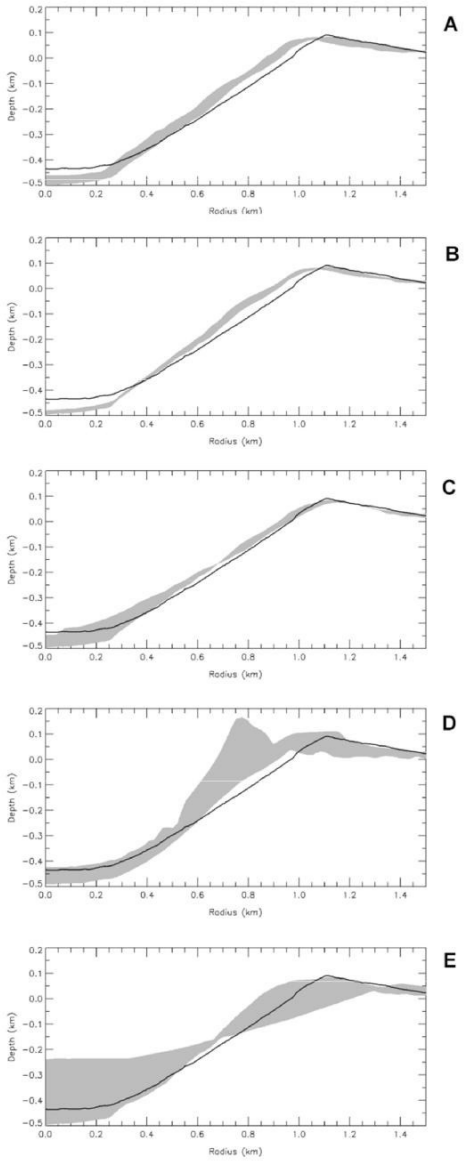

Figure 3. Plots show the results of numerical modeling of the one layer configuration, spanning different material properties: A) intact cohesive strength, B) intact friction coefficient, C) and D) damaged cohesive strength, and E) damaged friction coefficient. The simulated craters obtained by testing different values of each material parameter are represented as a shadowed area. The representative mean topographic profile of Linné is also given (black line).

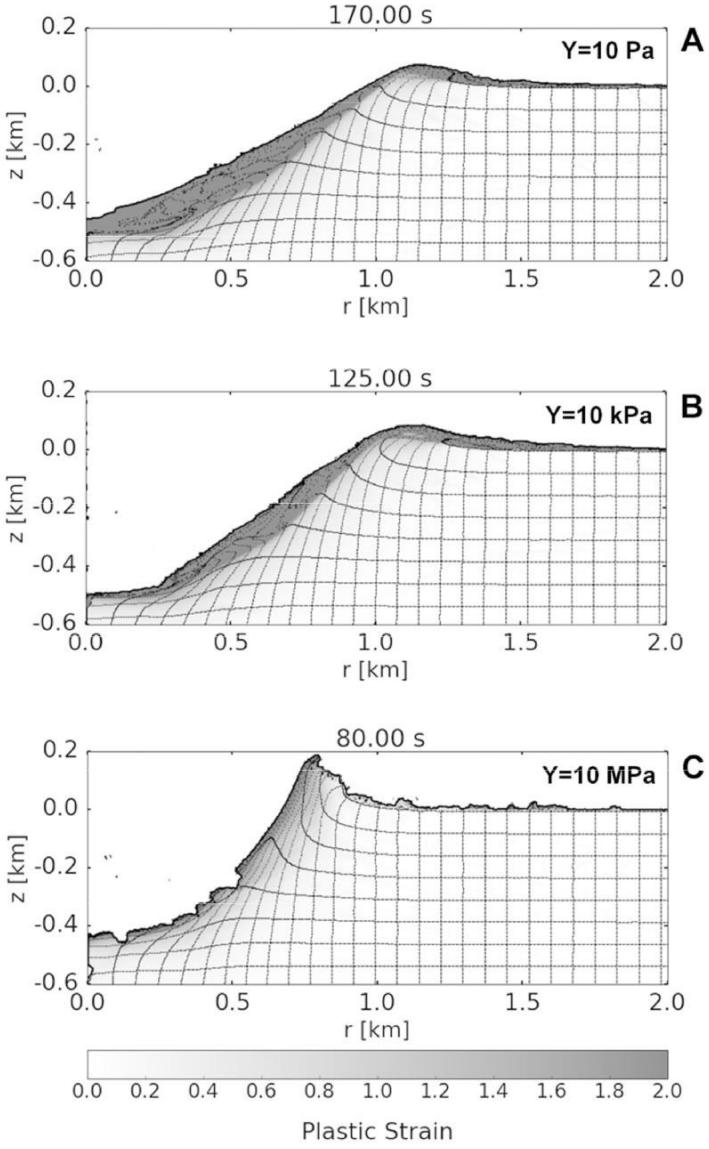

Figure 4. Accumulated plastic strain distribution (on a gray scale) overlaid by a Lagrangian grid for the 1 layer configuration, with varying damaged cohesive strengths: A) 10 Pa, B) 10 kPa, and C) 1 MPa.

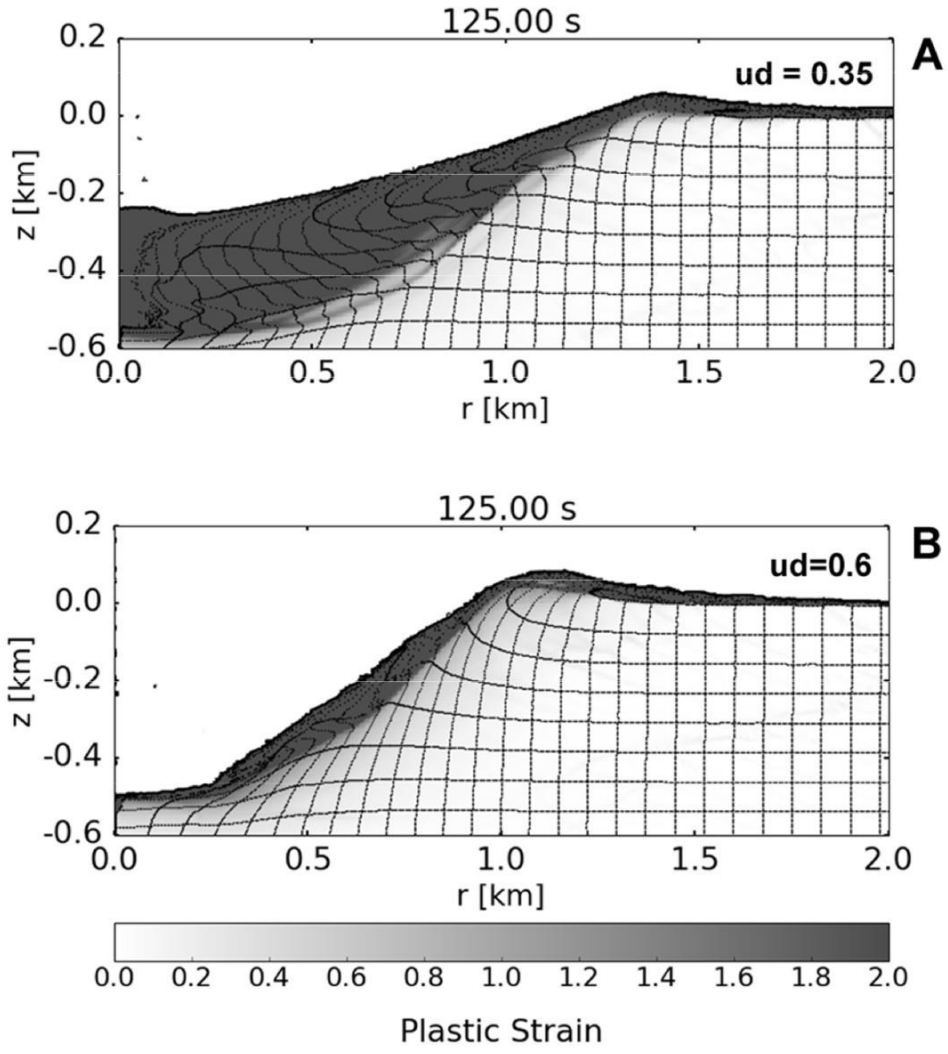

Figure 5. Accumulated plastic strain distribution (on a gray scale) overlaid by a Lagrangian grid for the 1 layer configuration, with varying damaged friction coefficient: A) 0.35, B) 0.6.

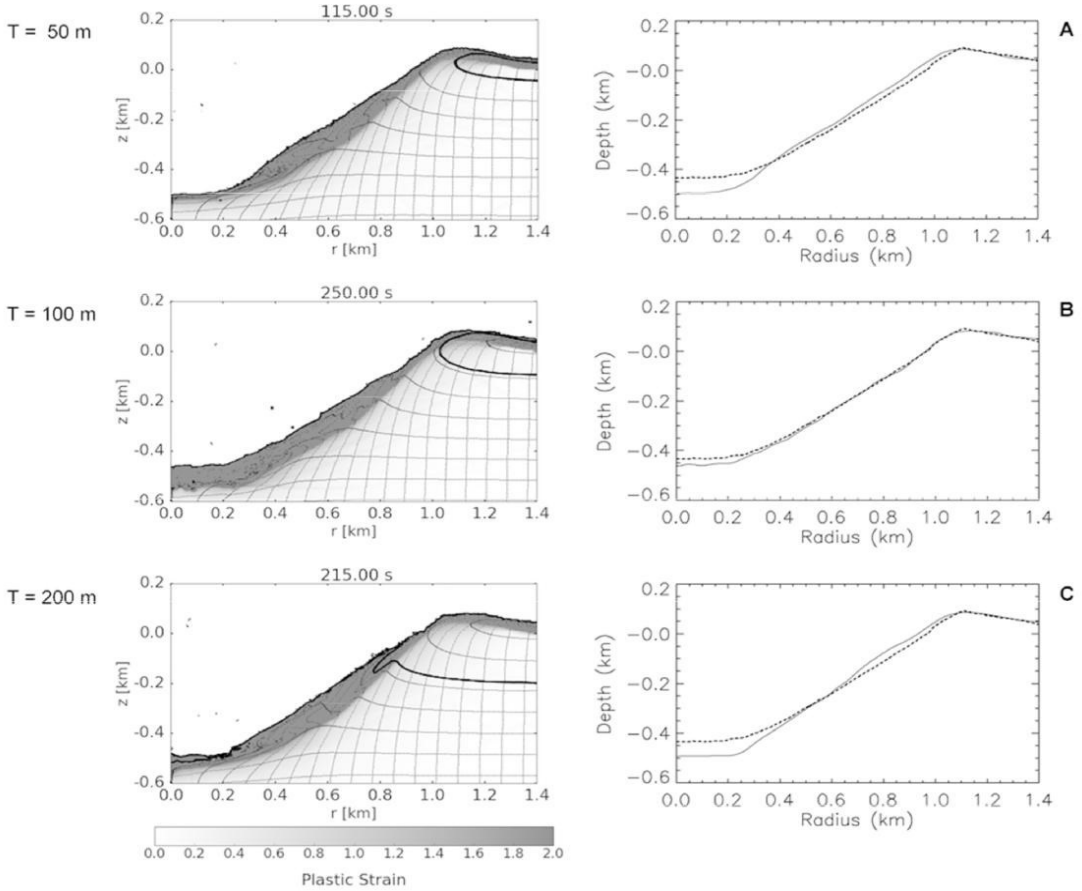

Figure 6. The results of numerical modeling derived for a Linné sized impact into the two layer configuration, where different upper layer thicknesses are considered; A) 50 m, B) 100 m, C) 200 m, D) 250 m, E) 300 m, and F) 400 m. In the left column, plots show the accumulated plastic strain distribution (on a gray scale) overlaid by a Lagrangian grid. In the right column, simulated crater profiles (continuous line) are compared to the mean topographic elevation of Linné (dotted line).

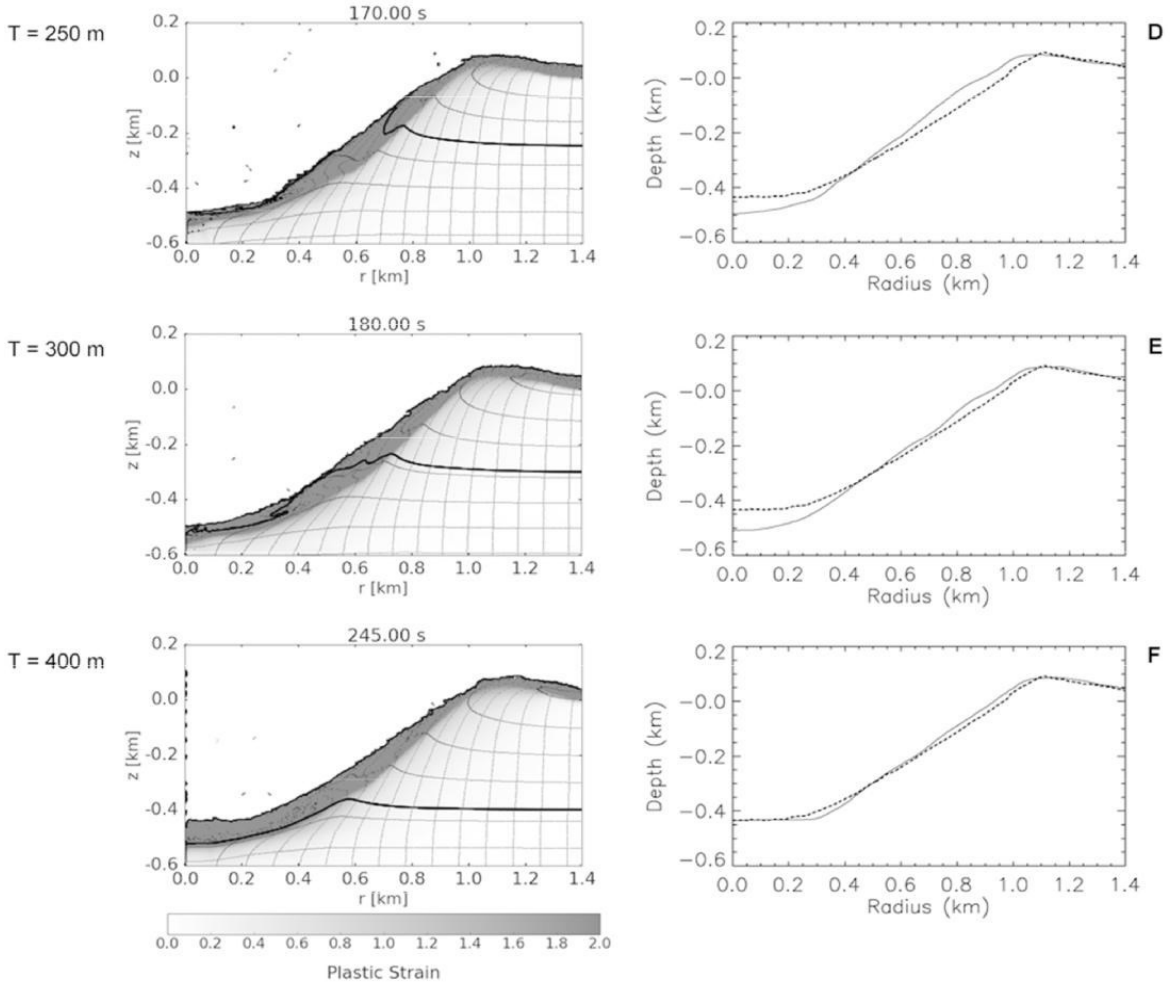

Figure 7. Final snapshot of the 3-layer model of Linné, where the semi-infinite target is made up by 100 m of fractured basalt on top of 100 m intermediate layer, which in turn overlays the basaltic basement. The left panel shows the total plastic strain (on a gray scale) that was accumulated during the passage of the shock wave and subsequent crater formation. The right panel of each plot represents the material overdrawn by a Lagrangian grid.

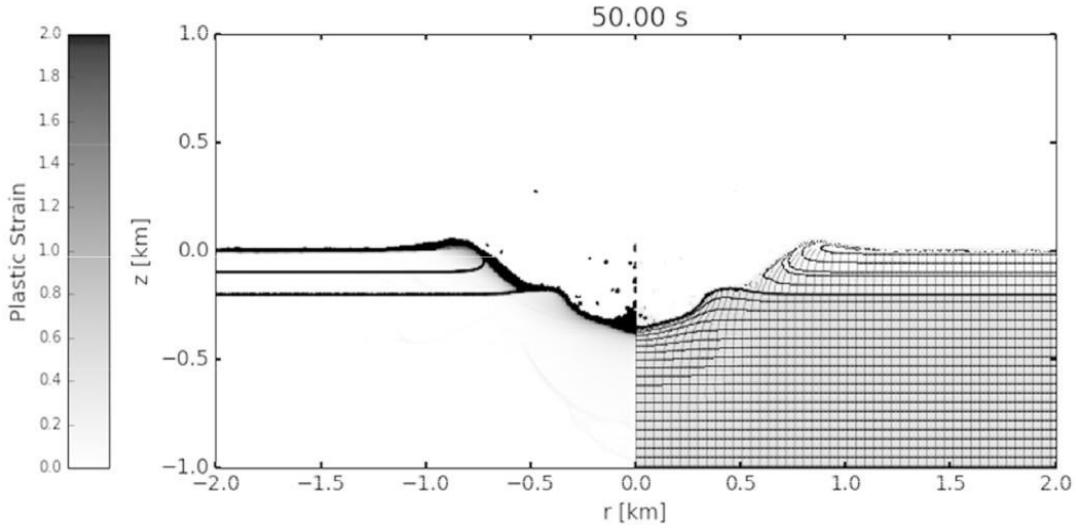

Figure 8. Maps of (A) topographic elevation, (B) slope, and (C) profile curvature.

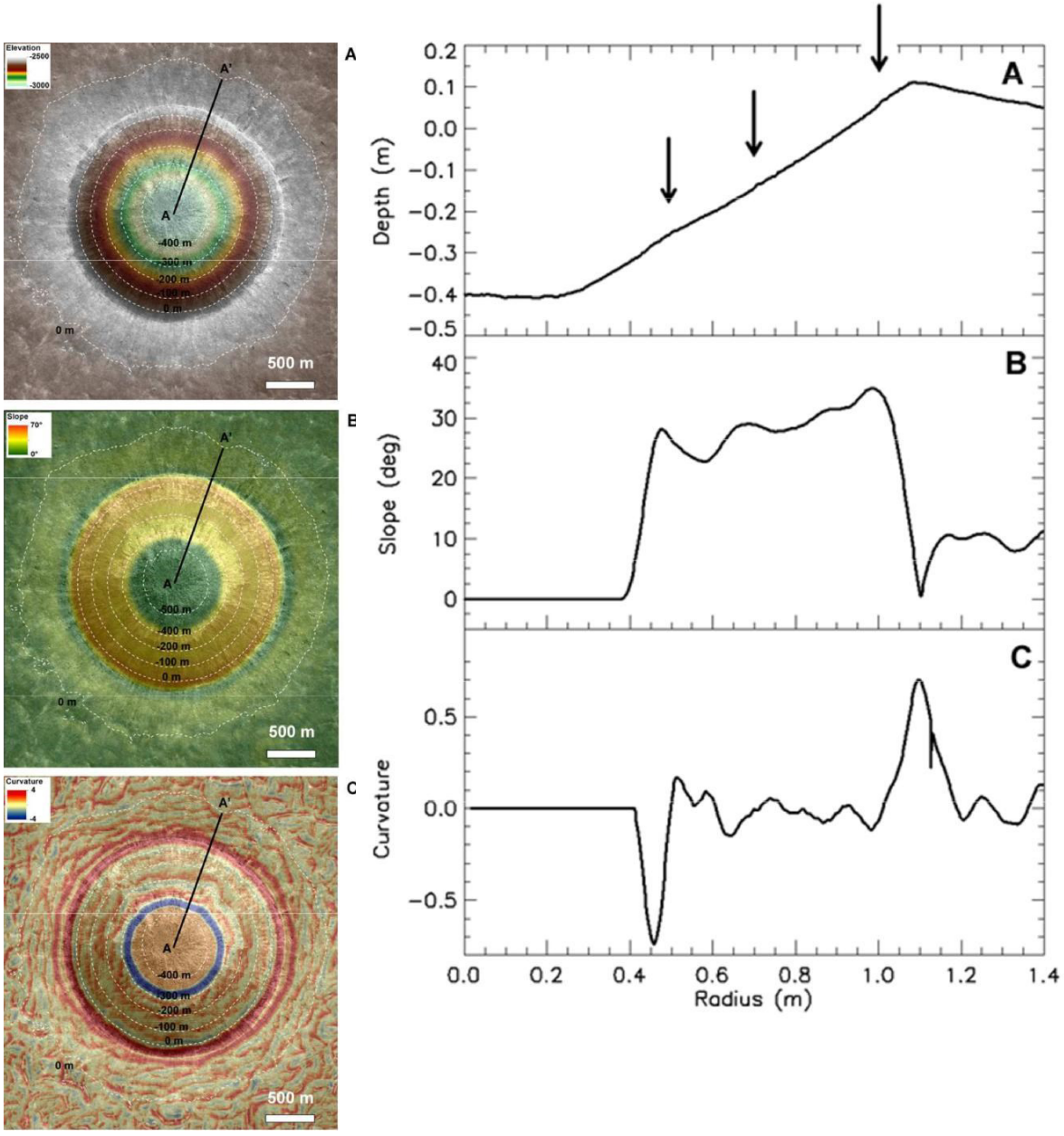

Figure 9. Profiles of (A) topographic elevation, (B) slope, and (C) profile curvature. Profiles are taken along the line AA' shown in Figure 8. The arrows indicate the corresponding position along the topographic profile where changes in both slope and profile curvature occur.

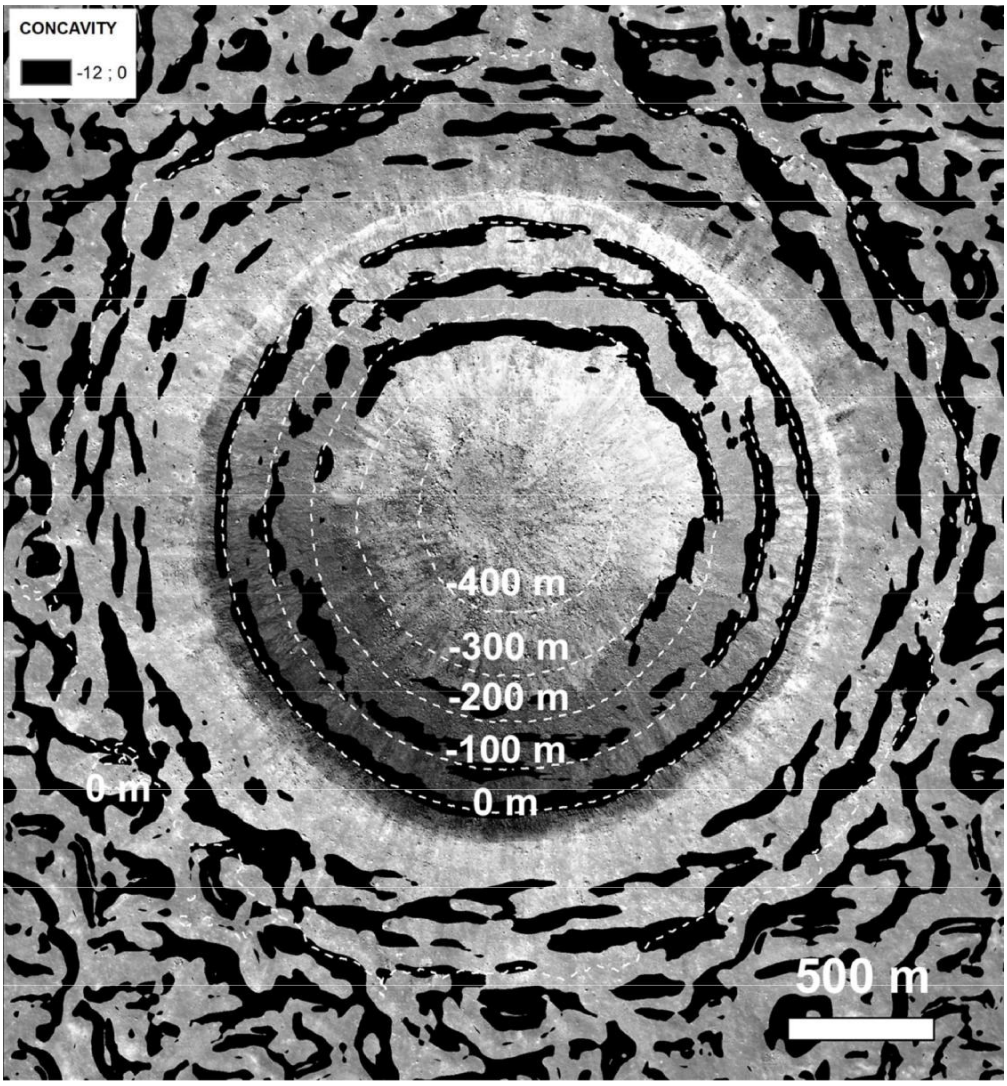

Figure 10. The figure represents the Linné crater overlaid by the post-processed profile curvature map. Crater concavities (negative values) revealed in Figure 8C were enhanced through a "3-threshold classification" method. Such technique relied in merging the zero, positive and negative values of the profile curvature in three separate classes, then setting to zero all the positive values, and finally showing only the negative ones. This new map highlighted the presence of three topographic steps along the inner wall at about +20, -100, and -200 m with respect to a theoretical zero set at the mare surface (-2620 m). The +20 m ring can be associated to the transition from the structurally-uplifted rim to the ejecta blanket; the -100 m ring can possibly represent the interface between two distinct geological units emplaced at different time on the Serenitatis basin; finally, the -200 m ring can mark the upper boundary of breccia lens on the crater floor.

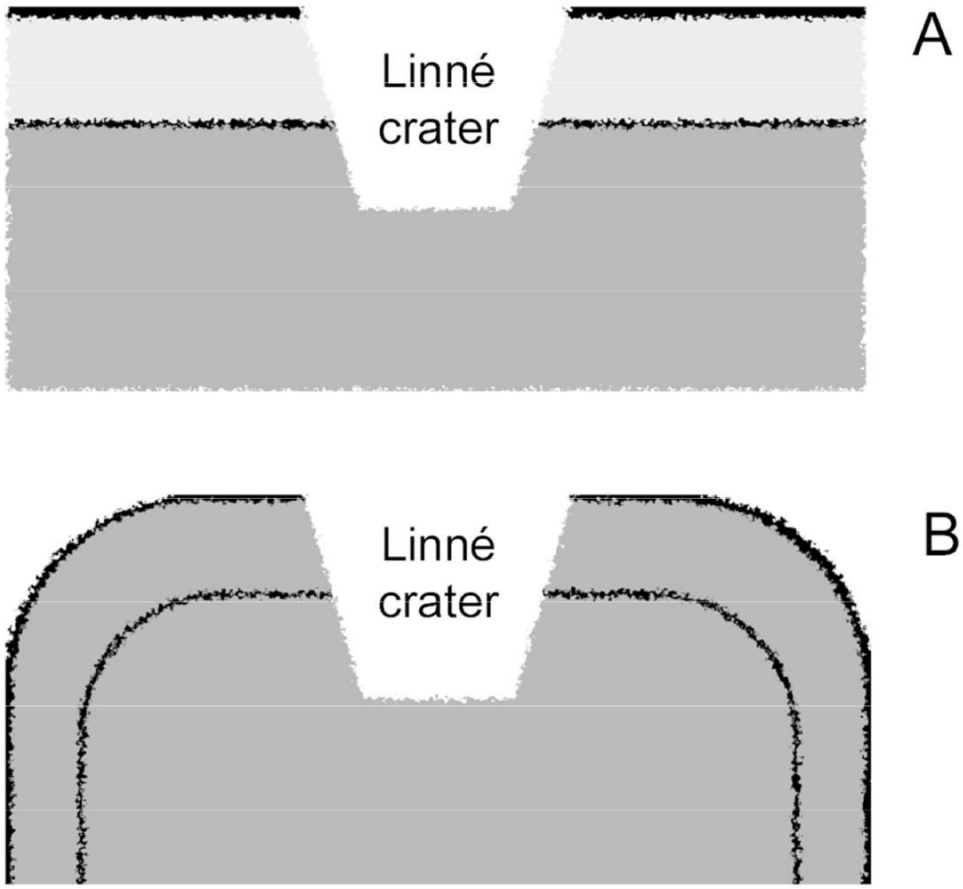

Figure 11. Sketch of our interpretation of the stratigraphy of Mare Serenitatis at the Linné impact site. Differences in age between the two layers are underlined by using a different color. A representative shape of Linné crater is drawn over over the two settings. A) The two modeled layers are different mare (compound flow) units, where the upper one experienced stronger impact cratering and/or fracturing after cooling processes, and emplaced soon afterwards the lower one. B) The two modeled layers represent the brittle shell over a competent core of a single volcanic inflated-like event.